Investigation of Possibilities to Measure the Deuteron Electric Dipole Moment at storage rings

Von der Fakultät für Mathematik, Informatik und Naturwissenschaften der RWTH Aachen University zur Erlangung des akademischen Grades eines Doktors der Naturwissenschaften genehmigte Dissertation

vorgelegt von

Master of Science

Stanislav Chekmenev

aus Sankt Petersburg, Russland

Berichter: Univ.-Prof. Dr. rer. nat. Jörg Pretz
Prof. Dr. Yury Senichev

Tag der mündlichen Prüfung: 08.02.2017

I dedicate this thesis to my wife and my mother for their endless love and support.

CONTENTS

1

MOTIVATION FOR THE SEARCH FOR AN ELECTRIC DIPOLE MOMENT OF A PARTICLE

A HISTORY LESSON

The Standard Model (SM) of particle physics, which was invented in the middle of 1960s, successfully describes elementary particles and interactions between them. The verification of the Standard Model was made in several experiments such as the discoveries of top quark in 1995 [2], [3] and tau neutrino in 2000 [58] along with the latest observation of the Higgs boson in 2012 [29]. Despite of the great number of right predictions for many experimental results, the SM doesn't provide the full explanation for the baryon asymmetry of the universe.

Two Japanese theoreticians, M.Kobayashi and T.Maskawa, have completed the SM by adding CKM matrix in it that describes flavour-changing in weak interactions in 1974 [57]. CP symmetry violation can be also characterized by CKM matrix, but the predicted baryon asymmetry turns out to be several orders of magnitude smaller than the observable one [42]. Thus, one cannot fully explain this phenomenon in the Standard Model frame. Symmetries are the fundamental concepts in modern physics, there are three of them in the Standard Model:

- C-symmetry — charge symmetry — all physical processes happen identically, when the a particle becomes its antiparticle;
- P-symmetry — parity symmetry — invariance of physical processes with respect to sign changing in all the particle coordinates;
- T-symmetry — time symmetry — invariance of the all physical equations, when time changes sign.

In 1954 G.Lüders and W.Pauli, independently of each other, proved the CPT-theorem, which reads: in all processes of quantum field theory holds the CPT invariance (C-,P- and T-transformations performed simultaneously [67], [77]). The direct consequence of this theorem is the fact that the breaking of CP-symmetry leads to T-symmetry violation, and vice versa.

In 1964 J.Cronin and V.Fitch found the first evidence of CP-symmetry breaking in K^0 meson decay [32]: neutral kaons may turn into their antiparticles, or the other way around; however, those transformations occur

with different probability in both directions. Moreover, the violation of CP invariance was detected in a series of other experiments such as NA31 [44], NA48 [39] in CERN, BaBar [16] in SLAC, Belle [4] in KEK. The CP violation in c quarks was observed in LHCb experiment in 2011 in LHC [1].

One of the essential problems of modern physics is the baryon asymmetry of the Universe [28] that represents the fact of the prevalence of matter over antimatter. The experiments COBE [43] and WMAP [49] have proven that. In addition, cosmic detectors, which purpose is to search for antimatter, PAMELA and AMS haven't found any significant amount of it in the Universe [78],[6] yet. The development of the new idea, that claims one of the reasons for the baryon asymmetry is the breaking of CP invariance, has begun soon after its discovery. A.Sakharov has shown three necessary conditions for baryogenesis (initial creation of baryons) in 1967 [82]:

- Baryon number violation;
- C-symmetry and CP-symmetry violation;
- Interactions out of thermal equilibrium.

Number of experiments have been taking place since the beginning of 1980s, in which the baryon number violates, for instance, the proton decay (Super-Kamiokande [75] and IMB [21]) and neutron oscillations (Super-Kamiokande [5] and ILL [93]).

Many theories beyond the SM have been proposed in the following years in order to solve that problem such as Weinberg multi-Higgs [98], theory of "Natural" left-right symmetry [74] and supersymmetric approaches [76],[99],[34]. All those methods of so-called "New Physics" are able to remove the difficulties, which one meets in the Standard Model, but their experimental confirmation has yet to be found.

ELECTRIC DIPOLE MOMENT

One of the possible arguments for the breaking of CP invariance is the existence of non-vanishing electric dipole moments (EDM) of elementary particles. Any object that has an electric charge distributed in volume V with density $\rho(\vec{r})$ has an EDM:

$$\vec{d} = \int_V \vec{r}\rho(\vec{r})d^3\vec{r}.$$

In the most simple case when the system consists of two points with charges q and $-q$ (for example, a NaCl molecule) an EDM vector has the following representation:

$$\vec{d} = q \cdot \vec{r},$$

where $\vec{r}$ is the displacement vector pointing from the negative charge to the positive charge.

It is well known that elementary particles have an intrinsic magnetic moment $\vec{\mu}$, which exists due to the presence of an intrinsic angular moment that is called spin $\vec{S}$:

$$\vec{\mu} = g \cdot \mu_0 \cdot \vec{S},$$

where g is the gyromagnetic ratio and μ_0 is the Bohr magneton or nucleon magneton [53].

If a nonzero EDM of an elementary particle exists, it violates both T- and P-symmetries [79]. The demonstration of this process is presented in Figure 1. The theory says that the EDM must be connected to the spin, since it's the only direction, relatively to which it can be defined for an elementary particle. So the EDM is either parallel or anti-parallel to the spin vector.

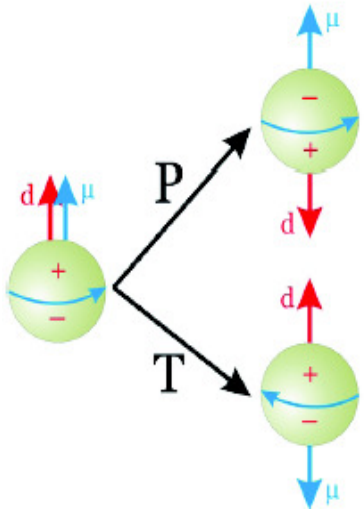

Figure 1: T- and P-symmetry violation in the presence of an EDM (from A.Knecht [56]).

The magnetic moment of a particle is drawn in blue and lies along the spin vector, it is the axis of the particle "rotation", "+" and "−" signs denote the positive and the negative charge densities, which are spatially separated, and the red vector is the EDM of the particle pointing from the negative to the positive charge. After a parity transformation the direction of the particle "rotation",i.e. spin direction, stays the same, since it is an axial vector, but the EDM vector changes sign and, therefore, breaks P invariance. The spin vector changes sign under a time reversal transformation, but the EDM stays untouched that indicates the breaking of T-symmetry. Thus if CPT-theorem holds, P- or T-symmetry violation leads to CP violation.

The first method of measuring a neutron EDM was proposed in 1957 [94] and ever-since there are many ongoing experiments of measuring an elementary particle EDM in the world. For example, there are a

number of experiments that use ultracold neutrons: ILL [93], FRM-II [7] and PNPI; electron EDM experiments: in ICL that uses YbF molecules [96], in Harvard with ThO [97], etc. There are plans to conduct a proton EDM experiment in BNL [95] and deuteron EDM investigation in IKP FZJ [63].

The current interest for an EDM search is generated by the fact that the SM predicts tiny non-vanishing values for EDMs of elementary particles, for instance, neutron EDM $|d_n| \sim 10^{-31} \div 10^{-32}\, e{\cdot}\text{cm}$, electron EDM $|d_e| \sim 10^{-40}\, e{\cdot}\text{cm}$, muon EDM $|d_\mu| \sim 10^{-38}\, e{\cdot}\text{cm}$ [55]. Nevertheless, the theories beyond the Standard Model provides EDMs that are several orders of magnitude higher such as SUSY models where neutron EDM is of the order of $|d_n| \sim 10^{-26} \div 10^{-30}\, e{\cdot}\text{cm}$ [95]. So if one measures an EDM, it opens the door to the "New Physics" and sheds light on the mystery of our Universe creation. Despite of the efforts being made, an EDM of any elementary particle has not been found yet, but the precision of the experiments grows in time (Figure 2).

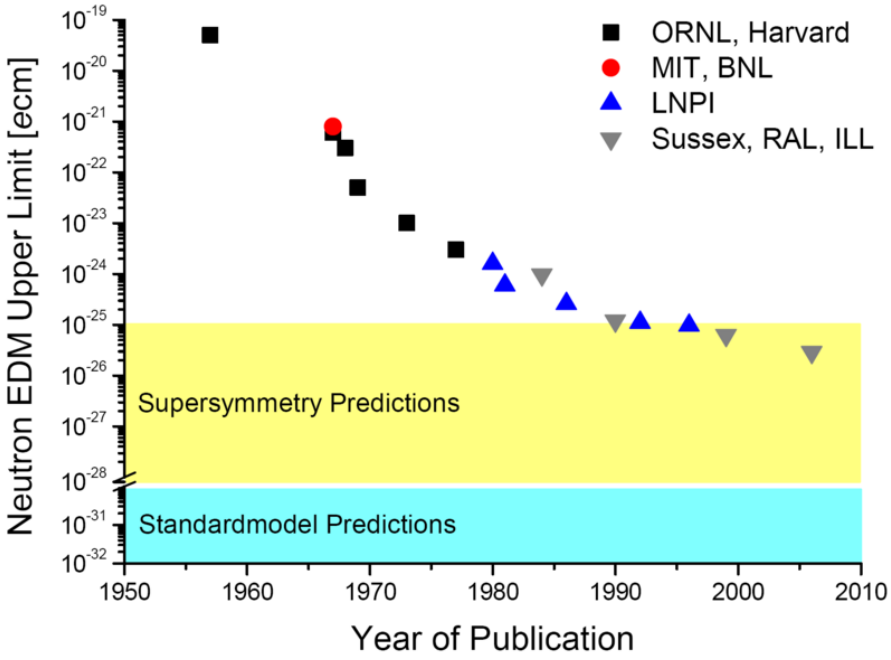

Figure 2: Measured upper limits of the neutron EDM. Given are also the predictions stemming from the Supersymmetry and the Standard Model [56].

There are the following measured upper limits of the different particles EDMs at the present time [97], [19], [22], [35]:

One of the problems of measuring such a small values is the necessity of accumulation of gigantic amount of experimental data in order to reach an acceptable confidence level. The "frozen spin" method of the proton EDM measurement was proposed in 2004 [41]. It's proposed to use a storage ring with all electric elements and a special ("magic") energy, on which a spin of a proton always points in the direction of its momentum,

Particle	EDM	Confidence level
electron	$< 10^{-29}\, e{\cdot}\mathrm{cm}$	90%
neutron	$< 2.9 \cdot 10^{-26}\, e{\cdot}\mathrm{cm}$	90%
muon	$< 1.8 \cdot 10^{-19}\, e{\cdot}\mathrm{cm}$	95%
proton	$< 5.4 \cdot 10^{-24}\, e{\cdot}\mathrm{cm}$	NA

Table 1: The latest measured EDM limits for elementary particles.

hence the name is "the frozen spin". The signal is the polarization build up out of the horizontal plane corresponding to the interaction of an EDM with electric field. An electrostatic ring, with the radius of $\sim 40\mathrm{m}$, the field of $\sim 10\,\mathrm{MV/m}$ and with $\sim 3\,\mathrm{cm}$ gap between the plates, was proposed to construct for this search. The horizontally polarized beam should be injected into the ring and the EDM kicks the spin out of the plane, which causes the build up of the vertical polarization. The polarization is detected with a polarimeter (Figure 3).

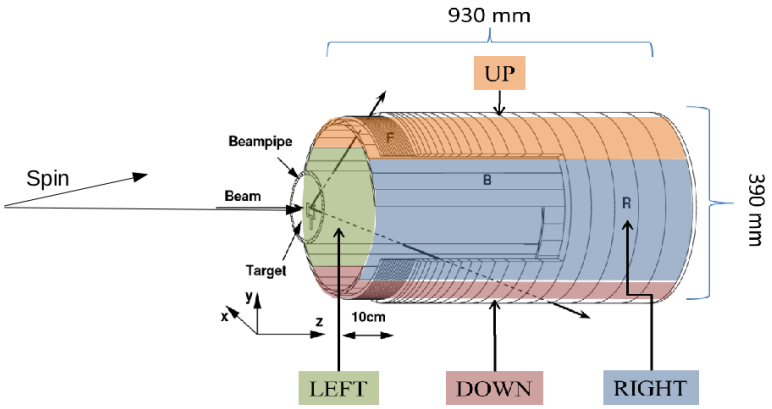

Figure 3: Polarimeter scheme.

The polarimeter detects protons that are elastically scattered on the carbon target [73]. One should look into Up-Down asymmetry to measure the horizontal polarization and into Left-Right asymmetry for the vertical polarization, which is essentially the EDM signal. The sensitivity of the polarimeter is proportional to the number of registered events. The advantage of using a storage ring for this investigation is that one can keep a large amount of stored particles $(10^9 \div 10^{10})$, that gives an efficiency for a current polarimeter of about 1% [95].

It is planned to reach the sensitivity of $10^{-29}\,e{\cdot}\mathrm{cm}$ for the proton EDM in the proposed experiment that 5 orders of magnitude higher than in the previous attempt, moreover, it will be the first direct measurements of an EDM of a charged hadron. The build up of the vertical polarization increases linearly with time. This rise must be detectable with a polarimeter, it means one must wait long enough to see the signal. If the proton EDM equals to $|d_p| \sim 10^{-29}\,e{\cdot}\mathrm{cm}$, the electric field is $\sim 10\,\mathrm{MV/m}$, then the polarization build up per second is $3.2\,\mathrm{nrad/s}$ [95]. Modern polarimeters are able to see the polarization of $1\,\mu\mathrm{rad}$. It means that one must store the beam without loosing horizontal polarization for approximately 1000 seconds or 10^9 turns. This is a difficult task that has to be solved at the first place, since as soon as the horizontal polarization vanishes, one destroys the build up of the vertical polarization. Therefore, the time of storage of a horizontally polarized beam is the main factor, which limits the sensitivity of the experiment. This time, during which a beam stays horizontally polarized, is called spin coherence time [63].

PRECURSOR AT COSY

The Cooler Synchrotron (COSY) that is located in Forschungszuntrum Jülich was chosen as a facility to perform the precursor charged particle EDM experiment [68]. COSY is a storage ring, which operates with polarized protons and deuterons in the kinetic energy range from 40 MeV to 2.5 GeV. The length of the ring is 183 m. One can see the schematic view of the ring in Figure 4. The EDDA detector at COSY, pictured

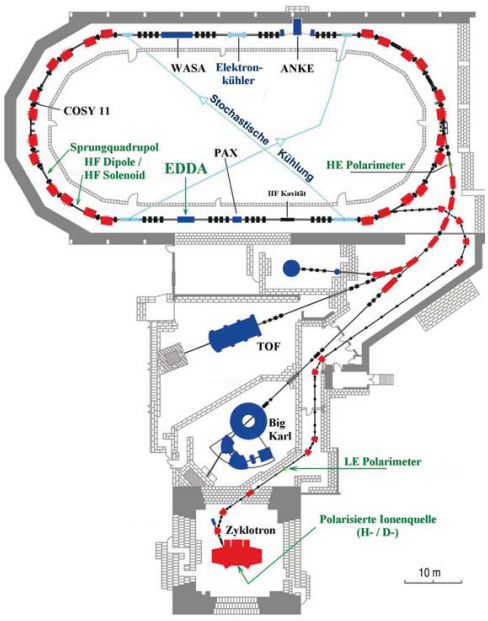

Figure 4: The scheme of COSY ring [68].

in Figure 5 analyzes polarization. Several methods for the precursor

experiment at COSY were proposed in the recent years [64],[63]. One of them will be discussed in chapter 5.

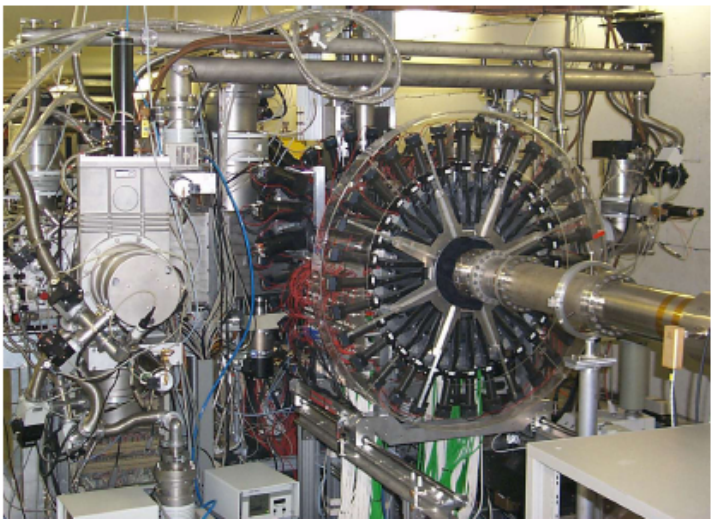

Figure 5: EDDA detectror at COSY.

Test runs for better understanding of polarized beams' behavior, for developing spin manipulation techniques and maximization of the spin coherence time have been being performed for the last 7 years at COSY [38], [48].

The development of a new ring for the final EDM experiment requires a detailed beam dynamics analysis. The beam dynamics investigations have the goal to find the precise solution of the equation of motion for the short period of time and further analysis of the evolution of the beam parameters in time. So the main subject of the accelerator physics is the study of periodic structures such as storage rings and accelerators. All these structures let one keep the beam for long periods of time, i.e. all the processes take place inside the dynamics aperture of the accelerator. The broad theory have been built throughout the decades, as well as the appropriate mathematical methods for beam dynamics studies.

SIMULATIONS

The motion of particles in the accelerator rings in the presence of electromagnetic fields is studied with numerical simulation approach. For this purpose there were invented a number of programs, for instance, MAD [47], COSY-Infinity [24], OptiM [61] and others. Modeling longstanding processes as the evolution of spin-orbital motion, which is absolutely necessary for a new EDM machine design, impose special criteria for any simulation program such as symplecticity and energy conservation [25], [36]. One of the methods of studying such long-lived systems is the mapping approach [37], [26]. The advantage of this technique is the

high computational speed that gives an opportunity to have a look at full evolution of the process.

The newly developed program MODE [52], written by A. Ivanov and S. Andrianov from Saint-Petersburg State University, was used in the work presented in this thesis. It solves the equations of motion and the generalized Thomas-BMT [20],[45] equation and generates maps, which are used later for tracking in Matlab [71]. More detailed program description will be presented in chapter 2.

OUTLINE

The main subject of this thesis is the investigation of systematic errors for the future electric dipole moment experiment. Two possible ring designs for the "final" ring and the design for the precursor experiment will be considered in this work. The sensitivity limits for the precursor search and for both methods, which aim to measure an EDM with the highest possible precision, will be set.

The main part is divided into 5 chapters.

The first of them is dedicated to the mathematical model of spin-orbital dynamics. An overview to the equations that are essential for the understanding of the physics considered in the thesis will be made. The equations of spin-orbital motion will be derived in canonical coordinates, as well. The map formalism, which is used in the simulation program, will be discussed.

The concept of spin coherence time is shown in Chapter 3. The mechanisms that lead to depolarization of a particle bunch are studied. The fundamental sources of systematic errors, which appear in any storage ring EDM experiment, are briefly represented, too.

Chapter 4 is assigned to benchmarking of MODE program, which was the primary simulation tool in this research. A quick introduction to MODE environment is made and the structure of the program is discussed. Experimental results from a testing run in 2014 are shown and compared with simulations made with MODE.

Chapter 5 of the main part is devoted to the methods for a hadron EDM measurement at a storage ring. The base ideas for the frozen and the quasi-frozen spin methods that require a new ring are explained in this chapter. The radio frequency Wien filter approach, which is planned to be the one for the precursor experiment, is investigated, too.

Chapter 6 describes the systematic errors for the "final" experiment and for the precursor separately, since they differ in some details. The possible ways that can be used to overcome the systematics are considered. Simulations are performed and their results are thoroughly examined and the sensitivity limits are set.

In conclusion, one finds the description of the results that were obtained during this research, as well as, the future outlook.

2

MATHEMATICAL MODELING OF SPIN-ORBITAL DYNAMICS

INTRODUCTION

The present chapter gives an overview of the working principle of MODE program and general consideration of spin-orbital particle dynamics at an accelerator. The mathematical formalism is discussed in detail. Equations of spin-orbital dynamics are derived in canonical coordinates. The coordinate choice is caused by the physical side of the task and the convenience of code implementation in the program.

SPIN-ORBITAL DYNAMICS

This section gives an overall introduction to the spin-orbital dynamics at a storage ring.

The orbital motion

One can define the orbital motion as a variation of spacial coordinates of the particle, which travels in the electromagnetic fields of a storage ring, in time. The electromagnetic fields are described by the vectors of electric field strength $\vec{E}$ and magnetic induction $\vec{B}$. The laws of electromagnetism are defined as Maxwell equations [81]

$$\nabla\cdot\vec{E} = \frac{\rho}{\epsilon_0},\ \nabla\times\vec{E} = -\frac{\partial\vec{B}}{\partial t},\nabla\cdot\vec{B} = 0,\ \nabla\times\vec{B} = \frac{1}{c^2}\frac{\partial\vec{E}}{\partial t} + \mu_0\vec{J}, \tag{2.2.1}$$

where ρ is the overall charge density, $\vec{J}$ is the vector of overall electric current density, ϵ_0 and μ_0 are electric and magnetic constants, which are vacuum permittivity and vacuum permeability, c is the speed of light. If the charges and currents do not change in time, the equations become more simple and have the form

$$\begin{aligned}\nabla\cdot\vec{E} = \frac{\rho}{\epsilon_0},\ \nabla\times\vec{E} = 0,\\ \nabla\cdot\vec{B} = 0,\ \nabla\times\vec{B} = \mu_0\vec{J}\end{aligned} \tag{2.2.2}$$

When the fields are static the electric and the magnetic components are independent of each other, and the electric field strength can written via the scalar potential u

$$\vec{E} = -\nabla u \tag{2.2.3}$$

Inserting this formula into Maxwell's equations one can get Poisson equation $\Delta u = \frac{\rho}{\epsilon_0}$, and when $\rho = 0$ this equations is called Laplace's equation, which has the following form in generic orthogonal curvilinear coordinates

$$\Delta u = \frac{1}{h_1 h_2 h_3} \sum_{i=1}^{3} \frac{\partial}{\partial q_i} \Big(\frac{h_1 h_2 h_3}{h_i^2} \frac{\partial u}{\partial q_i} \Big), \tag{2.2.4}$$

where q_1, q_2, q_3 are generic curvilinear coordinates, h_1, h_2, h_3 are metric Lamé coordinates [102] that characterize a certain reference system, and the potential u is the function of generic coordinates $u = u(q_1, q_2, q_3)$. One considers q_3 as a time dependent variable $q_3 = q_3(t)$ and two other coordinates as the functions $q_1 = q_1(q_3)$, $q_2 = q_2(q_3)$. In case of accompanying reference system, which is usually used in beam dynamics simulations [106], [107], the role of independent variable plays the path length s of a reference particle.

The Lorentz force acts on the particle with the charge q and the velocity $\vec{v}$, which propagates through the electromagnetic field. The equation of motion in that case is

$$\frac{d}{dt}\vec{p} = q\Big(\vec{E} + \vec{v} \times \vec{B}\Big), \tag{2.2.5}$$

where $\vec{p} = m_0 \gamma \vec{v}$ is the particle momentum, m_0 is the rest mass. The coefficient γ is Lorentz factor and is equal to $\gamma = (1 - \frac{v^2}{c^2})^{-1/2}$. The absolute value of the velocity of particle v and the speed of light c will be used in later discussion.

Using Lagrangian mechanics [108], the equation 2.2.5 can be rewritten in arbitrary curvilinear coordinate system. The equations of motion will be

$$\begin{aligned} \frac{dp_i}{dt} + \Big(\frac{\dot{q}_i}{h_{i+1}} \frac{\partial h_i}{\partial q_{i+1}} - \frac{\dot{q}_{i+1}}{h_i} \frac{\partial h_{i+1}}{\partial q_i} \Big) p_{i+1} + \Big(\frac{\dot{q}_i}{h_{i+2}} \frac{\partial h_i}{\partial q_{i+2}} - \frac{\dot{q}_{i+2}}{h_i} \frac{\partial h_{i+2}}{\partial q_i} \Big) p_{i+2} = \\ = q(E_i + h_{i+1}\dot{q}_{i+1} B_{i+2} - h_{i+2}\dot{q}_{i+2} B_{i+1}, \\ i = 1, 2, 3, \end{aligned} \tag{2.2.6}$$

where the indices change cyclically ($q_4 = q_1$, $q_5 = q_2$) and $'' \cdot ''$ is the operator of time differentiation. Equations (2.1.6) describe the evolution of curvilinear coordinates in time. For beam dynamics purposes the time differentiation is changed to differentiation with respect to the chosen coordinate, usually with respect to s.

Using the formula for elementary path length in curvilinear reference system,

$$\frac{d}{dt} = \frac{v}{(h_1^2 q_1'^2 + h_2^2 q_2'^2 + h_3^2}\frac{d}{dq_3)^{1/2}} \tag{2.2.7}$$

Momenta projections will be

$$p_i = h_i m_0 \gamma \dot{q}_i = h_i \frac{m_0 \gamma v}{(h_1^2 q_1'^2 + h_2^2 q_2'^2 + h_3^2)^{1/2}} q_i' \tag{2.2.8}$$

Inserting 2.2.8 into 2.2.6 one can obtain the resulting expressions for trajectory equations

$$\begin{aligned} q_1'' + \gamma^{-1}(\frac{HD}{v}q_1') + \Big(q_2'(2q_1'\frac{\partial h_1}{\partial q_2} - \frac{h_2 q_2'}{h_1}\frac{\partial h_2}{\partial q_1}) + \frac{\partial h_1}{\partial q_1}q_1'^2 + 2q_1'\frac{\partial h_1}{\partial q_3} - \\ - \frac{h_3}{h_1}\frac{\partial h_3}{\partial q_1}\Big)/h_1 = \frac{qH}{h_1 m_0 \gamma v}(\frac{HE_1}{v} + h_2 q_2' B_3 - h_3 B_2), \\ q_2'' + \gamma^{-1}(\frac{HD}{v}q_2') + \Big(q_1'(2q_2'\frac{\partial h_2}{\partial q_1} - \frac{h_1 q_1'}{h_2}\frac{\partial h_1}{\partial q_2}) + \frac{\partial h_2}{\partial q_2}q_2'^2 + 2q_2'\frac{\partial h_2}{\partial q_3} - \\ - \frac{h_3}{h_2}\frac{\partial h_3}{\partial q_2}\Big)/h_2 = \frac{qH}{h_2 m_0 \gamma v}(\frac{HE_2}{v} - h_1 q_1' B_3 + h_3 B_1), \end{aligned} \tag{2.2.9}$$

where $\vec{E} = (E_1, E_2, E_3)$ and $\vec{B} = (B_1, B_2, B_3)$, H and D are functions of generic coordinates

$$\begin{aligned} H = (h_1^2 q_1'^2 + h_2^2 q_2'^2 + h_3^2)^{1/2}, \\ D = \frac{q}{m_0 h_3}(h_1 q_1' B_2 - h_2 q_2' B_1 + \frac{HE_3}{v}) - \\ - \frac{\gamma v}{H h_3}\Big(h_1 q_1'(\frac{2}{h_1}\frac{\partial h_3}{\partial q_1} - \frac{q_1'}{h_3}\frac{\partial h_1}{\partial q_3}) + h_2 q_2'(\frac{2}{h_2}\frac{\partial h_3}{\partial q_2} - \frac{q_2'}{h_3}\frac{\partial h_2}{\partial q_3}) + \frac{\partial h_3}{\partial q_3}\Big). \end{aligned} \tag{2.2.10}$$

Equation 2.2.6 transforms into two equations for two projections onto two perpendicular planes, and they are relativistic trajectory equations in general orthogonal coordinate system. For the trajectory, as it was said before, one should pick some curve, for instance, the path of the reference particle, and the length of this curve will be the variable of integration. Coordinate axes $q_1 = x$, $q_2 = y$ will be perpendicular to the path of the reference curve. So, the coordinate system is an accompanying coordinate system, which is moving along the given curve.

One has to use the energy conservation law for calculation of the absolute value of the velocity from equation 2.2.9

$$m_0 c^2(\gamma - \gamma_0) + q(u - u_0) = 0, \tag{2.2.11}$$

where potential u is given by formula 2.2.3, γ_0 is the particle velocity in the place with potential u_0 and γ - with potential u.

T-BMT equation

Spin is a fundamental characteristic of a particle and is expressed by a quantum number. However, in a frame of Hamiltonian formalism it is more convenient to work with ordinary differential equation. Quasi-classical approach for spin dynamics representation is maintained by the Thomas-Bargmann-Michel-Telegdi (the T-BMT) equation [20]

$$\frac{d}{dt}\vec{S} = \frac{-q}{m_0\gamma}\Big((1+G\gamma)B_\perp + (1+G)B_\parallel + (G\gamma + \frac{\gamma}{\gamma+1})\frac{\vec{E}\times\vec{\beta}}{c}\Big)\times\vec{S}, \tag{2.2.12}$$

where G is the dimensionless anomalous magnetic factor, $\vec{\beta}c = \vec{v}$, $B_\perp$ and $B_\parallel$ are perpendicular and longitudinal components with respect to the direction of the velocity of a particle. The given equation can be written in terms of the magnetic induction vector $\vec{B}$. Indeed, the longitudinal component of the magnetic field one can present as a projection onto the direction of particle's momentum $B_\parallel = (\vec{B},\vec{p})\frac{\vec{p}}{\vec{p}^2}$. The perpendicular component in this notation will be $B_\perp = \vec{B} - B_\parallel$. Inserting those expressions into 2.2.12 one obtains the frequency of spin precession

$$\begin{aligned}\vec{\Omega} &= \frac{-q}{m_0\gamma}\Big((1+G\gamma)(\vec{B}-B_\parallel) + (1+G)B_\parallel + (G+\frac{1}{\gamma+1})\frac{\vec{E}\times\vec{p}}{m_0c^2}\Big) = \\ &= \frac{-q}{m_0\gamma}\Big((1+G\gamma)\vec{B} - \frac{G}{\gamma+1}\frac{(\vec{B},\vec{p})\vec{p}}{m_0^2c^2} - (G+\frac{1}{\gamma+1})\frac{\vec{p}\times\vec{E}}{m_0c^2}\Big).\end{aligned} \tag{2.2.13}$$

The T-BMT equation, which has the following form

$$\frac{d}{dt}\vec{S} = \vec{\Omega}(\vec{p},\vec{B},\vec{E})\times\vec{S}, \tag{2.2.14}$$

can be written in accompanying coordinate system. When the curve is plane and has the constant curvature k the equation is

$$\vec{S}' = \begin{pmatrix}0 & 0 & k\\ 0 & 0 & 0\\ -k & 0 & 0\end{pmatrix}\vec{S} + \frac{H}{v}\vec{\Omega}\times\vec{S}. \tag{2.2.15}$$

Equations 2.2.14 2.2.15 describe the spin motion in arbitrary fields.

Homogeneous vertical magnetic field

When one takes a look at equation 2.2.5, it is clear that in the presence of the vertical homogeneous magnetic field $\vec{B} = (0;B_0;0)$, where $B_0 = (m_0\gamma v)/(qR)$, a particle will be moving along the circumference with

radius R and with the constant absolute value of the velocity. Inserting the frequency of spin precession in 2.2.14

$$\vec{\Omega} = \frac{-q}{m_0\gamma}(1+\gamma G)\vec{B} = \frac{-q}{m_0\gamma}(1+\gamma G)(0;\frac{m_0\gamma v}{qR};0)$$

and taking into account that $k = 1/R$, one obtains

$$S'_x = \frac{1}{R}S_s + \frac{1}{v}\frac{m_0\gamma v}{qR}S_s\frac{-q}{m_0\gamma}(1+\gamma G) = -\frac{\gamma G}{R}S_s,$$
$$S'_s = -\frac{1}{R}S_x - \frac{1}{v}\frac{m_0\gamma v}{qR}S_x\frac{-q}{m_0\gamma}(1+\gamma G) = \frac{\gamma G}{R}S_x.$$

The elementary path length $ds = Rd\phi$, where ϕ is the angle of the rotation of the particle momentum in the ring. Considering this fact the frequency of the spin rotation with respect to the momentum vector will be

$$\omega = \gamma G. \tag{2.2.16}$$

Homogeneous longitudinal magnetic field

The spin precession in the longitudinal homogeneous magnetic field $\vec{B} = (0;0;B_z)$ is considered. Also, $B\rho = B_0R = (m_0\gamma v)/q$. Thus, the spin precession frequency is

$$\vec{\Omega} = \frac{-q}{m_0\gamma}(1+\gamma G)\vec{B} - \frac{G}{\gamma+1}B_z\frac{\gamma^2v^2}{c^2}.$$

Inserting this again in equation 2.2.14 and taking into account that for the straight section $k = 0$, one gets

$$S'_x = \frac{B_z}{B\rho}(1+G)S_y,$$
$$S'_y = -\frac{B_z}{B\rho}(1+G)S_x, S'_s = 0.$$

The spin vector in the presence of the longitudinal field B_z rotates with the frequency

$$\omega = \frac{B_z}{B\rho}(1+G). \tag{2.2.17}$$

Homogeneous radial electric field

In the radial homogeneous electric field $E_0 = (m_0\gamma v^2)$ a particle moves with the constant velocity and constant radius R of the circumference. The so-called *magic* energy is the energy of the particle when its spin rotates in the horizontal plane with the same frequency as the momentum.

This *magic* condition could be easily obtained if the frequency of spin precession in the electric field equals to zero. The T-BMT equation, then, has the form

$$S'_x = \frac{1}{R}S_s + \frac{H}{v}\Omega_y S_s = \omega S_s,$$
$$S'_s = -\frac{1}{R}S_x - \frac{H}{v}\Omega_y S_x = \omega S_x,$$

where $S'_y = 0$, and that means that the frequency is

$$\omega = \frac{1}{R}\Big(1 - \gamma\beta^2(G + \frac{1}{1+\gamma})\Big). \tag{2.2.18}$$

Setting this value of the frequency to zero, one can write the formula linking the *magic* energy (γ_m) and the magnetic factor G

$$G = \frac{1}{\gamma_m^2 - 1}. \tag{2.2.19}$$

The value of the *magic* energy is especially important for studies of the spin-orbital motion in electric storage rings because it allows one to *freeze* the spin [83], [84]. In such an experiment the spin vector lies along the momentum for all the time in the case of zero EDM. If there is a non-vanishing EDM, one will observe a rise of the vertical polarization in time.

Conclusion

In this section, the main equations of spin-orbital dynamics were considered in curvilinear coordinate system. These equations are used in the building of the mathematical model of particle motion, which is needed for the simulation made in this work.

TRAJECTORY EQUATIONS IN BEAM DYNAMICS

Equation 2.2.9 describes the trajectory dynamics in arbitrary orthogonal curvilinear coordinates. The accompanying coordinate system follows the path of the reference particle, when one works with models for beam dynamics calculation. This path is usually a straight line or an arc. The choice of the reference trajectory is connected to the symmetry of the field. The reference particle in a such coordinate system is a stationary point. When there are no perturbations, for instance, field errors or fringe fields, a given stationary point lies in the beginning of the coordinates. In general, such stationary point is the state with zero coordinates in that reference frame, and this state evolves into itself again after one full turn around the storage ring.

Derivation of the equations for accompanying coordinate system

In the trivial case of Cartesian coordinate system all the Lamé coefficients are equal to one, and the equations of motion have the following form [105]

$$x'' = \frac{q}{m_0 v}\Big((1-\frac{v^2}{c^2})(1+x'^2+y'^2)\Big)^{1/2}\Big((1+x'^2+y'^2)^{1/2}(E_x - x'E_z)/v - \\ -(1+x'^2)B_y + y'(x'B_x + B_s)\Big),$$
$$y'' = \frac{q}{m_0 v}\Big((1-\frac{v^2}{c^2})(1+x'^2+y'^2)\Big)^{1/2}\Big((1+x'^2+y'^2)^{1/2}(E_y - y'E_z)/v - \\ -(1+y'^2)B_x + x'(y'B_y + B_s)\Big). \tag{2.3.1}$$

When the motion trajectory is an arc the equations have more complicated form. Firstly, the derivation of the transformation formulas from Cartesian to curvilinear reference system will be considered. At a certain point of the circumference x and y axes are perpendicular (x in the bend plane, y perpendicular to the bend plane) to the path of the reference particle, s is tangent to the reference trajectory. When $s = 0$ the Cartesian and curvilinear reference systems coincide, and $x > -R$ (Figure 6).

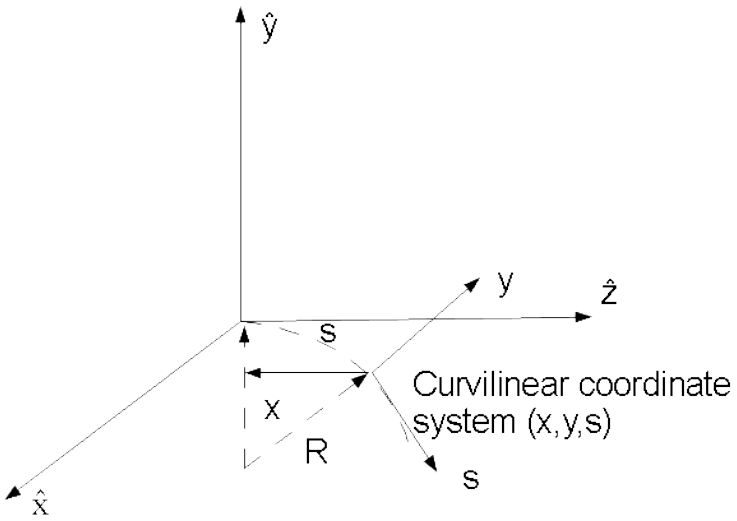

Figure 6: Cartesian and curvilinear coordinate systems.

Using the given notation one can write down the coordinate transformations [54]

$$\begin{aligned} \hat{x} &= -R + (R+x)cos(s/R) \\ \hat{y} &= y \\ \hat{z} &= (R+x)sin(s/R), \end{aligned}$$

which satisfy the condition of orthogonality.

$$\begin{aligned} \frac{\partial\hat{x}}{\partial x}\frac{\partial\hat{x}}{\partial x} + \frac{\partial\hat{y}}{\partial x}\frac{\partial\hat{y}}{\partial x} + \frac{\partial\hat{z}}{\partial x}\frac{\partial\hat{z}}{\partial x} &= 0+0+0 \equiv 0 \\ \frac{\partial\hat{x}}{\partial x}\frac{\partial\hat{x}}{\partial y} + \frac{\partial\hat{y}}{\partial x}\frac{\partial\hat{y}}{\partial y} + \frac{\partial\hat{z}}{\partial x}\frac{\partial\hat{z}}{\partial y} &= 0+0+0 \equiv 0 \\ \frac{\partial\hat{x}}{\partial y}\frac{\partial\hat{x}}{\partial s} + \frac{\partial\hat{y}}{\partial y}\frac{\partial\hat{y}}{\partial s} + \frac{\partial\hat{z}}{\partial y}\frac{\partial\hat{z}}{\partial s} &= 0 - \frac{R+y}{R}cos(\frac{s}{R})sin(\frac{s}{R}) + \\ & \frac{R+y}{R}cos(\frac{s}{R})sin(\frac{s}{R}) \equiv 0 \end{aligned} \tag{2.3.2}$$

In this case Lamé coefficients are

$$\begin{aligned} h_x &= h_y = 1 \\ h_s &= 1 + \frac{x}{R} \end{aligned} \tag{2.3.3}$$

To generalize all the derivable equations for the situation when an arbitrary plane trajectory is used one can use the following function [102]:

$$h_s(x) = \begin{cases} 1, \text{when the motion is along the straight line} \\ 1 + kx, \text{when the motion is along the arc.} \end{cases} \tag{2.3.4}$$

So using equation 2.2.10 and taking into account that $\frac{\partial h_s(x)}{\partial x} = k$ and $\frac{\partial h_s(x)}{\partial s} = kx'$ one can write the functions H and D in the following form

$$\begin{aligned} H &= (x'^2 + y'^2 + {h_s}^2)^{1/2}, \\ D &= \frac{q}{m_o h_s}(x'B_y - y'B_x + \frac{HE_s}{v}) - \frac{\gamma v}{Hh_s}3kx', \end{aligned} \tag{2.3.5}$$

and, finally, generalize the equations 2.3.1 for the motion along arbitrary plane curve [103]

$$\begin{aligned} x'' &= -\frac{HD}{\gamma v}x' + \frac{qH}{m_o\gamma v}\Big(\frac{HE_x}{v} + y'B_s - h_sB_y\Big) + kh_s, \\ y'' &= -\frac{HD}{\gamma v}y' + \frac{qH}{m_o\gamma v}\Big(\frac{HE_y}{v} + h_sB_x - x'B_s\Big). \end{aligned} \tag{2.3.6}$$

Canonical transformations

Equation 2.3.1 describes the orbital dynamics in terms of generic coordinates *x, y* and velocities x', y'. For the purpose of beam dynamics simulations one usually uses momenta projections p_x, p_y, which are included in canonically conjugate pairs of coordinates. In addition, it is inconvenient to use equation 2.3.1 directly because the absolute value of velocity v, which consists in the equation explicitly, is the function of spacial coordinates $v = v(x, y, s)$, and it must be constantly recalculated with according to the energy conservation law 2.2.11. There is a derivation of orbital motion equations in six-dimensional phase-space x, y, t, p_x, p_y, W below, where t is the actual time of flight of a particle through an arbitrary electromagnetic field, W is the particle kinetic energy. These given coordinates are canonically conjugate pairs $P = \{x, y, t\}$ and $Q = \{p_x, p_y, W\}$, and the resulting equations are convenient for the further integration in nonlinear matrix form.

With the usage of 2.2.6 one can write momenta projections onto the axes of the new curvilinear reference system 2.3.3, which is moving along the plane curve 2.3.4,

$$p_x = \frac{m_0 \gamma v}{\sqrt{x'^2 + y'^2 + {h_s}^2}} x' \qquad p_y = \frac{m_0 \gamma v}{\sqrt{x'^2 + y'^2 + {h_s}^2}} y', \tag{2.3.7}$$

and clearly see that $p_x y' = p_y x'$. Solving the last equation with respect to y', one gets for the x component of the momentum the formula without dependence on y'

$$p_x = \frac{m_0 \gamma v}{\sqrt{x'^2 + x'^2 {p_y}^2 / {p_x}^2 + {h_s}^2}} x'.$$

Now one can solve the obtained equation with respect to x'

$$(m_0 \gamma v)^2 x'^2 = {p_x}^2 (x'^2 + x'^2 \frac{{p_y}^2}{{p_x}^2} + {h_s}^2),$$
$$x'^2 = \frac{{p_x}^2 {h_s}^2}{(m_0 \gamma v)^2 - {p_x}^2 - {p_y}^2}.$$

Taking into account that the velocity and momentum vectors are collinear and the denominator $(m_0 \gamma v)^2 - {p_x}^2 - {p_y}^2 = {p_s}^2$ is always positive, one reads

$$x' = \frac{p_x h_s}{\sqrt{(m_0 \gamma v)^2 - {p_x}^2 - {p_y}^2}}. \tag{2.3.8}$$

If one does the same derivation for y', one obtains

$$y' = \frac{p_y h_s}{\sqrt{(m_0 \gamma v)^2 - {p_x}^2 - {p_y}^2}}. \tag{2.3.9}$$

As soon as the further derivation is the same for p_x and p_y momenta projections up to sign, it is handy to use a new variable $\xi \in \{x, y\}$. The derivatives of momenta described by equations 2.3.7 will be equal to

$$p'_\xi = \frac{m_0\gamma v'\xi'}{H} + \frac{m_0\gamma' v\xi'}{H} + \frac{m_0\gamma v\xi''}{H} + m_0\gamma v'\xi'(-\frac{1}{2})H^{-3}(2x'x'' + 2y'y'' + 2h_s h'_s).$$

Using formula 2.3.7 again one gets

$$p'_\xi = p_\xi\Big(\frac{v}{v'} - \frac{\gamma}{\gamma'}\Big) + m_0\gamma v\frac{\xi''}{H} - p_\xi\Big(\frac{p_x}{m_0\gamma v}\frac{x''}{H} + \frac{p_y}{m_0\gamma v}\frac{y''}{H} + \frac{h_s h'_s}{H^2}\Big) \tag{2.3.10}$$

One must take into consideration that p_ξ is the function of only canonical variables x, y, t, p_x, p_y, W. The values x'' and y'' are defined by equation 2.3.6 and the first derivatives - by equations 2.3.8 2.3.9. The function H is

$$H = \sqrt{x'^2 + y'^2 + h_s^2} = \frac{m_0\gamma v x'}{p_x} = \frac{m_0\gamma v h_s}{\sqrt{(m_0\gamma v)^2 - p_x^2 - p_y^2}}. \tag{2.3.11}$$

The next step is to show that the values v, γ, v', γ' also depend only on canonical coordinates. From the formula for kinetic energy of a relativistic particle

$$W = m_0\gamma c^2 - m_0 c^2 \tag{2.3.12}$$

one directly writes the equations for Lorentz factor and its derivative

$$\gamma = \frac{W + m_0 c^2}{m_0 c^2}, \qquad \gamma' = \frac{W'}{m_0 c^2} \tag{2.3.13}$$

On the other hand, kinetic energy may be written via the law of full energy conservation, which has the following differential form

$$W' = -qu'(x, y, s) = q(E_x x' + E_y y' + E_s). \tag{2.3.14}$$

Let us have a look at the velocity v and its derivative v'. From equation 2.3.12 the velocity is

$$v = \frac{c}{W + m_0 c^2}\sqrt{W^2 + 2Wm_0 c^2}, \tag{2.3.15}$$

and its derivative is

$$\begin{aligned} v' = \frac{c}{W^2 + m_0 c^2}\frac{1}{2}(W^2 + 2Wm_0 c^2)^{-1/2}(2WW' + 2W'm_0 c^2) + \\ + c\sqrt{W^2 + 2Wm_0 c^2}(-1)(W + m_0 c^2)^{-2}W' = \\ = cW'(m_0 c^2)^2\Big((W + m_0 c^2)^2\sqrt{W^2 + 2Wm_0 c^2}\Big)^{-1} \end{aligned} \tag{2.3.16}$$

Equations 2.2.7, 2.3.8 - 2.3.10 ,2.3.14 construct the ODE system for orbital motion in accompanying reference system, and all-together with the T-BMT equation fully describe the spin-orbital dynamics of a charged particle [103], [105]. To summarize:

$$
\begin{aligned}
x' &= \frac{p_x h_s}{\sqrt{(m_0\gamma v)^2 - {p_x}^2 - {p_y}^2}},\\
y' &= \frac{p_y h_s}{\sqrt{(m_0\gamma v)^2 - {p_x}^2 - {p_y}^2}},\\
t' &= \frac{H}{v},\\
p'_x &= p_x\Big(\frac{v}{v'} - \frac{\gamma}{\gamma'}\Big) + m_0\gamma v\frac{x''}{H} - p_x\Big(\frac{p_x}{m_0\gamma v}\frac{x''}{H} + \frac{p_y}{m_0\gamma v}\frac{y''}{H} + \frac{h_s h'_s}{H^2}\Big),\\
p'_y &= p_y\Big(\frac{v}{v'} - \frac{\gamma}{\gamma'}\Big) + m_0\gamma v\frac{y''}{H} - p_x\Big(\frac{p_x}{m_0\gamma v}\frac{x''}{H} + \frac{p_y}{m_0\gamma v}\frac{y''}{H} + \frac{h_s h'_s}{H^2}\Big),\\
W' &= -qu'(x,y,s) = q(E_x x' + E_y y' + E_s),\\
S'_x &= kS_s + \frac{H}{v}\Big((k_1(B_y S_s - B_s S_y) + k_2(p_y S_s - p_s S_y) +\\
&\quad + k_3\big((p_s E_x - p_x E_s)S_s - (p_x E_y - p_y E_x)S_y\big)\Big),\\
S'_y &= \frac{H}{v}\Big((k_1(B_s S_x - B_x S_s) + k_2(p_s S_x - p_x S_s) +\\
&\quad + k_3\big((p_x Ey - p_y Ex)S_x - (p_y E_s - p_s E_y)S_s\big)\Big),\\
S'_s &= -kS_x + \frac{H}{v}\Big((k_1(B_x S_y - B_y S_x) + k_2(p_x S_y - p_y S_x) +\\
&\quad + k_3\big((p_y Es - p_s Ey)S_y - (p_s E_x - p_x E_s)S_x\big)\Big),
\end{aligned}
\tag{2.3.17}
$$

where x'' and y'' are given by equation 2.3.1, the function H is characterized by formula 2.3.11, γ, γ' are described by equation 2.3.13 and, finally, the velocity v with its derivative v' are calculated through kinetic energy with formulas 2.3.14 - 2.3.16,

$$
\begin{aligned}
k_1 &= \frac{-q}{m_0\gamma}(1 + \gamma G),\\
k_2 &= \frac{q}{m_0^3 c^2 \gamma}\frac{G}{1+\gamma}(B_x p_x + B_y p_y + B_s p_s),\\
k_3 &= \frac{q}{m_0^2 c^2 \gamma}(G + \frac{1}{1+\gamma}).
\end{aligned}
$$

MATRIX INTEGRATION OF DIFFERENTIAL EQUATIONS

Equations 2.3.17 build a system of non-linear differential equations [104]

$$\frac{d}{ds}\mathbf{X} = \mathbf{F}(s, \mathbf{X})$$

with the state vector $\mathbf{X} = (x, y, t, p_x, p_y, W, S_x, S_y, S_s)$. The solution of this ODE system can be written in matrix form of Taylor series [23], [9], [15]

$$\mathbf{X} = \mathbb{R}_0 + \mathbb{R}_1\mathbf{X}_0 + \mathbb{R}_2{\mathbf{X}_0}^{[2]} + ... + \mathbb{R}_k{\mathbf{X}_0}^{[k]}. \tag{2.4.1}$$

The fields E and B in equations 2.3.17 are tuned in the way, that the reference particle does not oscillate around the reference orbit. Therefore, usually the vector $\mathbb{R}_0$ equals to zero, except for one element $\mathbb{R}_0(3,1) = t_0$, which defines the real time of flight of the particle in the electromagnetic fields. When a whole ring is taken into account t_0 shows the time particle needs to make one revolution. $\mathbb{R}_k(i,j)$ is the matrix element of $\mathbb{R}_k$ that stands in i-th row and j-th column.

Modeling of particle beam dynamics

Each element of the ring is defined by the distribution of E and B fields inside it, the beam dynamics is described by system of equations 2.3.17. Also, each element can be mapped with a $\mathcal{M} = \{\mathbb{R}_0, \mathbb{R}_1, ..., \mathbb{R}_k\}$ of a specified order of non-linearity [10], [11], [12]. Assuming that all the elements are determined by the matrices of the same order will not spoil the generality. So, mathematically a storage ring can be represented as a sequence of maps $\mathcal{M}_1, \mathcal{M}_2, ..., \mathcal{M}_N$, where N is the overall number of elements. The state vector $\mathbf{X}$ may be either written iteratively via sequence of maps mentioned above

$$\begin{aligned} \mathbf{X}_1 &= \mathcal{M}_1 \circ \mathbf{X}_0, \\ \mathbf{X}_2 &= \mathcal{M}_2 \circ \mathbf{X}_1, \\ &... \\ \mathbf{X} &= \mathcal{M}_N \circ \mathbf{X}_{N-1}, \end{aligned}$$

or found using the following formula

$$\mathbf{X} = \mathcal{M}_N \circ \mathcal{M}_{N-1} \circ ...\mathcal{M}_1 \circ \mathbf{X}_0 = \mathcal{M} \circ \mathbf{X}_0,$$

where the resulting map $\mathcal{M}$ is built by simple concatenation of all the maps for a single element, and this procedure is reflected by equation 2.4.1.

All the spin-orbital dynamics in the storage ring one can describe with a number of numerical matrices with the desired order of non-linearity. So in order to get the final state vector of the particle one simply should use the resulting map $\mathcal{M}$ and an initial state vector $\mathbf{X}_0$. That map is a one-turn map but it's easy to build a many-turn map $\mathcal{M}^n = \mathcal{M} \circ \mathcal{M}^{n-1}$.

Moreover, matrix form of the map allows to investigate the dynamics of an ensemble of particles also in matrix form

$$[\mathbf{X}_1, ..., \mathbf{X}_w] = \mathbb{R}_0 + \mathbb{R}_1[\mathbf{X}_{0,1}, ..., \mathbf{X}_0, w] + ... + \mathbb{R}_k[\mathbf{X}^{[k]}_{0,1}, ..., \mathbf{X}^{[k]}_{0,w}], \quad (2.4.2)$$

where the operation of multiplication of a state vector by a matrix changes to the multiplication of a matrix of different state vectors by a corresponded matrix [105], [13].

Calculation of beam parameters

The matrix $\mathbb{R}_1$ in 2.4.1 is a matrix of linear transformation. This matrix is a basis, which is sufficient for finding parameters of a storage ring such as beta-functions and dispersion.

Beta-function is an envelope of the beam in x and y directions [100]. The motion only in $x - x'$ plane is considered, for $y - y'$ plane all the derivation is analogous. The beta-function formation is based on the analysis of the beam envelope that in general form has the following representation

$$\gamma x_0^2 + 2\alpha x_0 x_0' + \beta {x_0'}^2 = 1,$$

or in matrix form

$$\begin{pmatrix} x_0 \\ x_0' \end{pmatrix}^T \begin{pmatrix} \gamma & \alpha \\ \alpha & \beta \end{pmatrix} \begin{pmatrix} x_0 \\ x_0' \end{pmatrix} = 1.$$

The linear part of the transfer map is

$$\begin{pmatrix} x \\ x' \end{pmatrix} = \mathbb{R}_1 \begin{pmatrix} x_0 \\ x_0' \end{pmatrix}, \quad \begin{pmatrix} x_0 \\ x_0' \end{pmatrix} = \mathbb{R}_1^{-1} \begin{pmatrix} x \\ x' \end{pmatrix},$$

where $\mathbb{R}_1$ is the 2×2 matrix, which is a small inner part of the full matrix of the linear order, $\mathbb{R}_1^{-1}$ is the inverse one. Inserting this map into the formula for the envelope one obtains

$$\begin{pmatrix} x \\ x' \end{pmatrix}^T (\mathbb{R}_1^{-1})^T \begin{pmatrix} \gamma & \alpha \\ \alpha & \beta \end{pmatrix} \mathbb{R}_1^{-1} \begin{pmatrix} x \\ x' \end{pmatrix} = 1. \quad (2.4.3)$$

For beta-function calculation one has to find a phase-space ellipse, which transforms into itself after one turn in a storage ring

$$(\mathbb{R}_1^{-1})^T \begin{pmatrix} \gamma & \alpha \\ \alpha & \beta \end{pmatrix} \mathbb{R}_1^{-1} = \begin{pmatrix} \gamma & \alpha \\ \alpha & \beta \end{pmatrix},$$

$$(\mathbb{R}_1^{-1})^T \begin{pmatrix} \gamma & \alpha \\ \alpha & \beta \end{pmatrix} = \begin{pmatrix} \gamma & \alpha \\ \alpha & \beta \end{pmatrix} \mathbb{R}_1$$

For simplicity one defines $(\mathbb{R}_1^{-1})^T = \{m_{i,j}\}_{i,j=1}^2$ and $\mathbb{R}_1 = \{n_{i,j}\}_{i,j=1}^2$. Thus, if to write the last formula by elements, one gets

$$\begin{pmatrix} m_{11}\gamma + m_{12}\alpha & m_{11}\alpha + m_{12}\beta \\ m_{21}\gamma + m_{22}\alpha & m_{21}\alpha + m_{22}\beta \end{pmatrix} - \begin{pmatrix} n_{11}\gamma + n_{21}\alpha & n_{12}\gamma + m_{22}\alpha \\ m_{11}\alpha + n_{21}\beta & n_{12}\alpha + n_{22}\beta \end{pmatrix} = 0$$

$$\begin{pmatrix} (m_{11}-n_{11})\gamma+(m_{12}-n_{21})\alpha & (m_{11}-n_{22}\alpha+m_{12}\beta-n_{12}\gamma \\ m_{21}\gamma+(m_{22}-n11)\alpha-n_{21}\beta & (m_{21}-n_{12}\alpha+(m_{22}-n_{22})\beta \end{pmatrix}=0.$$

If this system of equations has a solution and the envelope exists, the following equations must be true

$$\alpha=\frac{n_{22}-m_{22}}{m_{21}-n12}\beta,\gamma=\frac{(m_{12}-n_{21})(m_{22}-n_{22})}{(m_{11}-n11)(m_{21}-n_{12})}\beta.$$

When the phase-space ellipse coefficients α,β,γ, i.e. optical functions, are known it is possible to observe its dynamics when the beam travels consecutively through the elements. One can define the ellipse matrix as A_0 [105] and the linear matrices of consecutive transformations as $\mathbb{R}_{1,1},\mathbb{R}_{1,2},...$, then

$$\begin{array}{ccccc} A_0 & \to & A_1=\mathbb{R}_{1,1}^{-1^T}A_0\mathbb{R}_{1,1}^{-1} & \to & A_2=\mathbb{R}_{1,2}^{-1^T}A_0\mathbb{R}_{1,2}^{-1}\to ... \\ \downarrow & & \downarrow & & \downarrow \\ \beta_0 & & \beta_1 & & \beta_2 \end{array}.$$

The functions $b_x(s)$ that are defined in certain points $s_0,s_1,s_2,...$, which coincide with the distance traveled by the beam on the reference orbit, are called beta-functions along x coordinate.

Dispersion is another important function needed for an accelerator structure studies. If a particle has any offset from the reference energy $\frac{\delta p}{p}$, it starts to oscillate around the new closed orbit. The value of deviation in x or y directions of the new closed orbit with respect to the reference orbit in each point of the ring is called dispersion.

It is convenient to consider the linearized transformation of the $x,x',\delta p$ coordinates for one turn to build the dispersion function

$$\begin{pmatrix} x \\ x' \\ \delta p \end{pmatrix}=\begin{pmatrix} a_{11} & a_{12} & a_{13} \\ a_{21} & a_{22} & a_{23} \\ 0 & 0 & 1 \end{pmatrix}\begin{pmatrix} x_0 \\ x_0' \\ \delta p_0 \end{pmatrix},$$

where $\delta p=(p-p_0)/p_0$. The given transformation leads to the system of equations

$$\begin{aligned} x&=a_{11}x_0+a_{12}x_0'+a_{13}\delta p_0, \\ y&=a_{21}x_0+a_{22}x_0'+a_{23}\delta p_0. \end{aligned}$$

Taking into account the fact that the orbit must be closed $x=x_0$, $y=y_0$, one obtains

$$\begin{aligned} (1-a_{11})x_0-a_{12}x_0'&=a_{13}\delta p_0, \\ -a_{21}x_0+(1-a_{22})x_0'&=a_{23}\delta p_0. \end{aligned}$$

If this system has a solution, it can be written in matrix form as

$$\begin{pmatrix} x_0 \\ x_0' \end{pmatrix} = \begin{pmatrix} 1 - a_{11} & -a_{12} \\ -a_{21} & 1 - a_{22} \end{pmatrix}^{-1} \begin{pmatrix} a_{13} \\ a_{23} \end{pmatrix} \delta p_0 = \begin{pmatrix} \mathcal{D}\delta p_0 \\ \mathcal{D}'\delta p_0. \end{pmatrix}$$

The function $\mathbb{D}$ in the last equation is the dispersion and may be found with the help of the above algorithm in each point of the accelerator or, if the mapping approach is used, after each element.

Also, it is important to know two other characteristics of the accelerator such as slip factor η and momentum compaction factor α. The first coefficient defines the increase of the time of revolution with respect to the change of initial momentum,

$$\frac{\Delta T}{T} = (\alpha - \frac{1}{\gamma^2})\frac{\Delta p}{p} = \eta\frac{\Delta p}{p},$$

and the second one describes the orbit lengthening

$$\frac{\Delta L}{L} = \alpha\frac{\Delta p}{p}.$$

In order to find the momentum compaction factor one needs to add one more equation $L' = H$ to system of equations 2.3.17, where L is the length of the reference orbit. The solution of this equation in Taylor form reads: $L = L_0 + k\delta p$, and one immediately gets $\alpha = k/L_0$.

Conclusion

The derivation of nonlinear equations describing spin-orbital dynamics of particles in the associated coordinate system was considered in this section. The trajectory equations are represented in the canonical form, which, on one hand, artificially complicates the analytical form but, on the other hand, gives the opportunity for the following realization in program code in the more convenient way. The main ideas of the non-linear matrix approach for particle motion simulations were discussed.

HOW MODE INTEGRATES NUMERICALLY

Introduction to MODE

The mathematical principles of matrix integration, which were discussed in Chapter 2, are realized in newly developed spin-orbital tracking code MODE [51]. The program is written in Saint-Petersburg State University. MODE is an integrated development environment (IDE) that includes (Figure 7) the system of project management, text and visual code editors and the libraries containing all the logic of matrix integration of equations of spin-orbital dynamics. This environment works under Windows operating system and is written with .NET 3.5 platform.

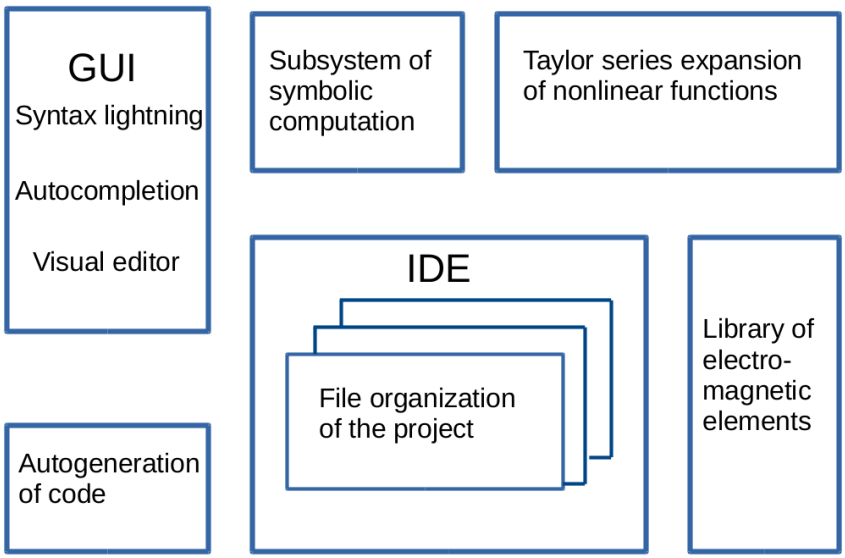

Figure 7: The structure of MODE program.

Although the usage of .NET platform almost excludes the possibility of running the developed environment under Linux operating systems, the given opportunities of the platform allows to reduce significantly time of program codes development and to reach the high desired computational performance [46]. One can point out some advantages of the chosen .NET 3.5 platform. Firstly, one uses specific attributes in the code, which allows to describe meta-data of the code. The programming process transforms, in this case, from procedural into declarative one, which increases the scalability of the program. For example, all the mechanism of auto-completion and the tooltips that pop up automatically use particular class attributes created in the description process of available elements. When new elements are made and the capabilities of the environment

are expanded all needed information will be automatically uploaded and transported to the appropriate modules.

The second important property of .NET 3.5 is the possibility to use dynamical data types. Starting from version 3.5 C# language contains the data type called *dynamic*. The usage of this data type allows to skip the check of an operator type and by doing this increase the speed of code computation.

The last advantage of this platform, when the computational algorithms are used, is the implementation of unmanaged code. The regime of compilation *unsafe* of .NET gives the opportunity to use pointers and operate with data arrays directly inside the memory. All the computational modules, which realize the matrix integration procedures, are written with the usage of pointers without any additional capabilities of .NET platform. This makes the code fully compatible with C ++ language and allows to realize it as a cross-platform library in the future [105].

Mathematical formalism

Consider the system of ODE

$$\frac{d}{dt}\mathbf{X} = \mathbf{F}(t, \mathbf{X}), \tag{2.5.1}$$

where $\mathbf{X} = (x_1 x_2 ... x_n)$ is the state vector of n-th order and $\mathbf{F}$ is the analytical function in the vicinity of $\mathbf{X} = 0$ and is measurable with respect to t in the integration range. If the above conditions are fulfilled, this function can be written as a Taylor series up to the given order of nonlinearity p. That expansion has more convenient representation in matrix form of Taylor series

$$\frac{d}{dt}\mathbf{X} = \mathbb{P}_0(t) + \mathbb{P}_1(t)\mathbf{X} + \mathbb{P}_2(t)\mathbf{X}^{[2]} + ... + \mathbb{P}_p(t)\mathbf{X}^{[p]}, \tag{2.5.2}$$

where $\mathbf{X}^{[k]}$ is the k-th Kronecker power [101], [9] of vector $\mathbf{X}$ with taken into account dimension reduction. The given vector consists of monomials of k-th order written in lexicographical order. For example, for two variable case the required vector could be found using the following expression

$$\begin{pmatrix} x_1 \\ x_2 \end{pmatrix} \otimes \begin{pmatrix} x_1 \\ x_2 \end{pmatrix} = \begin{pmatrix} x_1^2 \\ x_1 x_2 \\ x_2 x_1 \\ x_2^2 \end{pmatrix} \rightarrow \begin{pmatrix} x_1 h^2 \\ x_1 x_2 \\ x_2^2 \end{pmatrix} = \begin{pmatrix} x_1 \\ x_2 \end{pmatrix}^{[2]},$$

where $\otimes$ is the Kronecker matrix multiplication [101]. The elements of the matrices $\mathbb{P}_i, i = 1...p$, in general, depend on time. However, for the stationary systems $\mathbb{P}_i$ are numerical matrices with constant coefficients. If system 2.5.1 is non-stationary, the matrix elements may be arbitrary nonlinear time-dependent functions. In addition, the possibility to expand those functions in Taylor series is not needed.

One should find the solution of equation 2.5.1 with initial conditions $\mathbf{X}(0) = \mathbf{X}_0$ as Taylor series up to desired order k.

$$\mathbf{X}(t) = \mathbb{R}_0(t) + \mathbb{R}_1(t)\mathbf{X}_0 + \mathbb{R}_2(t)\mathbf{X}_0^{[2]} + ... + \mathbb{R}_k(t)\mathbf{X}_0^{[k]}. \tag{2.5.3}$$

When the system is stationary then matrices $\mathbb{R}_j, j = 1...k$ depend only on the value of integration range. All the coefficients will be constant real numbers.

The evolution of elements of matrices $\mathbb{R}_j$ in time can be expressed with the system of ODE. Solving this system of equations with one of the well-known methods, for instance, the Runge-Kutta [59], one can get the numerical estimate of the mapping method [17]. The state vector of such a system will be the sequence of matrices $\mathbb{R}_0(t), \mathbb{R}_1(t), ..., \mathbb{R}_k(t)$, and the initial conditions for the solution will have the form below

$$\mathbb{R}_0(0) = 0,\ \mathbb{R}_1(0) = I,\ \mathbb{R}_2(0) = ... = \mathbb{R}_k(0) = 0, \tag{2.5.4}$$

where I is identical matrix.

The given formulas are easily derivable if one takes into account that any state vector at initial time is equal to itself $\mathbf{X}(0) = \mathbf{X}_0 = I\mathbf{X}_0$. The differentiation with respect to t of equation 2.5.3 leads to the possibility of construction of a system of equations that describe the evolution of the matrix map in time

$$\begin{aligned}
\frac{d}{dt}\mathbf{X} &= \frac{d}{dt}\mathbb{R}_0(t) + \frac{d}{dt}\mathbb{R}_1(t)\mathbf{X}_0 + \frac{d}{dt}\mathbb{R}_2(t)\mathbf{X}_0^{[2]} + ... + \frac{d}{dt}\mathbb{R}_k(t)\mathbf{X}_0^{[k]},\\
\frac{d}{dt}\mathbf{X} &= \mathbb{P}_0(t) + \mathbb{P}_1(t)\mathbf{X} + \mathbb{P}_2(t)\mathbf{X}^{[2]} + ... + \mathbb{P}_p(t)\mathbf{X}^{[p]} =\\
&= \mathbb{P}_0(t) + \mathbb{P}_1(t)\Big(\mathbb{R}_0(t) + \mathbb{R}_1(t)\mathbf{X}_0 + \mathbb{R}_2(t)\mathbf{X}_0^{[2]} + ... + \mathbb{R}_k(t)\mathbf{X}_0^{[k]}\Big) +\\
&+ \mathbb{P}_2(t)\Big(\mathbb{R}_0(t) + \mathbb{R}_1(t)\mathbf{X}_0 + \mathbb{R}_2(t)\mathbf{X}_0^{[2]} + ... + \mathbb{R}_k(t)\mathbf{X}_0^{[k]}\Big)^{[2]} + ...\\
&+ \mathbb{P}_p(t)\Big(\mathbb{R}_0(t) + \mathbb{R}_1(t)\mathbf{X}_0 + \mathbb{R}_2(t)\mathbf{X}_0^{[2]} + ... + \mathbb{R}_k(t)\mathbf{X}_0^{[k]}\Big)^{[p]}
\end{aligned} \tag{2.5.5}$$

After all the simplifications one obtains a system of ordinary differential equations, which defines the dynamics of of matrices $\mathbb{R}_0, \mathbb{R}_1, \mathbb{R}_2, ..., \mathbb{R}_k$.

$$\begin{aligned}
\frac{d}{dt}\mathbb{R}_0(t) &= \sum_{i=1}^{p}\mathbb{P}_i(t)\mathbb{R}_0^{[i]},\\
\frac{d}{dt}\mathbb{R}_k(t) &= \sum_{i=1}^{p}\mathbb{P}_i(t)\frac{\partial\mathbf{X}^{[i]}}{\partial(\mathbf{X}_0^{[i]})^*}, \quad k = 1, 2, ...
\end{aligned} \tag{2.5.6}$$

Solving this system with initial condition 2.5.4 allows to find the desired map [14].

The operations with brackets in equation 2.5.5 should be done with accordance to Kronecker rules of additivity and commutativity with dimension reduction. For instance, $A\mathbf{X}^{[i]} \otimes B\mathbf{X}^{[j]} = (A \otimes B)(\mathbf{X}^{[i]} \otimes \mathbf{Y}^{[j]})$

must be written as $A\mathbf{X}^{[i]} \otimes B\mathbf{X}^{[j]} = C\mathbf{X}^{[i+j]}$, where matrix C is built from $A \otimes B$ by summation and reduction of certain elements. The algorithm, which is realized in MODE, allows to present the solution $\mathbf{X}(t) = \mathbb{R}_0(t) + \mathbb{R}_1(t)\mathbf{X}_0 + \mathbb{R}_2(t)\mathbf{X}_0^{[2]} + ... + \mathbb{R}_k(t)\mathbf{X}_0^{[k]}$ in the matrix form

$$\mathbf{X} = \begin{pmatrix} R_0^1 + (R_1^1, \mathbf{X}_0) + ... + (R_k^1, \mathbf{X}_0^{[k]}) \\ ... \\ R_0^n + (R_1^n, \mathbf{X}_0) + ... + (R_k^n, \mathbf{X}_0^{[k]}) \end{pmatrix},$$

where R_i^j is the j-th row of the matrix $\mathbb{R}_i$ and operator $(\cdot, \cdot)$ is the scalar product of the vectors. The resulting vector can be easily raised to a power with dimension reduction. When this operation is done the new vector, which represents the right Kronecker power, is expanded in a series $\mathbf{X}_0, ..., \mathbf{X}_0^{[k]}$.

Conclusion

The main mathematical basis of MODE program was discussed in detail. The map formalism, which uses MODE was investigated and the derivation of the method for matrix integration of systems of ordinary differential equations was explained.

3

SYSTEMATIC ERRORS IN A STORAGE RING EDM EXPERIMENT

The main problem, which has to be solved, of the future charged particle electric dipole moment experiment at a storage ring is the impact of the different kinds of systematic errors on the signal coming from the presence of the non-vanishing EDM. In this section various sources for systematic errors will be discussed. However, before one starts to investigate their influence on the experimental data and limitations that they put on the sensitivity of the particular measurement method, one should say a couple of words about so-called spin coherence time, which plays crucial role in any storage ring EDM experiment.

INTRODUCTION TO SPIN COHERENCE TIME

The idea of the experiment is to detect a build-up of the polarization of the deuteron beam due to the interaction of the EDM with the electric field (or motional electric field) in the ring. The spin of a particle not only precesses in electric and magnetic fields because of the interaction of its magnetic dipole moment $\vec{\mu}$ with these fields but also for the reason that it has an electric dipole moment. Thus, the equation 2.2.12 may be supplemented by an additional term, which describes that interaction

$$\begin{aligned} \frac{d\vec{S}}{dt} &= \vec{S} \times \vec{\Omega}_{MDM} + \vec{S} \times \vec{\Omega}_{EDM}, \\ \vec{\Omega}_{MDM} &= \frac{e}{\gamma m}\Big(G\gamma\vec{B} - (G - \frac{1}{\gamma^2 - 1})\frac{\vec{E} \times \vec{\beta}}{c} - \frac{G\gamma^2}{\gamma + 1}\vec{\beta}(\vec{\beta} \cdot \vec{B})\Big), \\ \vec{\Omega}_{EDM} &= \frac{e}{m}\frac{\eta}{2}\Big(\frac{\vec{E}}{c} + \vec{\beta} \times \vec{B} - \frac{\gamma}{\gamma + 1}\vec{\beta}(\frac{\vec{\beta} \cdot \vec{E}}{c})\Big), \end{aligned} \tag{3.1.1}$$

where η is the dimensionless parameter characterizing the EDM term. One can introduce the magnetic dipole moment of a particle $\vec{\mu}$ and the electric dipole moment $\vec{d}$.

$$\begin{aligned} \vec{\mu} &= 2(G + 1) \cdot \frac{e}{2m}\vec{S}, \\ \vec{d} &= \eta \cdot \frac{e}{2m}\vec{S}. \end{aligned} \tag{3.1.2}$$

If the EDM is of the order of $10^{-29}\,e{\cdot}$cm, then η of the order of 10^{-15}, which is 14 orders of magnitude smaller than the G factor that for deuterons, for example, equals to -0.143.

The definition of the spin coherence time (SCT) regarding to the example when the "frozen spin" concept will be discussed. As a reminder, the "frozen spin" condition is written as

$$(\frac{1}{\gamma^2-1}-G)(\frac{\vec{\beta}\times\vec{E}}{c})+G\vec{B}=0. \tag{3.1.3}$$

The condition above only works for protons, since deuterons have the negative G factor and in order to fulfill the "frozen spin" condition one should apply a magnetic field, and the equation will have a slightly different form. Nevertheless, all the following discourse is the analogous for both types of particles, so the proton case will be considered.

The equation 3.1.3 makes sure that the spin vector, initially aligned with the momentum in the horizontal plane, rotates with the same frequency as the momentum, in other words, stays "frozen". The radial electric field must be applied in a storage ring. If a proton has the EDM, the spin starts to rotate around the electric field and build a vertical polarization. With the EDM is of the order of $10^{-29}\,e{\cdot}$cm one should wait approximately 1000 seconds to see a build-up of the polarization of 1μrad. During this time all the spins of the particles in the beam must lie along the momentum (be coherent) because as soon as the spins decohere and point in different directions, the EDM will force the spin vectors to rotate either up or down around the electric field according to the direction of the spin of a particular particle. The EDM signal is proportional to $\vec{d}\times\vec{E}$, thus, there will be no net EDM polarization build-up if the spins are not alligned with each other. The time, during which the ensemble of particles completely decohere, is called spin coherence time. This process is presented in Figure 8.

DECOHERENCE EFFECTS IN THE IDEAL RING

The spin coherence time is the first thing one should provide for the upcoming EDM search. One should have a look at the mechanisms, which lead to spin decoherence. The spins of the particles in a bunch decohere due to the fact, that the spin tune of each particle - number of spin oscillations relative to the momentum per one revolution in a ring - depends on its energy and trajectory in electromagnetic fields. Any non-reference particle experiences effects that are connected with orbit lengthening and additional rotations of the spin in the bending and focusing fields, which have nonlinear orders of field decomposition.

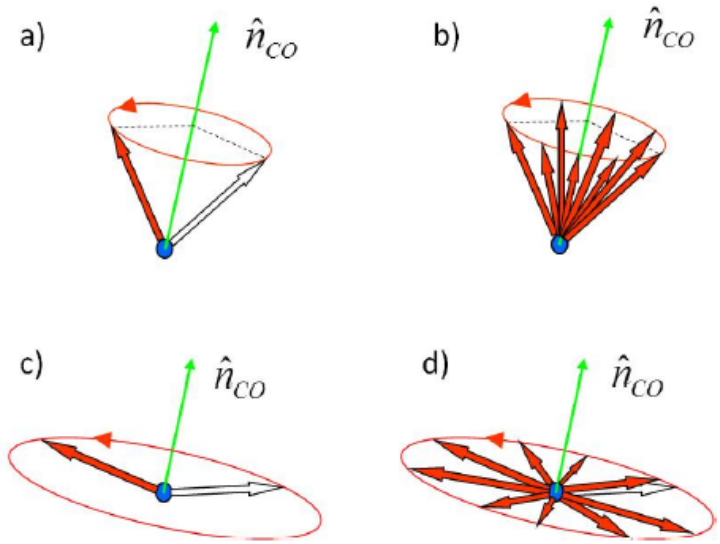

Figure 8: In experiments involving polarized beams in storage rings, one usually does not worry about the coherence of spins along the closed-orbit vector n_{CO}. Shortly after injection, as shown in panel a), all spin vectors are aligned (coherent). After some time, the spin vectors get out of phase and fully populate the cone, as shown in panel b), and this is the situation of a conventional polarization experiment using a stored beam, where the projection of spins along the closed orbit vector,$\vec{S} \parallel n_{CO}$, is the same with and without decoherence. When you deal with a beam polarized along a direction perpendicular to the closed orbit vector,$\vec{S} \perp n_{CO}$, as proposed for high-sensitivity storage ring EDM searches, the situation is very different. Shortly after injection, as shown in panel c), the particle spins may still be coherent, but once they are fully out of phase, as shown in panel d), the polarization component perpendicular to n_{CO} has vanished. Therefore, in a dedicated EDM machine, the observation time is limited by the time it takes the ensemble of particles to decohere, the spin coherence time [48].

Synchronous acceleration principle

For better understanding of the matter of spin decoherence one must firstly consider the basic principle of synchrotronous acceleration. It can be written in a form of a system of equations

$$\begin{aligned} \frac{d\phi}{dt} &= -\omega_{rf}\eta\delta \\ \frac{d\delta}{dt} &= \frac{eV_{rf}\omega_{rf}}{2\pi h\beta^2 E}\sin\phi, \end{aligned} \tag{3.2.1}$$

where $\delta = \frac{\Delta p}{p_s}$ is the relative momentum deviation from equilibrium synchronous level of momentum ($\Delta p = p - p_s$), ϕ is the phase deviation from synchronous phase $\phi_s = 0$, which corresponds to no acceleration in a storage ring, η is the slip factor, E is the full energy, eV_{rf} is the energy gain per turn with V_{rf} voltage gap, $\omega_{rf} = 2\pi h f_{rev}$ is the angular frequency of RF field, h is the harmonic number, $f_{rev} = \frac{1}{T_{rev}}$ is the revolution frequency. [85]

The first equation reflects the concept of synchronous acceleration: a particle with larger energy and, therefore, shorter revolution time arrives earlier at the acceleration region with the lagging phase of the field with respect to ϕ_s. Thus, it gets smaller energy kick, than a particle with the longer revolution time. So the first equation of system 3.2.1 can be presented in the following form

$$\frac{\Delta\phi}{d\phi} = -\frac{\Delta T_{rev}}{T_{rev}}. \tag{3.2.2}$$

Usually, the change of the length of the orbit is given by this formula

$$\frac{\Delta C}{C} = \alpha_0 \cdot \delta,$$

where α_0 is the momentum compaction factor, C is the orbit length. Therefore, one can write down the equation for the relative change in the revolution time through the orbit length change

$$\frac{\Delta T_{rev}}{T_{rev}} = \frac{\Delta(C/v)}{C/v} = \frac{\Delta C}{C} - \frac{\Delta v}{v} = \left(\alpha_0 - \frac{1}{\gamma^2}\right)\cdot\delta, \tag{3.2.3}$$

where the term in brackets is the slip factor $\eta = (\alpha_0 - \frac{1}{\gamma^2})$. Then 3.2.3 is transformed into

$$\frac{\Delta T_{rev}}{T_{rev}} = \eta \cdot \delta. \tag{3.2.4}$$

The average value of the relative revolution time change for one synchrotron oscillation is zero, it follows from the solution of system 3.2.1.

Nevertheless, if one uses higher orders in the expansion of the momentum compaction factor and velocity,

$$\alpha = \alpha_0 + \alpha_1 \cdot \delta$$
$$\frac{1}{v_s + \Delta v} = \frac{1}{v_s}\left[1 - \frac{\Delta v}{v} + \left(\frac{\Delta v}{v}\right)^2 - ...\right]$$

then the equation 3.2.3 takes the form

$$\begin{aligned}\frac{\Delta T_{rev}}{T_{rev}} = \frac{\Delta C}{C} - \frac{\Delta v}{v_s} - \frac{\Delta C}{C}\cdot\frac{\Delta v}{v_s} + \left(\frac{\Delta v}{v_s}\right)^2 = \\ = \left(\alpha_0 - \frac{1}{\gamma^2}\right)\cdot\delta + \left(\alpha_1 - \frac{\alpha_0}{\gamma^2} + \frac{1}{\gamma^4}\right)\cdot\delta^2.\end{aligned} \tag{3.2.5}$$

The betatron motion also brings in an additional term $\left(\frac{\Delta L}{L}\right)_\beta$ into the orbit lengthening. So the previous formula becomes

$$\frac{\Delta T_{rev}}{T_{rev}} = \left(\alpha_0 - \frac{1}{\gamma^2}\right)\cdot\delta + \left(\alpha_1 - \frac{\alpha_0}{\gamma^2} + \frac{1}{\gamma^4}\right)\cdot\delta^2 + \left(\frac{\Delta L}{L}\right)_\beta. \tag{3.2.6}$$

The equation for the longitudinal motion can be written as

$$\begin{aligned}\frac{d\phi}{dt} = -\omega_{rf}\left[\left(\alpha_0 - \frac{1}{\gamma^2}\right)\cdot\delta + \left(\alpha_1 - \frac{\alpha_0}{\gamma^2} + \frac{1}{\gamma^4}\right)\cdot\delta^2 + \left(\frac{\Delta L}{L}\right)_\beta\right] \\ \frac{d\delta}{dt} = \frac{eV_{rf}\omega_{rf}}{2\pi h\beta^2 E}\sin\phi.\end{aligned} \tag{3.2.7}$$

If one assumes that $\phi << 1$ and, therefore, $\cos\phi \approx 1$, one can write the equation for the momentum deviation δ

$$\begin{aligned}\frac{d^2\delta}{dt^2} + \frac{eV_{rf}\omega_{rf}^2}{2\pi h\beta^2 E}\left(\alpha_0 - \frac{1}{\gamma^2}\right)\cdot\delta = \\ = -\frac{eV_{rf}\omega_{rf}^2}{2\pi h\beta^2 E}\cdot\left[\left(\alpha_1 - \frac{\alpha_0}{\gamma^2} + \frac{1}{\gamma^4}\right)\cdot\delta^2 + \left(\frac{\Delta L}{L}\right)_\beta\right].\end{aligned} \tag{3.2.8}$$

It follows from 3.2.6 that the average value $\overline{\Delta T_{rev}/T_{rev}} \neq 0$ is not zero, and it is described by $\alpha_0, \alpha_1, \gamma$ and $(\Delta L/L)_\beta$. Thus,

$$\overline{\frac{\Delta T_{rev}}{T_{rev}}} = \left(\alpha_1 - \frac{\alpha_0}{\gamma^2} + \frac{1}{\gamma^4}\right)\cdot\overline{\delta^2} + \overline{\left(\frac{\Delta L}{L}\right)_\beta}. \tag{3.2.9}$$

Equation 6.2.2 leads to the conclusion that the orbit lengthening must be compensated by the rise of the equilibrium momentum level in order

to be consistent with the synchronous acceleration principle. When 6.2.2 is solved using asymptotic methods [27], one can determine the impact of the betatron oscillation, the momentum compaction factor of the second order α_1 and the slip factor η on the variation of the equilibrium energy level $\Delta\delta_{eq}$

$$\Delta\delta_{eq} = \frac{\gamma_s^2}{\gamma_s^2\alpha_0 - 1}\left[\frac{\delta_m^2}{2}\left(\alpha_1 - \frac{\alpha_0}{\gamma_s^2} + \frac{1}{\gamma_s^4}\right) + \left(\frac{\Delta L}{L}\right)_\beta\right], \tag{3.2.10}$$

where δ_m is the maximum momentum deviation shift.

The equilibrium momentum is different for each particle inside a bunch, that follows from equation 3.2.10. The simulations[84] have been made with COSY Infinity in the electrostatic ring. The equilibrium momentum level increases for the non-reference particle, which experience betatron oscillations, as expected (Figure 9) [85], [90]. The momentum compaction factor of the second order is not equal to zero $\alpha_1 \neq 0$ and the contribution from $(\Delta v/v_s)^2$ are responsible for non-symmetry in the phase trajectories in the longitudinal plane and, thus, lead to a shift of the equilibrium momentum.

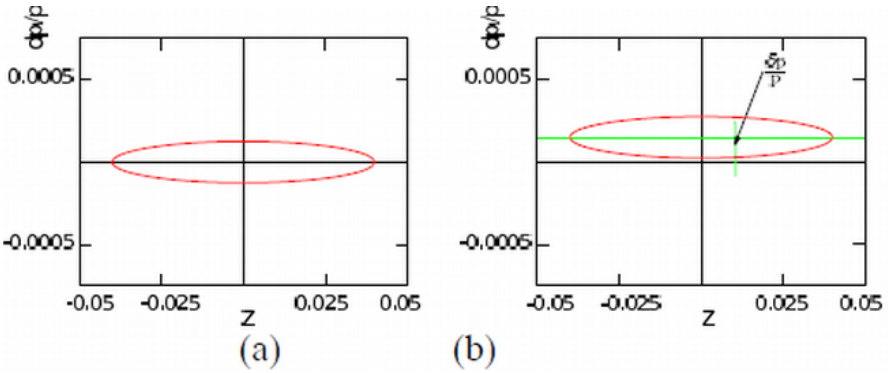

Figure 9: Phase trajectory in longitudinal plane for initial coordinates x=0, y=0 (a) and x=3 mm, y=0 (b)[90].

Figure 10 represents the difference between two cases: the reference particle with zero and non-zero momentum compaction factor of the second order. When $\alpha_1 \neq 0$, one can see the similarity in the phase space pictures with the situation when sextupoles affect the orbit particle motion - the phase space ellipse smoothly transforms into a triangle.

Orbit lengthening

Now, everything is prepared to start to talk about orbit lengthening directly. The first thing when orbit lengthening arises is the situation, when one has any non-reference particle with initial offset in x, y directions, energy deviation is equal to zero for time being.

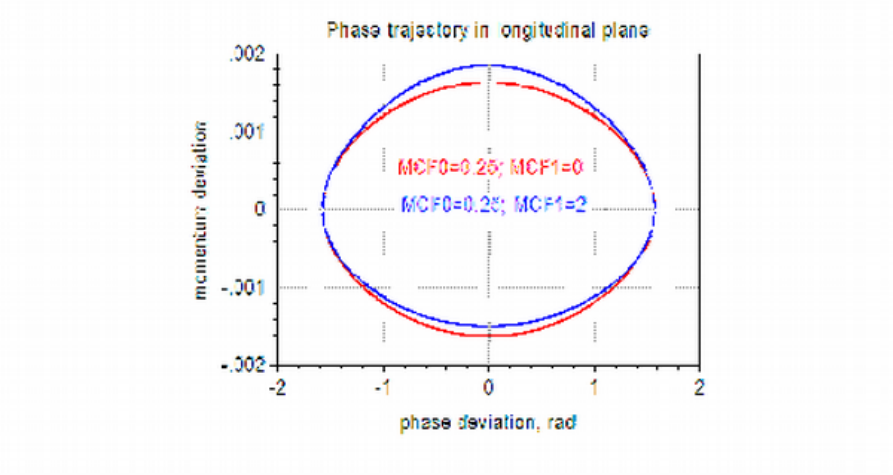

Figure 10: Phase trajectory in longitudinal plane for $\alpha_1 = 0$ and $\alpha_1 \neq 0$ without betatron oscillation [85].

Betatron motion

One can define parameters α_0, α_1 and $(\Delta L/L)_\beta$ using simple geometrical considerations. The momentum spread δ and the betatron oscillation $(\Delta L/L)_\beta$ produce the orbit lengthening, which is illustrated in Figure 11. Firstly, one takes a look at the left side of Figure 11 where the orbit lengthening arises only due to the betatron oscillation. If to assume that a particle has the following coordinates (x_β, x'_β) at a particular time, then because of the larger radius $\rho + x_\beta$ the orbit is longer by a factor of $(\rho + x_\beta)/\rho$ and also the orbit is longer due to the influence of x'_β by a factor of $1/\cos x_\beta$. When the vertical motion is taken into account the lengthening factor is $1/\cos\theta$, where $\theta = \sqrt{x'_\beta + y'_\beta}$.

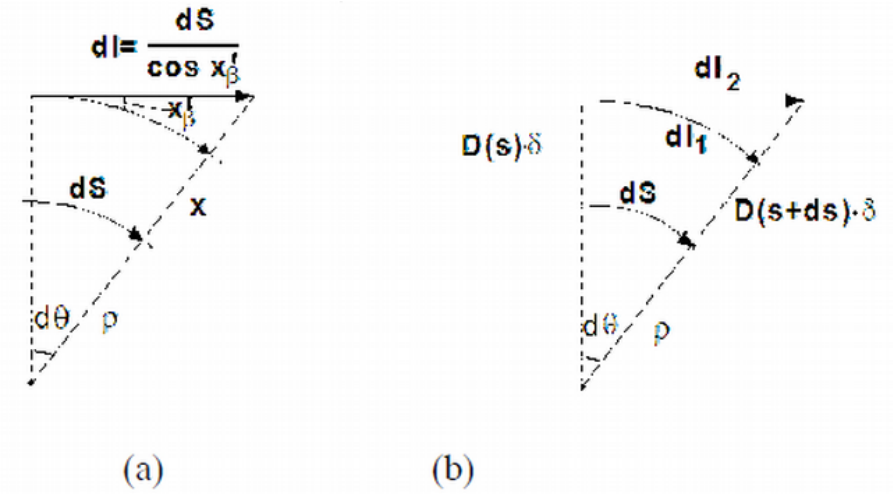

Figure 11: Orbit lengthening due to betatron oscillation (a) and momentum spread (b) [85].

As a result the orbit lengthening produced by the betatron oscillation has the following form

$$\left(\frac{\Delta L}{L}\right)_\beta = \frac{1}{L}\oint\left(\frac{\rho + x_\beta}{\rho\cos\theta} - 1\right)ds = \frac{1}{L}\oint\left(\frac{x_\beta}{\rho} + \frac{{x'_\beta}^2 + {y'_\beta}^2}{2}\right)ds \tag{3.2.11}$$

Since

$$\begin{aligned}\langle\frac{x_\beta}{\rho}\rangle &= 0,\\ \langle x'_\beta\rangle &= \frac{1}{2}\langle\frac{\epsilon_x}{\beta_x}\rangle,\\ \langle y'_\beta\rangle &= \frac{1}{2}\langle\frac{\epsilon_y}{\beta_y}\rangle,\\ \langle\frac{1}{\beta x,y}\rangle &= \frac{\nu_{x,y}}{\overline{R}},\end{aligned}$$

where $\epsilon_{x,y}$ are beam emittances in horizontal and vertical planes and $\beta_{x,y}$ are the corresponding beta-functions and $\nu_{x,y}$ are the horizontal and vertical tunes and $\overline{R}$ is the average radius, the orbit lengthening is represented as

$$\left(\frac{\Delta L}{L}\right)_\beta = \frac{\pi}{2L}\Big[\epsilon_x\nu_x + \epsilon_y\nu_y\Big]. \tag{3.2.12}$$

Momentum deviation

Another contribution to the orbit lengthening comes from the momentum deviation. Let us consider Figure 11b and introduce linear and angular dispersions

$$\begin{aligned}D(s,\delta) &= D_0(s) + D_1(s)\cdot\delta,\\ D'(s,\delta) &= D'_0(s) + D'_1(s)\cdot\delta.\end{aligned} \tag{3.2.13}$$

In an arbitrary position along $ds = \rho d\theta$ one can define

$$\begin{aligned}dl_1 &= (\rho + D_0\delta + D_1\delta^2)d\theta = \left(1 + \frac{D_0}{\rho}\delta + \frac{D_1}{\rho}\delta^2\right)ds,\\ dl_2 &= dl_1\sqrt{1 + (D'_0\delta)^2} = \left(1 + \frac{D_0}{\rho}\delta + \frac{D_1}{\rho}\delta^2\right)\cdot\left(1 + \frac{1}{2}(D'_0\delta)^2\right)ds.\end{aligned} \tag{3.2.14}$$

To summarize:

$$l_2 = \oint\left[1 + \frac{D_0}{\rho}\delta + \left(\frac{D_1}{\rho} + \frac{1}{2}{D'_0}^2\right)\delta^2\right]ds. \tag{3.2.15}$$

Therefore, the orbit lengthening, which appears due to the momentum spread is

$$\begin{aligned} \frac{\Delta C}{C} = \frac{l_2 - C}{C} &= \alpha_0 \delta + \alpha_1 \delta^2 + ..., \\ \alpha_0 &= \langle \frac{D_0}{\rho} \rangle, \\ \alpha_1 &= \langle \frac{D_1}{\rho} \rangle + \frac{1}{2} \langle {D_0'}^2 \rangle \end{aligned} \tag{3.2.16}$$

Subsequently, one can get in the end the total equilibrium momentum shift because of the betatron motion and non-zero momentum compaction factor of the second order.

$$\Delta\delta_{eq} = \frac{\gamma_s^2}{\gamma_s^2 \alpha_0 - 1} \left[\left(\alpha_1 - \frac{\alpha_0}{\gamma_s^2} + \frac{1}{\gamma_s^4} \right) \frac{\delta_m^2}{2} + \frac{\pi}{2L} (\epsilon_x \nu_x + \epsilon_y \nu_y) \right]. \tag{3.2.17}$$

Spin decoherence due to orbit lengthening

Finally, it is all ready to describe spin decoherence effects through the mechanism of orbit lengthening. The spin tune of the reference particle is $\nu_s = G\gamma$. The equilibrium energy shift $\Delta\gamma_{eq}$ depends on the particle parameters, thus the spin tune spread for the N_t turns is given by the following formula

$$2\pi \langle \Delta\nu_s \rangle = 2\pi G \langle \Delta\gamma_{eq} \rangle N_t. \tag{3.2.18}$$

The spread is fully described by the orbit lengthening effects. The spin tune spread limits the spin coherence time.

The following example is considered: the SCT should be of the order of 1000 seconds, which equals to 10^9 turns approximately. If the maximum allowed difference between the direction of the spin of the reference particle and a non-reference one should not exceed 1rad, then one can write

$$\langle \frac{\Delta\gamma_{eq}}{\gamma} \rangle < \frac{1\,\text{rad}}{2\pi\gamma G N_t} = 7 \cdot 10^{-11} \tag{3.2.19}$$

An anticipating EDM build-up has increasing or decreasing behavior, depending on the direction of the longitudinal spin component. If S_z is smaller than zero, the build-up will go down. So, the above formula prevents the EDM from averaging out to zero if fulfilled.

Using 3.2.10, the limit for the momentum spread can be defined as

$$\langle \delta_m^2 \rangle < \langle \frac{\Delta\gamma_{eq}}{\gamma} \rangle \frac{2}{\beta^2} \cdot \frac{\gamma_s^2 (\gamma_s^2 \alpha_0 - 1)}{\gamma_s^4 \alpha_1 - \gamma_s^2 \alpha_0 + 1} \tag{3.2.20}$$

At COSY one has $\alpha_0 = 0.2$, $\gamma_s = 1.25$, $\alpha_1 = 2$, taking zero contribution from betatron motion ($\epsilon_{x,y} \sim 0$) RMS momentum spread should not be larger than $\langle \delta_m \rangle < 8 \cdot 10^{-6}$. Reducing the second order momentum compaction factor down to $\alpha_1 = 0.01$, one obtains $\langle \delta_m \rangle < 2 \cdot 10^{-5}$

For complete elimination of the momentum spread influence on the orbit lengthening the coefficient

$$\alpha_1 - \frac{\alpha_0}{\gamma_s^2} + \frac{1}{\gamma_s^4} = 0 \tag{3.2.21}$$

has to be zero.

For the emittance restrictions one writes

$$\epsilon_{x,y}^{rms} < \langle \frac{\Delta\gamma_{eq}}{\gamma} \rangle \frac{1}{\beta^2} \cdot \frac{\gamma_s^2\alpha_0 - 1}{\gamma_s^2} \cdot \frac{L}{\pi\nu_{x,y}}. \tag{3.2.22}$$

Therefore at COSY with $\langle \delta_m \rangle << 10^{-5}$ the emittance should be $\epsilon_{x,y}^{rms} <$ 1.4mm mrad [85].

MISALIGNMENTS OF THE RING ELEMENTS

In this section the effects of unwanted spin rotations due to the presence of misalignments of the ring elements will be considered. The matter will be discussed in general, since the more aspects of it will be examined in detail later on for the specific methods of EDM searches such as the radio frequency Wien filter method and the quasi-frozen spin approach. Each of those experiments has its own individualities and they must be studied separately.

The rotations of the dipoles play the most significant role, when one talks about misalignments, which spoil the EDM signal.

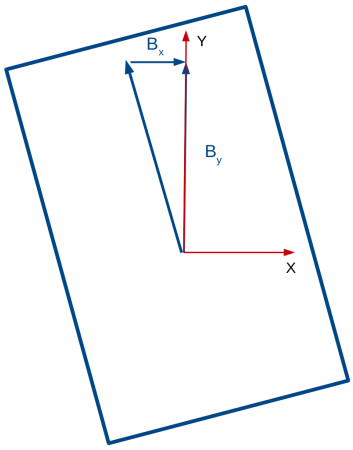

Figure 12: A dipole rotated around the longitudinal axis.

As one can see in Figure 12, the dipole rotation leads to the formation of a B_x component of the magnetic field. This component will rotate the spin via the interaction with the dipole magnetic moment of a particle and that will mimic the effective EDM rotation. Not only the spin motion is perturbed in this scenario but the beam itself starts to experience betatron oscillations, which lead to the orbit lengthening and further depolarization of the bunch. The misalignments of the elements, the

simulations of the spin behavior and the ways of fighting the systematic errors correlated with misalignments will be studied in chapter 6 for three measurement methods.

BERRY'S PHASE EFFECTS

Berry's phase or geometrical phase is, actually, a phenomenon, which comes from quantum mechanics and plays one of the major roles in neutron EDM experiments [7], [50].

In application for an EDM search at a storage ring the geometrical phase is also important and it's connected with the non-commutativity of spin rotations in the ring. If one considers a set of consecutive spin rotations around different axes, so with different angular vectors, which forms a closed loop

$$\sum_i \omega_i t_i = 0, \tag{3.4.1}$$

where ω_i are the angular vectors and t_i are the times, when the rotation occurred, then the integrated spin rotation is not zero. Let $M_i^{\alpha,-\alpha}$ be the spin rotation matrices around any axis $i = x, y, z$ by an angle α or $-\alpha$.

Taking into account the equation written above, one should consider a rotation around the vertical axis and consequently around the longitudinal field, which is non-zero in any accelerator. One can think of an element that rotates back the spin by exactly the same angles around both axis. The resulting rotation is

$$M_y^{\alpha} \cdot M_z^{\phi} \cdot M_y^{-\alpha} \cdot M_z^{-\phi} \neq E, \tag{3.4.2}$$

where $M_{y,z}^{\pm\alpha,\pm\phi}$ are the rotation matrices around the vertical and longitudinal axes rotating the spin vector by $\pm\alpha$ and $\pm\phi$, E is the identity matrix. After such a rotation the spin vector that initially was longitudinally polarized will acquire the vertical component, which mimics the EDM signal. However, if one inverts the matrices $M_{y,z}^{\alpha,\phi}$ and writes the following transformation

$$M_y^{\alpha} \cdot M_z^{\phi} \cdot (M_y^{\alpha})^{-1} \cdot (M_z^{\phi})^{-1} = E, \tag{3.4.3}$$

it will be equal to the identity matrix, and no vertical component will be produced. Here comes the idea of clockwise and counter-clockwise stored beams, which will be described in detail in chapter 6.

Conclusion

In this chapter the principle of spin coherence time was discussed, which is the basic measure for the future EDM experiments. The SCT should be not less than one thousand seconds to successfully measure an EDM polarization build-up.

Also the main sources of systematic errors were considered. Orbit lengthening, which occurs because of the energy spread in a bunch and

the finite size of it, leads to depolarization. Misalignments of the ring elements seriously affect the spin motion and produce fake EDM signal. Finally, the geometrical phase impact on the behavior of the spin was examined. An EDM contribution to the vertical spin component can be mimicked by the geometrical phase, which arises when two consecutive rotations around the vertical and the longitudinal axis are present.

4

BENCHMARKING OF MODE PROGRAM

SIMULATIONS OF SPIN TUNE SHIFTS DURING EXTRACTION

For the past several years the Cooler Synchrotron (COSY) in Forschungszentrum Jülich has been used as a facility for test runs for the upcoming precursor experiment for the EDM search. One of the aims of those test was to identify the optimal settings of the machine for the longest spin coherence time.

Autumn run of 2013 was performed with approximately 10^9 deuterons in the beam, they were accelerated up to 970 MeV and stored for 140 seconds inside the ring. The beam was cooled with an electron cooler to reduce the equilibrium beam emittance, and the relative momentum spread $\frac{\Delta p}{p}$ was of the order of 10^{-5}. The beam was initially vertically vector polarized, $p_\epsilon^+ = 0.57 \pm 0.01$ for the up-state and $p_\epsilon^- = -0.49 \pm 0.01$ for the down-state, the tensor polarization was less than 0.02. The RF cavity was on, so the beam was bunched. When the beam preparation was over the electron cooler was turned off and the measurement was taken for the remaining 100 seconds.

The RF solenoid was operated at the spin resonance frequency to rotate the spin from vertical to horizontal direction. The beam was slowly extracted onto the internal carbon target. There were three different ways of extraction: the white noise electric field extraction and the vertical and horizontal extractions with extraction magnets. The purpose was to see how the spin tune is affected by an extraction method. Scattered deuterons were detected in the scintillation detectors, consisting of rings and bars around the beam pipe [40] and the energy deposit was measured in the outer scintillator rings. The times of arrival of each particle with respect to the beginning of each cycle and the COSY RF cavity frequency were recorded in the long-range time-to-digital (TDC) converter. The number of orbit revolutions could be, therefore, exactly assigned to each recorded event [18] [38].

The spin tune was measured with the tremendous relative precision of 10^{-9} per cycle [38]. It was observed that during the extraction process the spin tune was drifted from its initial value. The experiment showed that the horizontal extraction affected the spin tune stronger than the other two methods. This process was considered and simulated in MODE to benchmark the program.

The extraction of the beam was made using two horizontal steerers with linearly increasing magnetic fields. The simulation result is presented in Figure 13 [30]. The following picture (Figure 14) shows the actual

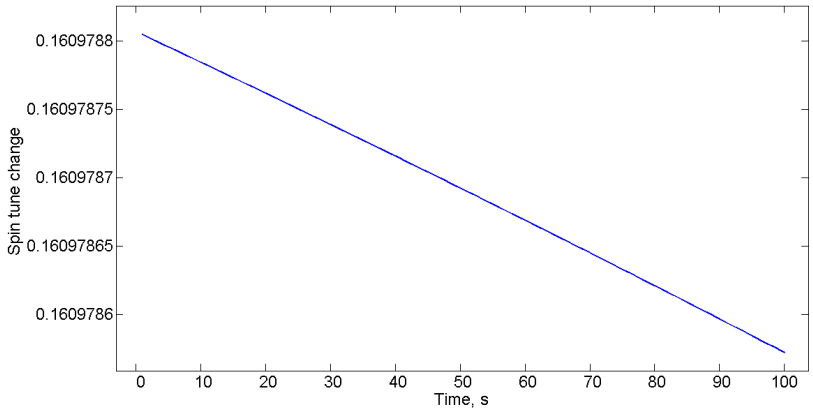

Figure 13: The simulation of the spin tune change during the horizontal extraction at the COSY.

experimental results.

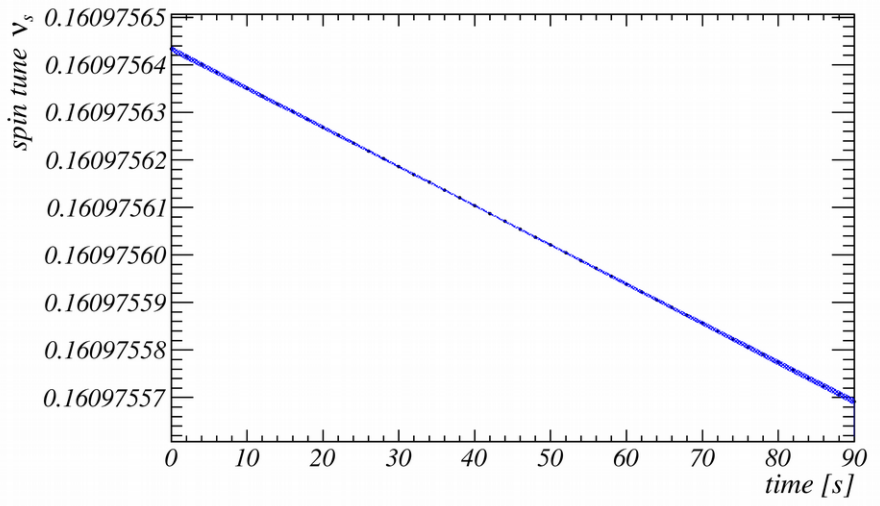

Figure 14: The experimental results of the spin tune change during the horizontal extraction at COSY.

It was obesrved experimentally that during the extraction the absolute spin tune change was approximately $\delta\nu_s = 2.53 \cdot 10^{-7}$. As one can see in the picture, the spin tune changes slightly slower in the simulation ($\delta\nu_s = 2.25 \cdot 10^{-7}$), which testifies for the fact that not all of the existent fields were properly described or taken into account. One can see that MODE correctly describes the orbital and spin motion. The program was also benchmarked with the different experimental set-up.

SIMULATION OF SPIN TUNE SHIFTS IN THE PRESENCE OF TWO STEERERS

In September 2014 the series of test runs was performed. Besides the SCT studies there were runs for the investigation of systematic errors in the ring.

The idea was to study the effects on the beam parameters, caused by the misalignments in the ring, using the steerers which excite an orbit. It was proposed to use different steerer sets: a horizontal and a vertical steerer placed either in the straight section or in the arc of the COSY. They were turned on separately and also in pairs - two horizontal ones, for example, which were located in the opposite straight sections. The steerers then kick the beam in the vertical or in the horizontal direction imitating a presence of the imperfection field. The corresponding spin tune shift was measured afterwards. The experimental scheme is depicted in Figure 15.

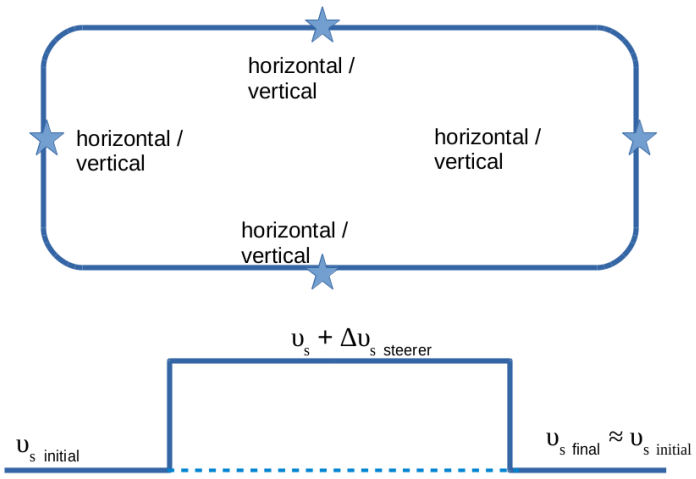

Figure 15: The scheme of the experimental set-up for 2014 September run at the COSY.

The measurement started after the beam preparation, as usual. The beam was slowly extracted, as was explained in the previous section, the white noise electric field extraction was chosen because the smallest spin tune drift was observed only in this case. The spin tune drift during the white noise extraction is shown in Figure 16 [38].

Not only because of the smallest spin tune drift the white noise extraction method was used but due to the fact that this approach allows to kick the particle from the beam randomly, from random "layers" of the bunch.

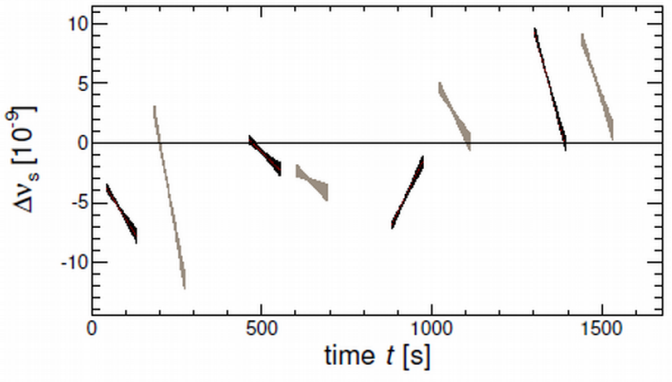

Figure 16: Drift of the spin tune during eigth consecutive cycles with alternating initial vector polarization p_ϵ^+ (black) and p_ϵ^- (gray) [38]

.

This makes possible to work with the whole size of the beam and, therefore, detect the true value of the spin tune, which is averaged over the emittance size. In other words, this technique doesn't extract the beam "cut by cut" - of course the spin coherence time, in this case, is large and infinitely long for the infinitely thin "slice". White noise extraction moves the measured spin tune value closer to the real one.

Figure 15 represents the timing of the experiment. When the extraction started the spin tune was measured for first 20 seconds without any additional steerer fields. Then the steerer was turned on and the spin tune tune shift was observed, after 40 seconds time the steerer was again off and the spin tune was measured again. This procedure was done in order to exclude any changes of the spin tune due to the factors apart from steerer's influence. Figure 17 shows the spin tune shift due to the steerer impact. It is clearly visible that the spin tune is affected by the steerers.

The impact of the steerers on the spin tune was primarily determined by the orbit lengthening and the location of the steerer in the ring. The following pictures shows the spin tune change as a function of the steerer strength (see Figure 18, 19).

The simulations were made with MODE. The original lattice of COSY ring was fully modeled in the program. All elements were randomly shifted along x, y and z directions and rotated around radial, vertical and longitudinal axes. The steerer kick was simulated with the implementation of a special element, which was written specifically for this purpose. Five different random seeds were selected for each simulation dedicated to the particular steerer that was used.

Figures 18, 19 show the experimental points measured during the experiment and the simulation results for different random seeds. The measured spin tune shifts linearly depend on the steerer strength despite of

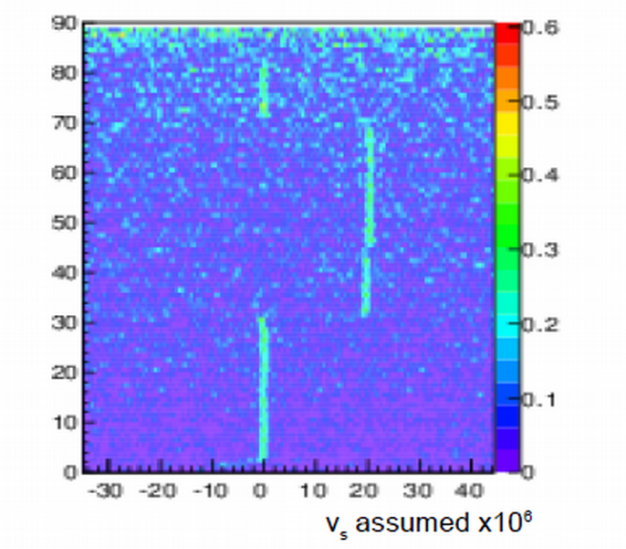

Figure 17: The experimentally measured spin tune shift induced by the steerer

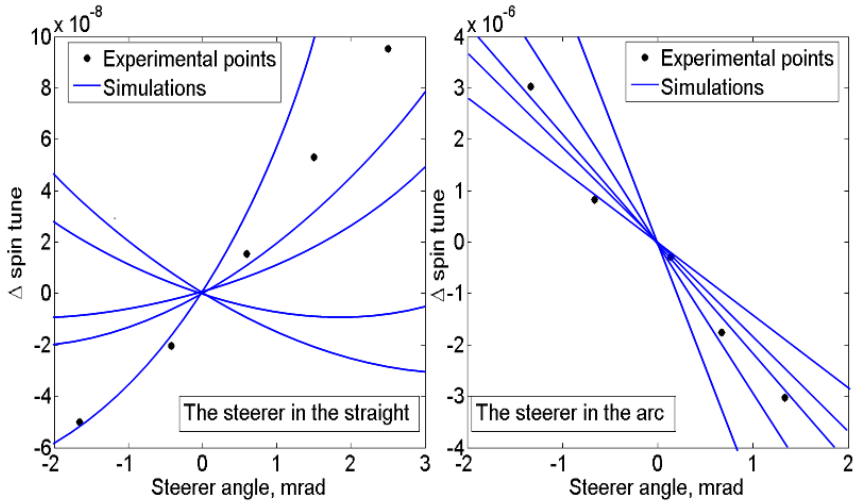

Figure 18: The experimental spin tune shifts for different horizontal steerer strengths and the simulations with different random seeds of misalignment errors.

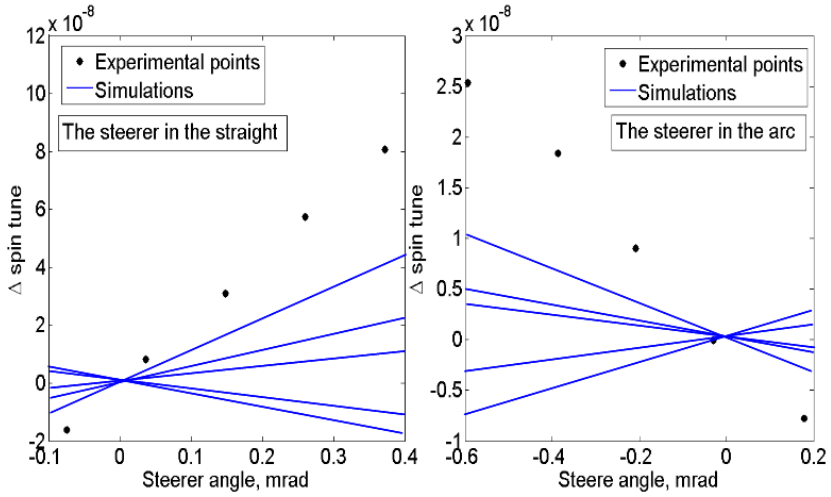

Figure 19: The experimental spin tune shifts for different vertical steerer strengths and the simulations with different random seeds of misalignment errors.

the location of the steerer for both planes. However, theory predicts that the spin tune shift should be sensitive to the position of the steerer.

A steerer kicks the beam, for instance, in horizontal plane. Particles' x coordinates change in accordance with Hill's differential equations. The square root of the *beta* function determines a particle x coordinate in the straight section, where the dispersion is zero, and a larger linear contribution from the dispersion function mainly determines that coordinate in the arc. The spin tune change is proportional to the orbit lengthening and, therefore, to the change in particles' coordinates. That is why, one should expect quadratic dependence of the spin tune shift if a steerer located in the straight sections and a linear dependence for the steerers in the arcs. In the vertical plane COSY ring has no dispersion at all. So quadratic behavior of the spin tune change is expected.

The experimental points for each steerer setting form a straight line, since the range of the steerer strength is not broad enough to see the quadratic behavior. The range was set at its maximum, when the field was increased further the beam was lost.

The blue curves in the plots from the simulation results strongly depend on the random seed of the misalignments, which was chosen. Quadratic behavior of the simulated spin tune change for the case of the horizontal steerer placed in the straight section was in agreement with the theoretical predictions. Nevertheless, it couldn't fully describe the data. The linear spin tune change for the horizontal steerer in the arc was in the best accordance with the measured data points. Both simulations for the vertical steerer case demonstrated the linear dependence on the steerer

kick, since the range of the steerer strength was too close to zero, so one couldn't see the parabolic shapes of the curves. The simulations didn't fully coincide with the data, however, the change of the spin tune had at least the same magnitude.

In conclusion, one can say that the steerer kicks affect the spin-orbital motion and cause shifts of the spin tune. The spin tune change strongly depends on the particular misalignment set, which is present in the machine. Simulations cannot fully describe the data, since the model of the whole accelerator should be improved. For example, cooling process was not taken into account, the solenoid fields, either. Nevertheless, MODE results have the same order of magnitude as the experimental ones and for some cases they are in well agreement with the experiment. This is the indication that the program works correctly, can be used in the following studies and its results are correct.

5

THE METHODS FOR EDM MEASUREMENT AT A STORAGE RING

INTRODUCTION

In this chapter three methods for an EDM measurement will be discussed. The main idea and the experimental principle will be explained for each of the approaches. All methods will be considered for the ideal machine with one single reference particle, since this way is easy and sufficient to demonstrate the possible way of EDM determination. Previously described systematic errors will be studied in detail in the next chapter for each method, together with the procedures for their compensation.

THE FROZEN SPIN METHOD

Introduction

To search for a proton EDM using a ring with purely electrostatic elements, the concept of the frozen spin method has been proposed [95]. This method is based on two facts: in the equation of spin precession, the magnetic field dependence is entirely eliminated, and at the "magic" energy, the spin precession frequency coincides with the precession frequency of the particle momentum. In case of deuterons one has to use electric and magnetic fields simultaneously, as will be explained later, keeping the frozen spin direction along the momentum as in the pure electrostatic ring.

The frozen spin [95] is based on the fact that at a certain so-called "magic" energy, a particle spin begins to rotate with the frequency of the momentum and always lies along the momentum. Under this condi-

tion, the signal growth of presumably existing electric dipole moment is maximized. This is clearly evident from the T-BMT equations

$$\begin{aligned} \frac{d\vec{S}}{dt} &= \vec{S} \times (\vec{\omega_G} + \vec{\omega}_{EDM}) \\ \vec{\omega_G} &= -\frac{e}{m}\left[G\vec{B} + \left(\frac{1}{\gamma^2 - 1} - G\right)\frac{\vec{\beta} \times \vec{E}}{c}\right] \\ \vec{\omega}_{EDM} &= \frac{e\eta}{m}\left[\vec{\beta} \times \vec{B} + \frac{\vec{E}}{c}\right] \\ \vec{\mu} &= 2(G+1)\frac{e}{2m}\vec{S} \\ \vec{d} &= \eta\frac{e}{2m}\vec{S}, \end{aligned} \tag{5.2.1}$$

where G is the anomalous magnetic moment, which contributes to the dipole magnetic moment $\vec{\mu}$, $\vec{\omega_G}$ is the spin precession frequency due to the magnetic dipole moment (MDM precession) relative to the momentum, $\vec{\omega}_{EDM}$ is the spin precession frequency due to the electric dipole moment (EDM precession) and and η is the dimensionless coefficient defined, which is used to describe the EDM.

It is reasonable to implement the frozen spin method in a purely electrostatic machine with electric deflectors keeping a beam on orbit. The advantages of purely electrostatic machines are especially evident at the "magic" energy, where

$$G - \frac{1}{\gamma_{mag}^2 - 1} = 0, \tag{5.2.2}$$

and the spin is oriented in the longitudinal direction. It rotates in the horizontal plane with the same frequency as the momentum, which is $\omega_G = 0$ [95].

However, this method cannot be used for deuterons, which have negative anomalous magnetic moment $G = -0.143$ [80]. That follows from condition 5.2.2. Therefore, the only possible method in this case is a storage ring with both electric and magnetic fields [86], [87]. The frozen spin condition, in this case, will be written as

$$\left(\frac{1}{\gamma^2 - 1} - G\right)\frac{\vec{\beta} \times \vec{E}}{c} + G\vec{B} = 0. \tag{5.2.3}$$

It was proposed to store a longitudinally polarized deuteron beam of 1 GeV/c total momentum in an electro-magnetic storage ring of 0.5 T. Spin precession frequency due to the interaction of magnetic dipole moment with electro-magnetic fields of the ring should be zero. This can be done by applying a radial electric field of magnitude

$$E_r = \frac{GBc\beta\gamma^2}{1 - G\beta^2\gamma^2} \approx GBc\beta\gamma^2 \tag{5.2.4}$$

to cancel the $G \cdot \vec{B}$ contribution to ω_G in 5.2.1.

One should also fulfill the usual equilibrium condition, which keeps the beam on orbit. It is simply the equality of Lorentz force to the centrifugal force

$$e[-\vec{E} + c\beta \times \vec{B}] = \frac{\gamma m V^2}{R}, \tag{5.2.5}$$

where R is the ring radius and V is the particle velocity. Inserting equation 5.2.4 into 5.2.5 one gets

$$\frac{ecB_y}{\frac{1}{\gamma^2-1} + |G|} = \frac{\gamma m V^2}{R}. \tag{5.2.6}$$

Completing all the calculation, the radius of the ring is

$$R = \frac{|G|}{(|G|-1)} \left[\frac{mc^2}{eE}\right] \gamma^3 \beta^2. \tag{5.2.7}$$

One clearly sees that the radius depends on anomalous magnetic moment of a particle (deuteron in our case), mass, energy and the strength of electric field. The kinetic energy of deuterons is 270 MeV, the electric field is 120 kV/cm and a deuteron mass is $3.34 \cdot 10^{-27}$ kg. That yields a radius of the ring, which is equal to ≈ 9.21 m. The length of the ring, including space for beam-position monitors, sextupoles, drift sections that are long enough to install the required beam diagnostic equipment, is 145.84 m. The ring and the beta functions with the dispersion are shown in Figures 20 and 21 below.

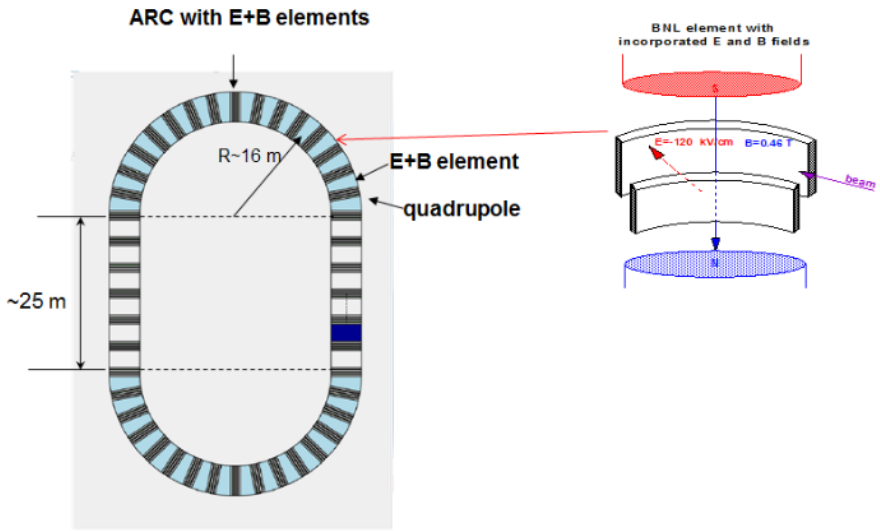

Figure 20: The lattice for the frozen spin experimental method for deuteron beam with 270 MeV kinetic energy.

The E+B elements used in the lattice design are called BNL elements because it was initially proposed to create such a device at BNL [8]. The element is composed of a simple electric cylindrical deflector and a dipole magnet.

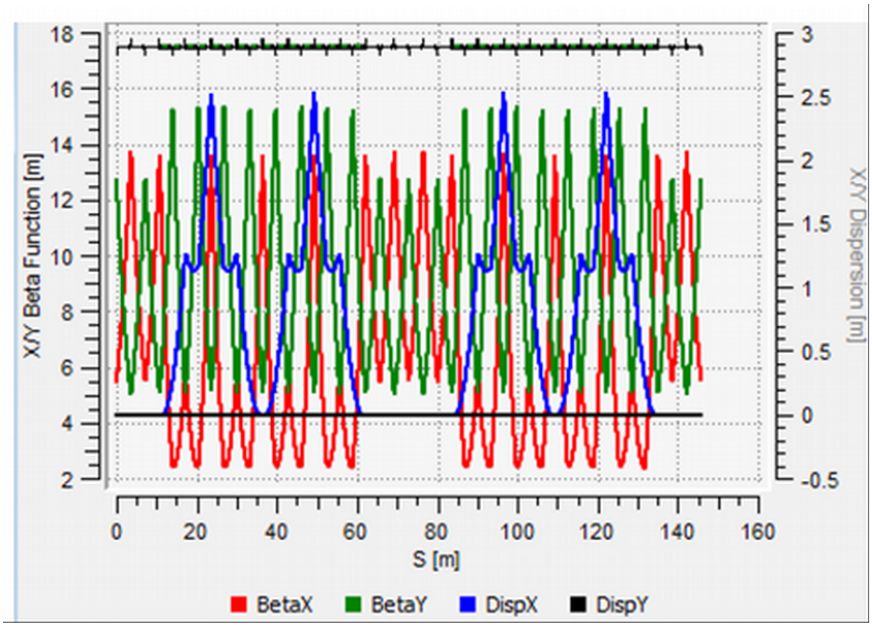

Figure 21: The beta functions and the dispersion for the frozen spin method.

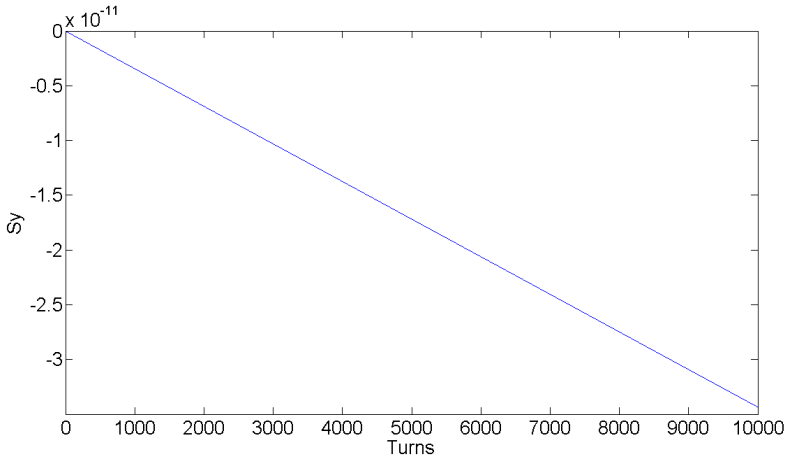

Figure 22: The polarization build-up in the vertical plane for the frozen spin measuring method. The EDM was $\sim 10^{-29}\, e \cdot \mathrm{cm}$.

The simulation for a single reference particle was performed. The EDM value was chosen to be $\sim 10^{-29}\, e{\cdot}$cm. One sees the EDM build-up of approximately $3.5 \cdot 10^{-15}$ per turn.

THE QUASI-FROZEN SPIN METHOD

Introduction

The quasi-frozen spin (QFS) method [87] introduces a new idea, in which the spin oscillates around the momentum direction within the half value of the advanced spin phase in magnetic arcs, each time returning back in electrostatic arcs. Due to the low value of the anomalous magnetic moment of deuteron, an effective contribution to the expected EDM effect is reduced only by a few percent compared with the frozen spin method.

The concept of quasi-frozen spin

The only requirement of the frozen spin condition is to maximize the EDM signal growth. However, if the spin oscillates in the horizontal plane with respect to the frozen spin direction with amplitude Φ_s, the EDM growth decreases proportionally to the factor $J_0(\Phi_s) \approx 1 - \frac{\Phi_s^2}{4}$.

Taking into account that the anomalous magnetic moment for deuteron $G = -0.143$ has a small value and assuming that the spin oscillates around the momentum direction within the half value of the advanced spin phase $\pi G\gamma/2n$, each time returning back by special optics with n-periodicity. Due to the low value of the anomalous magnetic moment of deuteron, the effective contribution to the expected EDM effect is reduced only by a few percent.

This allows one to proceed to the concept of quasi-frozen spin, where the spin is not frozen with respect to the momentum vector, but continually oscillates around some average fixed direction coinciding with the momentum direction. After all, one has to answer the question how to implement a variable MDM spin precession in the storage ring and to provide a sufficient EDM signal rise.

Now, the spin equation in an electric deflector and in a bending magnet will be considered separately. From the T-BMT equation in the laboratory coordinate system, it follows that MDM spin precession in the radial driving electrical field is

$$\omega_G^E = -\frac{e}{m}\left[\left(G + \frac{1}{1+\gamma}\right)\frac{\vec{\beta}\times\vec{E}}{c}\right]. \tag{5.3.1}$$

At the same time, the frequency of particle momentum precession in the laboratory coordinate system inside E field is

$$\Omega_p^E = \frac{e}{mc}\frac{\vec{E}\times\vec{\beta}}{\gamma\beta^2}. \tag{5.3.2}$$

Subtracting 5.3.2 from 5.3.1 and normalizing the difference by 5.3.2, it is possible to obtain the spin tune in the electric deflector relative to the momentum

$$\nu_s^E = \left[\frac{1}{\gamma^2 - 1} - G\right]\gamma\beta^2. \tag{5.3.3}$$

Performing the same actions for the magnetic field, in the bend magnet, the frequency of MDM spin precession in the laboratory frame is

$$\omega_G^B = -\frac{e}{mc}\left(G + \frac{1}{\gamma}\right)cB, \tag{5.3.4}$$

and the frequency of momentum precession in real space inside B field is

$$\Omega_p^B = \frac{e}{mc}\frac{Bc}{\gamma}. \tag{5.3.5}$$

Similarly, the spin tune in a magnetic field relative to the momentum is

$$\nu_s^B = \gamma G. \tag{5.3.6}$$

One can define the ratio of 5.3.3 and 5.3.6. Figure 23 shows that ratio

$$K = \frac{\nu_s^E}{\nu_s^B}, \tag{5.3.7}$$

between the spin tune in electric and magnetic fields relative to a particle momentum versus energy.

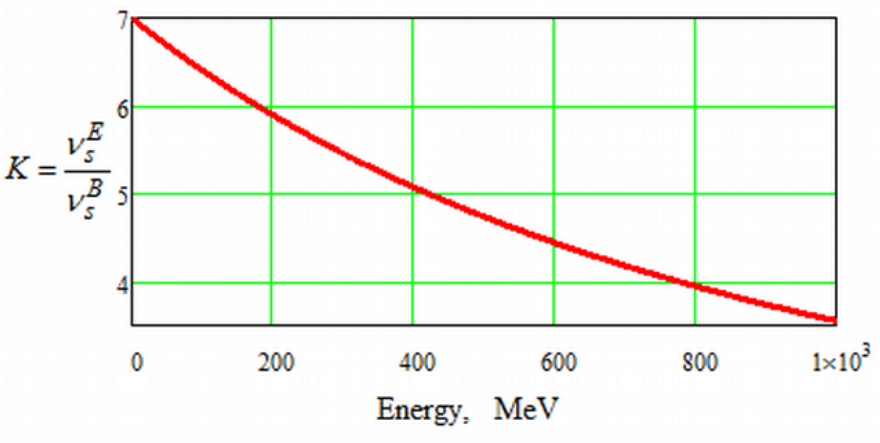

Figure 23: The ratio ν_s^E/ν_s^B vs beam energy.

Thus, one can see that there is an energy region, where the MDM spin oscillation in the electric field is several times faster than in the magnetic field. Due to this fact, the idea of the quasi-frozen structure can be implemented on the basis of two types of arcs: magnetostatic and electrostatic with negative curvature.

The lattice is created by two parts: two magnetic arcs with bend magnets, rotating the particle by an angle $\Phi^B = (\pi + 2\alpha)$ per arc and providing the MDM spin rotation in the horizontal plane relative to the momentum by an angle $\Phi_s^B = \nu_s^B \Phi^B$, and two electrostatic arcs with electric deflectors with negative curvature, rotating the beam by an angle $\Phi^E = -2\alpha$ per arc and providing the MDM spin rotation in the horizontal plane relative to the momentum in opposite direction by an angle $\Phi_s^E = \nu_s^E \Phi^E$. To realize the quasi-frozen spin concept, it is necessary to fulfil that condition and ensure $\Phi_s^E = -\Phi_s^B$. Since in the electrostatic deflector the spin is rotated with the frequency, which is by the factor of $K = \nu_s^E / \nu_s^B$ faster than in magnetostatic structure, we have the basic relation for two different arcs

$$\begin{aligned} \nu_s^B \cdot (\pi + 2\alpha) &= \nu_s^E \cdot 2\alpha \\ \alpha &= \frac{0.5 \cdot \pi}{\nu_s^E / \nu_s^B - 1}. \end{aligned} \tag{5.3.8}$$

Following the principles of this idea, it is obvious that the electrostatic and magnetostatic parts have an arbitrary geometry with the single condition:

$$\sum_i \Phi_i^E \nu_s^E = \sum_j -\Phi_j^B \nu_s^B, \tag{5.3.9}$$

where Φ_i^E, Φ_j^B are the momentum angle rotations in i-th electrostatic and j-th magnetostatic element of structure respectively. The sequence of magnetic and electrostatic elements in the ring is also arbitrary and determined by the beam dynamics. So, turn by turn, the MDM spin rotation in magnetostatic part is compensated by MDM spin rotation in electrostatic part.

Obviously, this oscillation should lead to the EDM signal reduction. However, due to the small amplitudes of Φ_s^E and Φ_s^B, the growth of the EDM signal is reduced in comparison to the fixed spin direction case by the factor

$$J_0(\Phi_s^{E,B}) \approx 1 - \frac{(\Phi_s^{E,B})^2}{4}, \tag{5.3.10}$$

which is ~ 0.98 in the case for 270 MeV.

Figure 24 shows an example of the ring for the deuteron energy of 270 MeV based on the QFS concept. This energy was chosen, since the cross-section for deuteron elastic scattering, which is used in polarimetry, has the appropriate value.

The quasi-frozen spin condition must be fulfilled. The lattice was calculated with bending magnets of 1.5 T and electric deflectors with 120 kV/cm $E-$field. This yields the ring length of 166 m and two bending radii for electric and magnetic elements of the ring respectively: $R^E \approx 42.1$ m and $R^B \approx 2.3$ m. Cylindrical deflectors were used in the

lattice design. This feature leads to the some aspects of the spin motion, which will be discussed later. The beta functions together with the dispersion are pictured in Figure 25. The lattice is shown in Figure 24.

In addition, there is another lowering factor directly affecting the EDM signal, and it is common for both the frozen and quasi-"frozen" spin concepts. As one can see from the T-BMT equation, the EDM signal in electrostatic and magnetostatic parts of the ring will grow with different signs, partially compensating itself. One can estimate this lowering factor as well. Since the EDM signal is proportional to the Lorentz force

$$dS_{E,B}^{EDM} \sim \frac{e\eta}{mc}\left(c\beta_z B_y - E_x\right) \cdot dt, \tag{5.3.11}$$

it is obviously proportional to the path length L^E, L^B and inversely proportional to the radii of curvature R^E, R^B in electrostatic and magnetostatic parts, that is, to the angle of beam rotation Φ^E and Φ^B in the corresponding structure

$$\begin{aligned} dS_E^{EDM} &\sim \frac{L^E}{R^E} = \Phi^E \\ dS_B^{EDM} &\sim \frac{L^B}{R^B} = \Phi^B \end{aligned} \tag{5.3.12}$$

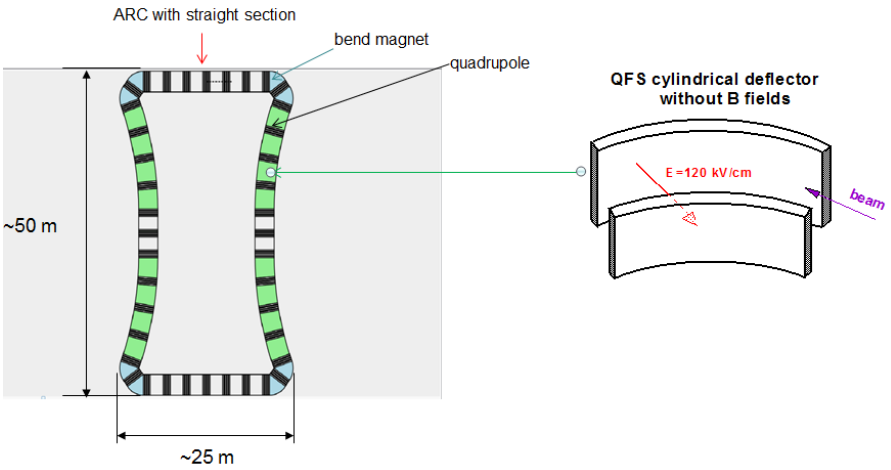

Figure 24: The lattice for the quasi-frozen spin method.

As a result, it is true that the ratio between the values of the EDM signal is determined by the ratio of the rotation angles in two structures, which, in turn, is determined by K

$$\frac{dS_B^{EDM}}{dS_E^{EDM}} = \frac{\Phi^B}{\Phi^E} = \frac{\nu_s^E}{\nu_s^B} \approx 7 \div 5. \tag{5.3.13}$$

Thus, the second lowering factor is about $0.85 \div 0.80$, which is not a substantial reduction of the EDM signal.

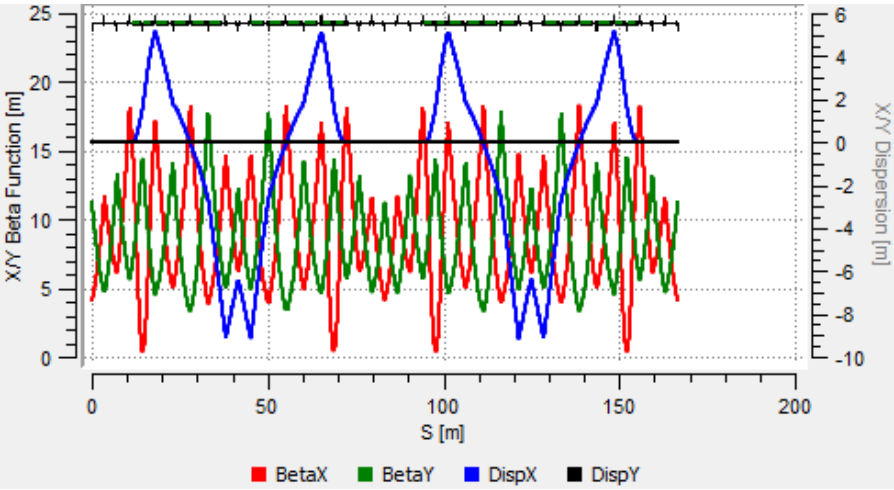

Figure 25: Dispersion and beta functions for the quasi-frozen spin lattice.

To make sure that this is true, a numerical simulation of 3D spin-orbital motion, using MODE program, was performed. Figure 26 shows the variation of the horizontal component of spin S_x along the ring. One sees that the deviation of the spin in the horizontal plane is periodic and that it remains at the same level $\sim \pm 0.3$. Due to oscillation, which is assumed in the quasi-frozen spin method, the EDM signal decreases by 1%. Besides, in each magnet, the EDM signal grows by $2.14 \cdot 10^{-16}$, and in each deflector it decreases by $3.2 \cdot 10^{-17}$. The simulation was performed for an EDM of $\sim 10^{-29}\, e{\cdot}\mathrm{cm}$

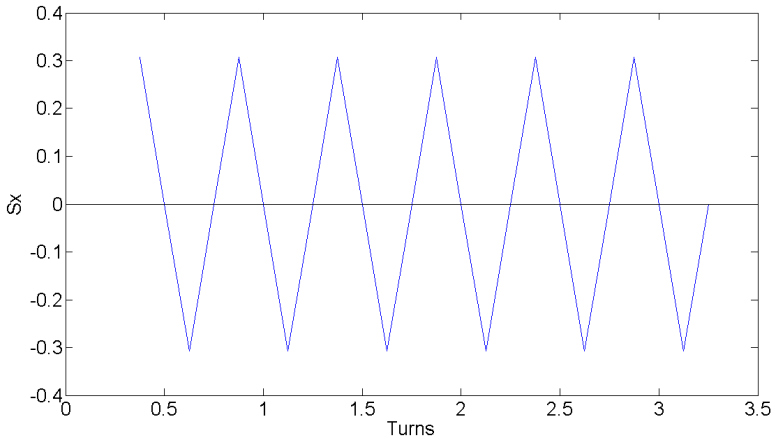

Figure 26: Variation of S_x spin component during the beam storage.

As a result, the total EDM signal grows by $-3.5 \cdot 10^{-15}$ per turn, and in order to get the total EDM signal to be $\sim 10^{-6}$, one has to keep the beam in the ring for the duration of $N_{turn} \sim 10^9$ turns or $\sim 1000\,\mathrm{s}$ (see Figure 27).

The quasi-frozen spin method for deuteron is based on the following fundamental principles. Firstly, in a certain region of energy, the MDM

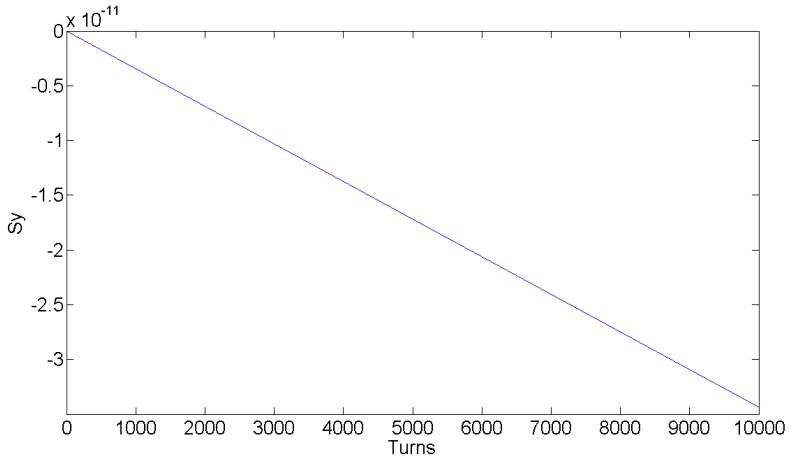

Figure 27: The polarization build-up in the vertical plane for the quasi-frozen spin method due to the presence of non-vanishing EDM of the order of $10^{-15}\,e$·cm.

spin precession relative to the momentum in the electric field is faster by factor $6-7$ than in the magnetic field. Secondly, in the same region of energy, the EDM spin precession is faster by the same factor $6-7$ in the magnetic field than in the electric field. Therefore, in case of different signs of curvatures in the magnetic and electrostatic field, the MDM spin rotation relative to the momentum can be compensated and one should observe the EDM signal.

RADIO FREQUENCY WIEN FILTER METHOD

Introduction

Two previous methods need a new ring to be built. The JEDI collaboration proposed to perform a precursor experiment with the existing COSY ring at the Forschungszentrum in Jülich [63]. For this purpose the RF Wien filter method was created by our collaboration and it is well suited for the initial test of the future experimental approach. With this method, one can analyze the impact of systematic errors, investigate the ways for their correction at the real machine, not only on paper or in simulations, and, finally, perform the first experiment on a charged particle EDM determination. The deuteron beam with the momentum of $970\,\mathrm{MeV}/c$ is planned to be used for the precursor.

The measurement principle of RF Wien filter method

COSY ring is a pure magnetic ring with electric field equals to zero. In such a machine, an EDM interacts with the motional electric field,

according to the T-BMT equation in the presence of a vertical magnetic field

$$\begin{aligned} \frac{d\vec{S}}{dt} &= \vec{S} \times (\vec{\omega}_{MDM} + \vec{\omega}_{EDM}) \\ \vec{\omega_{MDM}} &= -\frac{e}{m} G\vec{B} \\ \vec{\omega}_{EDM} &= \frac{e\eta}{m} \vec{\beta} \times \vec{B} \\ \vec{\mu} &= 2(G+1)\frac{e}{2m}\vec{S} \\ \vec{d} &= \eta \frac{e}{2m}\vec{S}. \end{aligned} \tag{5.4.1}$$

This interaction tilts the spin closed orbit

$$\vec{n_{co}} = n_1\vec{e}_x + n_2\vec{e}_y + n_3\vec{e}_z. \tag{5.4.2}$$

This vector indicates the direction, around which the spin rotates.

Using 5.4.1, one can write the following formula for the spin precession frequency, when the spin closed orbit is tilted due to the EDM interaction with the motional electric field.

$$\begin{aligned} \vec{\Omega} &= -\frac{e}{m}\left\{ G\vec{B} + \eta\vec{\beta} \times \vec{B} \right\} = \\ &= \Omega_R \frac{G\gamma}{\cos\xi} \cos\xi\vec{e_y} + \sin\xi\vec{e_x}. \end{aligned} \tag{5.4.3}$$

The spin tune will be modified

$$\nu_s = \frac{G\gamma}{\cos\xi}, \quad \tan\xi = \eta. \tag{5.4.4}$$

It was proposed to use a Wien filter with a strong radial electric field in this case. The Lorentz force inside such a device equals to zero in the particle rest frame, and therefore it has no influence on the EDM.

$$\vec{E} + \vec{\beta} \times \vec{B} = 0. \tag{5.4.5}$$

However, the interaction of the magnetic dipole moment (MDM) with the combined motional and direct magnetic fields leads to an additional kick in the spin precession. This MDM kick, together with the interaction of the EDM with the motional electric field in COSY ring, yields the spin rotation around the radial axis and produces a build-up of a vertical or horizontal polarization, depending on the initial spin orientation, which increases linearly with time. In the absence of the RF Wien filter the same EDM interaction in the ring results in the small oscillating signal, which doesn't grow with time.

The RF Wien filter has a radial electric E_x and a vertical magnetic B_y field. It must be operated on a harmonic K of the spin motion,

$$f_{WF} = |K + G\gamma| f_{rev}, \tag{5.4.6}$$

where f_{WF} is the frequency of the harmonically excited RF Wien filter and f_{rev} is the beam revolution frequency. That device should not excite any betatron oscillations in the machine, so the alignment of it and other elements in COSY plays a crucial role in the experiment [31].

RF Wien filter commisioning

The JEDI collaboration has made the first operating RF Wien filter and successfully installed it at COSY. The RF-B part of the Wien filter consists of a 560 mm long coil made out of 6 mm copper tubes with 8 windings around a titanium coated, ceramic section of the vacuum chamber (see Figure 28) [72]. Ferrites are used to flatten the field distribution in the transverse plane and increase the maximum flux in the central beam plane up to 0.59 mT at the maximum current amplitude of $\hat{I} = 10\text{A}$ (see Figure 28a). The resulting integrated field along the beam axis is $\int \hat{B}_x dl = 0.33\,\text{Tmm}$. The total inductance of the system is $L = 30\,\mu\text{H}$.

The electric part of the RF Wien filter consists of two stainless steel electrodes (AISI 316L), mounted inside the vacuum chamber and made out of 50 μm thin foil. Due to the large penetration depth of $\delta \approx 450\,\mu\text{m}$ in this material, the overall damping of the external magnetic field is negligible. The electrodes are spanned over glass rods held by a frame inside the flanges of the ceramic vacuum chamber (see Figure 30). The edges are bent with a radius of 3 mm, providing high voltage proofing inside the UHV of COSY up to $\approx 50\,\text{kV}$ (see Figure 29b). For deuterons at 970 MeV/c (Lorentz $\beta = 0.459$) compensation occurs at an impedance of

$$Z = \frac{E_x}{H_y} = -\frac{E_y}{H_x} = Z_0 \beta_z = 173\,\Omega. \tag{5.4.7}$$

At an electrode distance of 54 mm, the required potential on each electrode for the field compensation is $\pm 3936\,\text{V}$, leading to a maximum vertical electric field amplitude of $\hat{E_y} = 75.840\,\text{kV/m}$ (see Figure 31a).

The RF Wien filter is operated at the first few harmonics of the spin tune $(\gamma G + K) f_{rev}$. Within the momentum range at COSY, this involves frequencies of 100 kHz to 2000 kHz. The RF power is supplied by two separate frequency-generator and amplifier pairs. Adjustable capacitors (see Figure 30) together with the coil in case of the RF-B dipole and a 180° phase splitter between the electrodes in the case of the RF-E dipole form two parallel resonance circuits. This provides the possibility of tuning the system to the required range of resonance frequencies while simultaneously matching the circuits' impedances to $50\,\Omega$ [72].

RF Wien filter and an EDM build-up

COSY ring (see Figure 32) was modeled in MODE program. It has the length of approximately 183 m and the bending radius for the dipoles

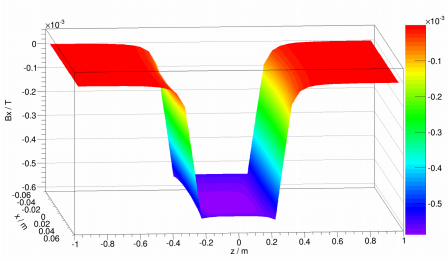

(a) Magnetic field distribution [72].

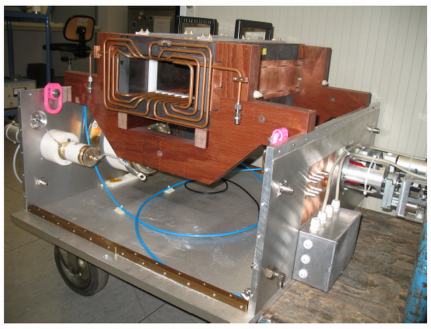

(b) The RF coil with ferrites in the laboratory[72].

Figure 28: The RF-B dipole.

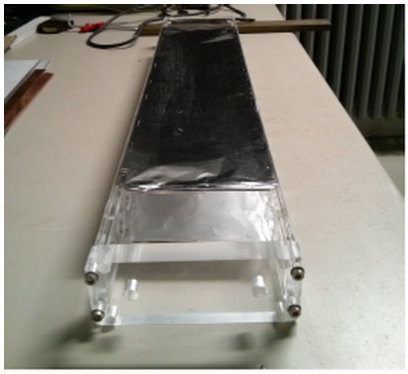

(a) Magnetic field distribution [72].

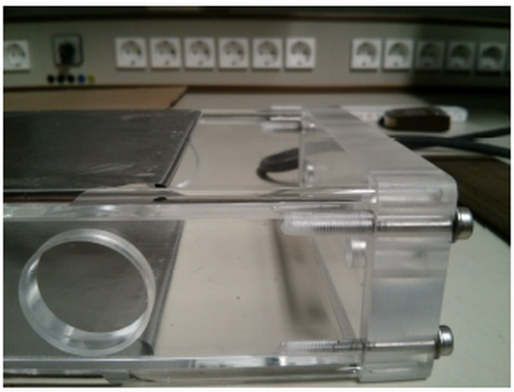

(b) The RF coil with ferrites in the laboratory [72].

Figure 29: The RF-B dipole.

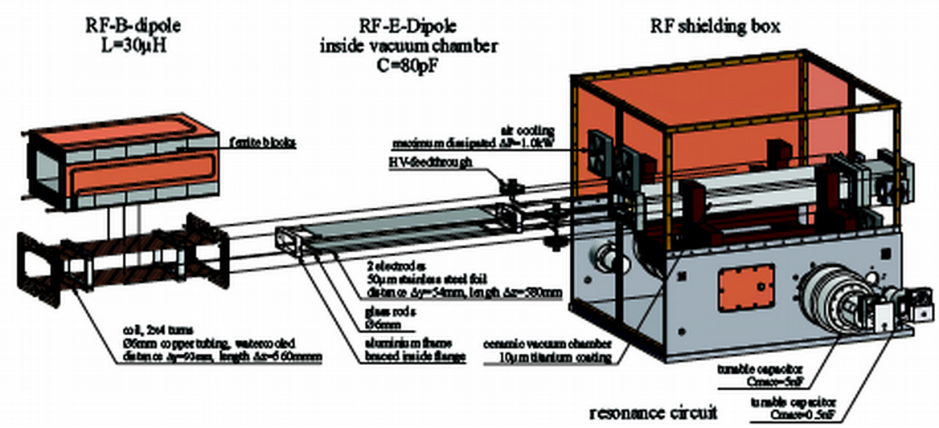

Figure 30: The components of the RF Wien filter [72].

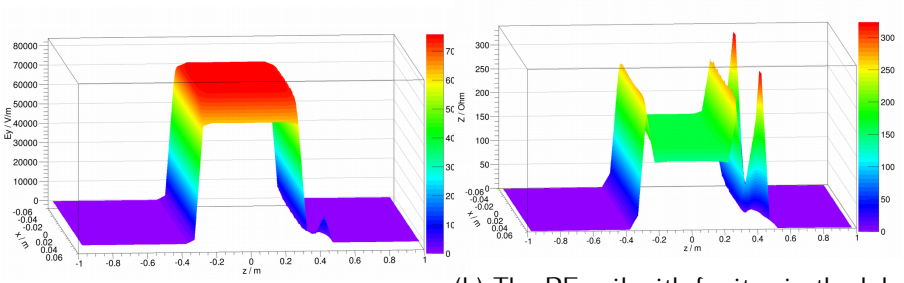

(a) Magnetic field distribution [72].

(b) The RF coil with ferrites in the laboratory [72].

Figure 31: The RF-B dipole.

in the arcs equals to 7 m. As was mentioned above, there were no magnet misalignments, the frequency of the Wien filter was perfectly matched with the resonance spin frequency, the Wien filter itself was ideally placed in the ring and no field errors occurred.

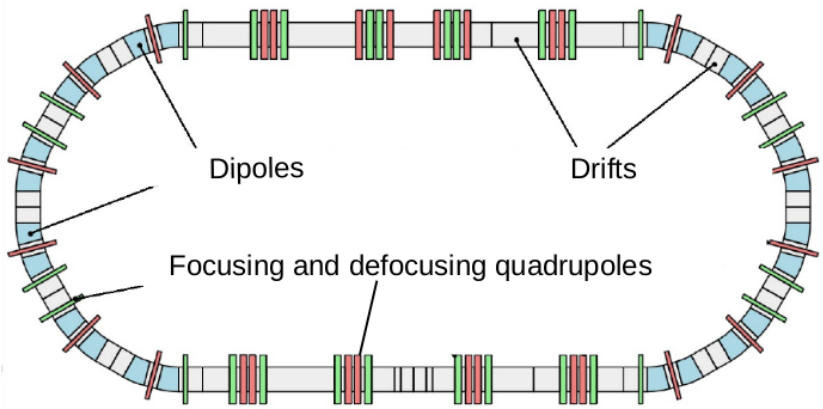

Figure 32: The lattice of COSY ring.

The electric field of the Wien filter was set to 10 kV/cm. The magnetic field was calculated by formula 5.4.5. Longitudinally polarized deuteron with the momentum of 970 MeV/c located right on the closed orbit was tracked through the ring 10^4 times. The build-up of a vertical polarization was observed, as expected. The EDM was set to be equal to $\approx 10^{-21}\, e \cdot$ cm. The polarization in the vertical plane was calculated by the following formula

$$S_y = \sqrt{S_x^2 + S_z^2}. \tag{5.4.8}$$

Figure 33 represents that build-up. One observes not a thin line but rather a band because this rise of the polarization is modulated by the Wien filter. So if one zooms in, the oscillations will be clearly visible. The width of the band, i.e. the amplitude of the polarization oscillations, is directly proportional to the EDM value. The smaller the EDM, the thinner the line. The rate of the EDM signal growth is $\approx 10^{-7}$ per turn

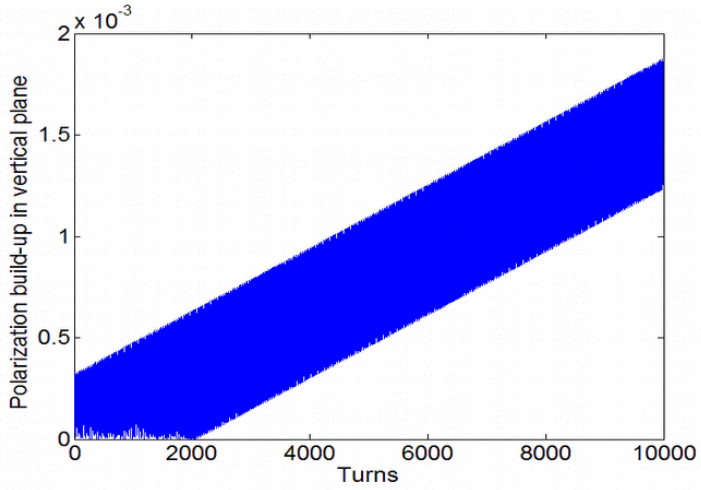

Figure 33: The polarization build-up due to EDM interaction with the motional electric field in the whole ring with Wien filter on. $\eta = 10^{-6}$, which corresponds to EDM is equal to $2.63 \cdot 10^{-21}\, e \cdot \mathrm{cm}$.

and it also scales linearly with the EDM value or the Wien filter field strength.

CONCLUSIONS

Three approaches for possible EDM measurement were discussed in this chapter. Two of them, the frozen spin and the quasi-frozen spin methods, are dedicated to the "final" experiment and the RF Wien filter method is for the precursor run. The lattice designs were shown and the technical parameters for each ring were listed. The simulation results, which demonstrated the the build-up of the anticipated EDM signal for a reference particle, were studied. All methods have a potential for a charged particle EDM determination at a storage ring.

6

SYSTEMATIC ERRORS FOR DIFFERENT EDM MEASUREMENT METHODS

SYSTEMATIC ERRORS FOR THE FROZEN AND THE QUASI-FROZEN SPIN METHODS

Introduction

The systematic errors, which play a crucial role in the future search for an EDM of a charged particle at a storage ring, will be discussed further. Since the frozen spin and the quasi-frozen spin methods are similar, it is reasonable to combine them and describe in a single section. The ways for error compensation are also identical for both methods, although one gets different results when maximizing the spin coherence time, for example. This main difference will be examined in this section, too.

The general impact of systematic errors on the spin-orbital motion has already been described in chapter 3. However, the detailed discussion will be made in this section. The comparison of two methods will be made and for both of them the advantages and disadvantages will be listed.

Spin coherence time for the frozen and the quasi-frozen spin methods

Spin coherence time prolongation with a radio frequency cavity

Radio frequency (RF) cavities are usually used for acceleration, bunching or deceleration of the beam. However, an RF cavity increases spin coherence time, moreover it is impossible to have the SCT close to 1000 seconds. One can take a closer look at one of the methods, for instance, at the quasi-frozen spin. Using this example, the impact of an RF cavity on the SCT will be discussed.

First of all, one should write the quasi-frozen spin condition for the laboratory coordinate system in the following form

$$\gamma G \Phi_B = \left(\frac{1}{\gamma}(1 - G) + \gamma G \right) \Phi_E, \tag{6.1.1}$$

where $\Phi_{B,E}$ are the angles of the momentum rotation in the magnetic/electric part of the ring. For the spin tunes in both parts one gets:

$$\begin{aligned} \nu_E &= \left(\frac{1}{\gamma}(1-G)+\gamma G\right)\Phi_E \\ \nu_B &= \gamma G \Phi_B \end{aligned} \tag{6.1.2}$$

This condition is fulfilled only for the reference particle. One should consider a particle with energy deviation from the reference one. A series expansion can be done in the vicinity of γ_0 for this purpose

$$\begin{aligned} \gamma G\Phi_B &= \gamma_0 G\Phi_B + G\Phi_B\Delta\gamma \\ \left(\frac{1}{\gamma}(1-G)+G\gamma\right)\Phi_E &= \left[\frac{1}{\gamma_0}(1-G)+\gamma_0 G\right]\Phi_E + \Delta\gamma G\Phi_E - \\ &\quad -\frac{1}{\gamma_0^2}(1-G)\Delta\gamma\Phi_E + \frac{1}{\gamma_0^3}(1-G)\Phi_E\frac{\Delta\gamma^2}{2}. \end{aligned} \tag{6.1.3}$$

The total angle of the spin rotation of a non-reference particle per one revolution in the ring will be equal to

$$\begin{aligned} \Phi_B^s - \Phi_E^s &= \gamma_0 G\Phi_B + G\Phi_B\Delta\gamma - \left[\frac{1}{\gamma_0}(1-G)+\gamma_0 G\right]\Phi_E - \Delta\gamma G\Phi_E + \\ &\quad + \frac{1}{\gamma_0^2}(1-G)\Delta\gamma\Phi_E - \frac{1}{\gamma_0^3}(1-G)\Phi_E\frac{\Delta\gamma^2}{2} = \\ &= \Delta\gamma G(\Phi_B-\Phi_E) + \frac{1}{\gamma_0^2}(1-G)\Delta\gamma\Phi_E - \frac{1}{\gamma_0^3}(1-G)\frac{\Delta\gamma^2}{2}\Phi_E. \end{aligned} \tag{6.1.4}$$

The above equation shows that the quasi-frozen spin condition is violated for a non-reference particle. The S_x component of the spin vector will differ from zero. Leaving only the linear terms in 6.1.4, one can write a system of equations

$$\begin{aligned} \gamma_0 G\Phi_B &= \left[\frac{1}{\gamma_0}(1-G)+\gamma_0 G\right]\Phi_E \\ \Delta\Phi_{B,E}^s = \Phi_B^s - \Phi_E^s &= \Delta\gamma G(\Phi_B-\Phi_E) + \Delta\gamma\frac{1}{\gamma_0^2}(1-G)\Phi_E. \end{aligned} \tag{6.1.5}$$

The first equation of 6.1.5 is the quasi-frozen spin condition - equality of the spin precession in magnetic and electric parts of the ring. The second one defines the difference between the angles of spin rotations in two parts of the ring for a non-reference particle. Actually, one can consider this difference as a difference between spin rotations of the reference and a non-reference particles. The first condition is mandatory, so inserting it in the second one, one gets

$$\Delta\Phi_{B,E}^s = 2\Delta\gamma\frac{1}{\gamma_0^2}(1-G)\Phi_E. \tag{6.1.6}$$

RF cavity makes it possible to get rid of the difference in the spin precession. For example, for deuteron beam with G factor of -0.143, $\Phi_E = 0.68$, a typical $\Delta\gamma = 10^{-4}$ and deuteron energy of 270 MeV [85]

$$2\Delta\gamma\frac{1}{\gamma_0}^2(1-G)\Phi_E \approx 2\cdot 10^{-4}\frac{1}{1.14^2}0.86\cdot 0.68 \approx 10^{-4}. \tag{6.1.7}$$

The formula above shows that for 10^4 turns the angle between the spins of the reference and a non-reference particle will be around 1 rad. The voltage and the frequency of a RF cavity should be tuned in such a way that a particle would experience the number of synchrotron oscillations that would average out $\Delta\gamma$ effects. In other words, the longitudinal tune ν_z, which is the number of longitudinal oscillations per turn, must be larger than the spin tune ν_s by several orders of magnitude.

$$\nu_z = \frac{1}{\beta_s}\sqrt{\frac{eUh\eta}{2\pi E_s}} \gg \nu_s = \gamma G\cdot\frac{\Delta\gamma}{\gamma}, \tag{6.1.8}$$

where e is the elementary charge, U is the voltage between the electrodes, h is the harmonic number, η is the slip factor and E_s and β_s are the energy and relative velocity of the reference particle.

That is, if per one turn $\Delta\Phi^s_{B,E} \approx 10^{-4}$, then the number of oscillations per revolution should be around $10^{-2} - 10^{-1}$ to smear out this difference.

Let us have a look how it's done by a RF cavity. Figure 34 demonstrates the voltage value of a RF cavity depending on time. $\Phi_s = 0$ is the working

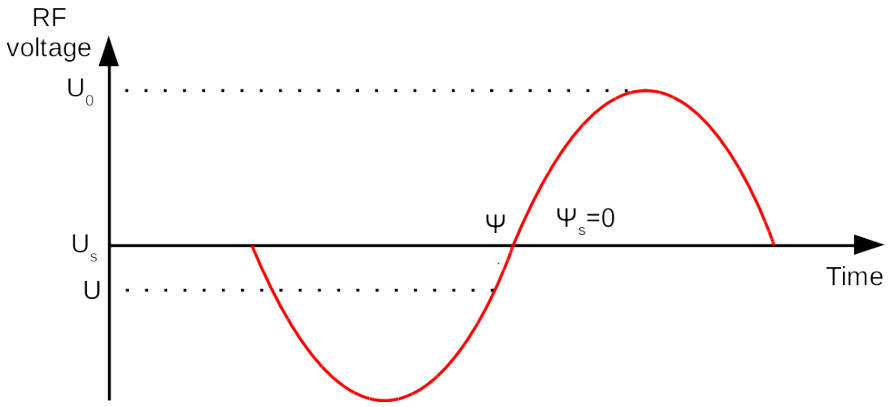

Figure 34: Value of RF voltage in time.

phase of a RF cavity, which was used in the simulations, $U_s = 0$ is the corresponding voltage and U_0 is the maximum voltage at the electrodes. The energy kick obtained by a particle passing through a region where the cavity was installed can be written as [65]

$$\Delta E = eU_0\sin\Phi_s, \tag{6.1.9}$$

where e is the elementary charge. The phase is chosen in the way that the reference particle would get a zero energy kick, particles with larger

energy would be decelerated and ones with smaller energy would be accelerated in the electric field of the cavity. As was mentioned earlier, the particles will experience synchrotron oscillations around the reference energy value. All those particles will be trapped in a separatrix - a longitudinal phase-space region, which defines a longitudinal size of the particle bunch. The separatrix for the simulations for the frozen spin method is pictured below (Figure 35).

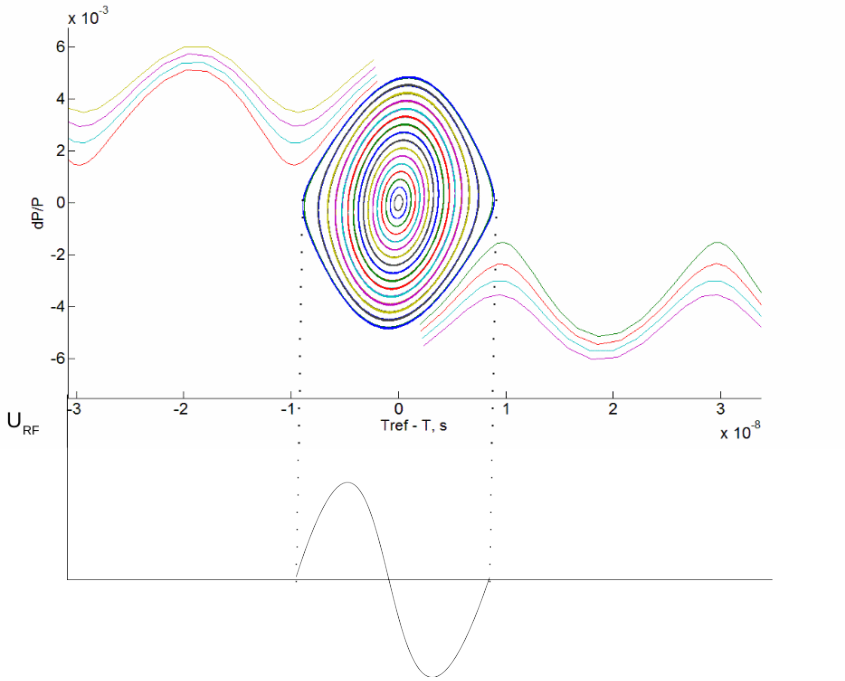

Figure 35: Separatrix for the frozen spin method.

The picture represents different particles with various initial energy offsets. X-axis is the difference between the revolution time of the reference particle and all the others. A single line shows a phase-space trajectory of a particle with some value of $\frac{\Delta p}{p} \neq 0$. The voltage U_0 was set to be equal to 200 kV, RF frequency was 50 MHz. The separatrix size, in this case, is around $5 \cdot 10^{-3}$ with respect to $\frac{\Delta p}{p}$. This means that all the particles with the momentum deviation larger than $5 \cdot 10^{-3}$ are lost from the bunch, which is illustrated in the picture by the lines on both sides of the separatrix. Those particles don't oscillate around the equilibrium energy level. With the described parameters of the RF cavity a particle experience one synchrotron oscillation per 21 turn. That is shown in Figure 36.

Each line segment represents one turn, so the circle closes after 21 turns. This number is high enough to average out $\frac{\Delta \gamma}{\gamma}$ effects of the first order. One should examine how the decoherence is affected by an RF cavity.

The simulation was made where the initial particles have different energy or momentum offsets $\frac{\Delta p}{p}$ in the range $[-4 \cdot 10^{-3} \div 4 \cdot 10^{-3}]$. The

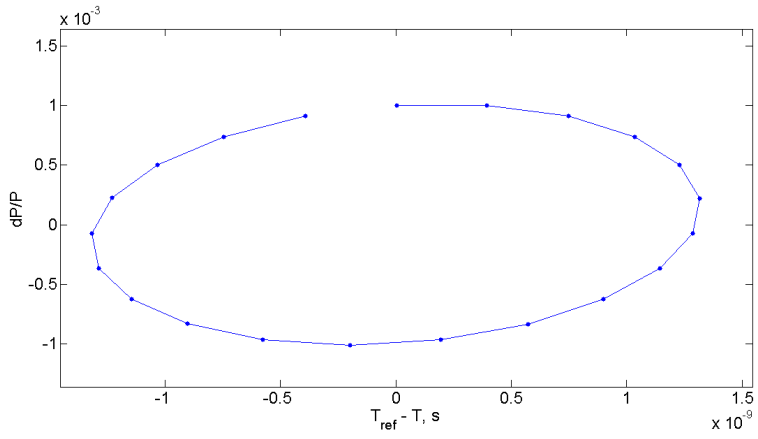

Figure 36: Number of turns needed for one complete synchrotron oscillation.

particles' initial spin was pointing in the direction of motion, $\vec{S} = (0,0,1)$. Then the S_x component of the spin vector of each particle was plotted after 100 and 10^4 turns. This is pictured in Figure 40. For better understanding of Figure 40, one has a look at Figure 37 and Figure 38.

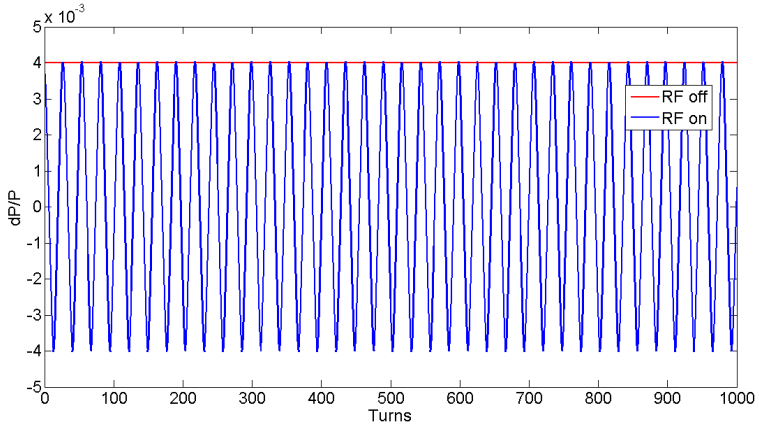

Figure 37: $\frac{\Delta p}{p}$ for a particle with initial momentum offset of $4 \cdot 10^{-3}$ when the RF cavity was turned on and off.

Figure 37 demonstrates the evolution of the non-reference particle's energy in time. Obviously, when the RF is turned off, the energy stays the same and it oscillates, when the RF is on. So what is going on with the spin in those two cases?

The horizontal spin component arose due to the energy deviation between the reference particle and the tracked particle, and thus due to the difference between the angles of spin rotation. In other words, the quasi-frozen spin condition 6.1.1 was broken. The spin began to rotate in the horizontal plane, meaning that the S_x started to oscillate from 1 to -1. All that happened, when the RF cavity was turned off. Opposite to that case, one sees the blue curve in this figure, which demonstrates

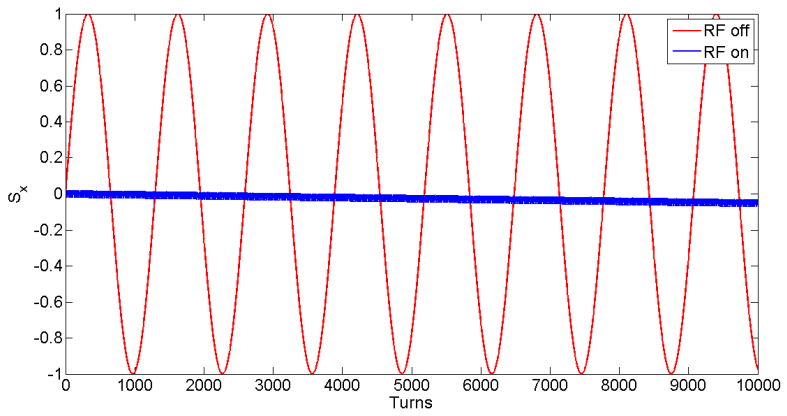

Figure 38: Oscillation of the S_x component of the particle with the initial $\frac{\Delta p}{p} = 4 \cdot 10^{-3}$ with respect to the turn number.

the behavior of the horizontal spin projection in time with the RF on. As it was predicted above, the RF cavity averages out the energy difference between the particles, and therefore the difference in their spin tunes. If one zooms into the picture, the oscillating pattern of the S_x component will be revealed (Figure 39).

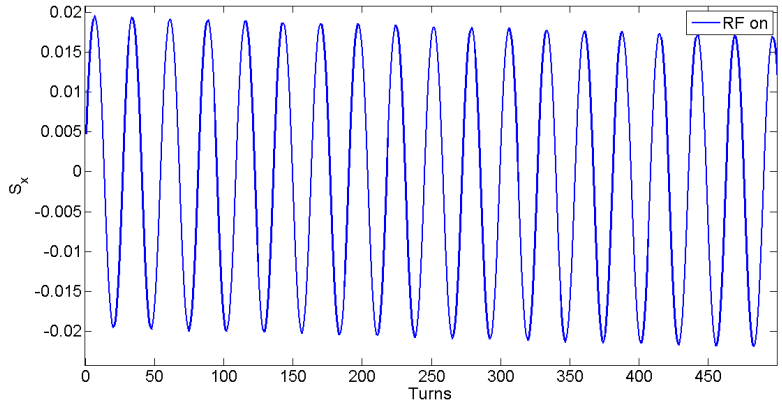

Figure 39: Oscillation of the S_x component of the particle with the initial $\frac{\Delta p}{p} = 4 \cdot 10^{-3}$ with respect to the turn number (zoom).

The small oscillation of the S_x is present, since there is the energy oscillation due to the RF field of the cavity. Nevertheless, one observes a slight slope in Figure 38 for the case with the switched on RF cavity. The slope is there because of the higher orders in the equation 6.1.4, which cannot be fought with only the RF cavity.

After the consideration of the single particle situation, Figure 40 should be inspected again. It has been shown that S_x of a non-reference particle oscillates from 1 to -1 in time. If RF is off, depending on the initial momentum deviation from the reference particle, the horizontal components of the spin vectors of all particles in the bunch will oscillate with different

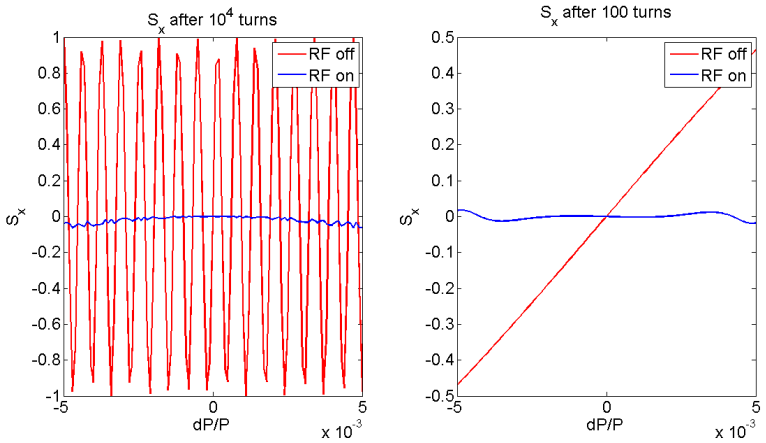

Figure 40: Left: horizontal spin component S_x for particles with different initial momentum offsets after 10^4 turns for RF on/off cases. Right: horizontal spin component S_x for particles with different initial momentum offsets after 100 turns for RF on/off cases.

frequencies (Figure 41). For example, if one tracks two particles, as it

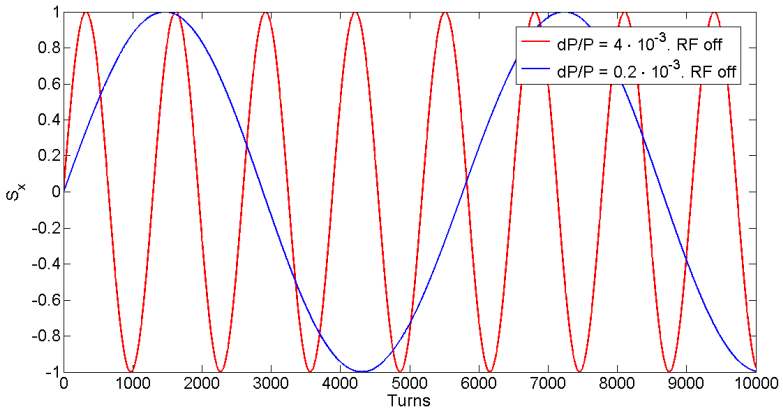

Figure 41: Oscillations of the S_x component for two particles with initial momentum offsets of $4 \cdot 10^{-3}$(red) and $0.2 \cdot 10^{-3}$(blue).

was done in Figure 41, the x projections of the spin vectors after, say, 10^4 turns will be different. This is the reason why the S_x components in the left part of Figure 40 have this random oscillating form. One obtains a broad variation of horizontal spin components for a bunch of particles after some number of turns if an RF cavity is switched off. This is the signal of complete depolarization. The right part of the picture 40 gives a more clear hint on the problem. Simply saying, one can notice that the spins of the particles with larger energy (or momentum) rotate faster than the spin of the reference particle. So their S_x components start to grow with time and after 100 turns they form almost a straight line with respect to their initial momentum deviation. Similarly, the spins of the

"slower" particles cannot perform the full rotation per one ring revolution, and therefore their S_x components become smaller than zero, which is the desirable value that corresponds to the S_x of the reference particle.

Alternatively to this case, the blue lines illustrate the behavior of S_x when the RF cavity was turned on. The RF smears out the energy difference, thus the spin tune difference, and all the particles in the bunch have roughly the same S_x component after 10^4 turns. However, the blue curve has a parabolic shape.

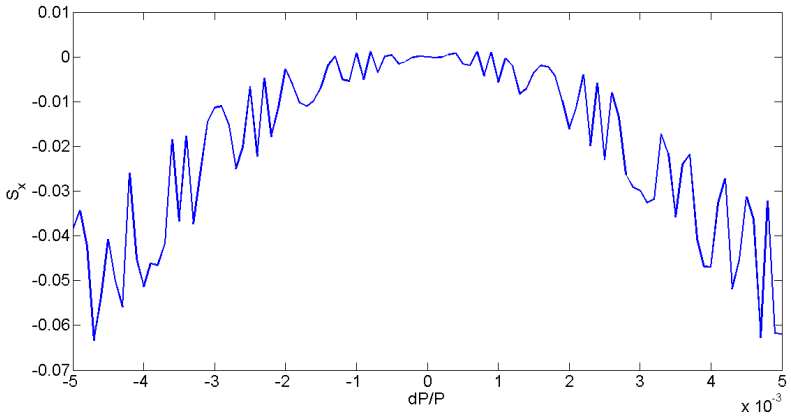

Figure 42: S_x spin components of the particles in the bunch with initial $\frac{\Delta p}{p}$ offsets after 10^4 turns with the RF cavity turned on.

This plot looks like a parabola because the energy change is quadratically proportional to the initial $\frac{\Delta p}{p}$, according to the equation 3.2.17. RF field cannot fully compensate this effect, and one needs to use sextupole correction.

One can define the condition for the depolarization occurrence in the following way:

$$S_x^{ref} - S_x^{max\,\frac{\Delta p}{p}} \leq 1, \tag{6.1.10}$$

where S_x^{ref} is the horizontal spin projection of the reference particle and $S_x^{max\frac{\Delta p}{p}}$ is the horizontal spin projection of the particle with the largest $\frac{\Delta p}{p}$. In the Figure 42 this difference is around $5 \cdot 10^{-2}$ at 10^4-th turn. This difference grows linearly and at 10^9-th turn (this number of turns, as was mentioned above, is needed to measure an EDM signal) will surely exceed 1. So one needs to use, firstly, sextupole correction to decrease the slope of the parabola and, secondly, beam cooling to reduce the $\frac{\Delta p}{p}$ maximum value down to $\frac{\Delta p}{p} \approx 10^{-5}$. The sextupole correction of the spin coherence time will be discussed in the next subsection.

Orbit lengthening, and therefore the energy deviation, depends on the momentum spread (3.2.16) in the areas with non-zero values of a dispersion function. Use of a RF cavity can also slightly decrease the decoherence effect in the horizontal plane. Having a look at Figure 43 one concludes that the improvement of the decoherence in the x-plane by the

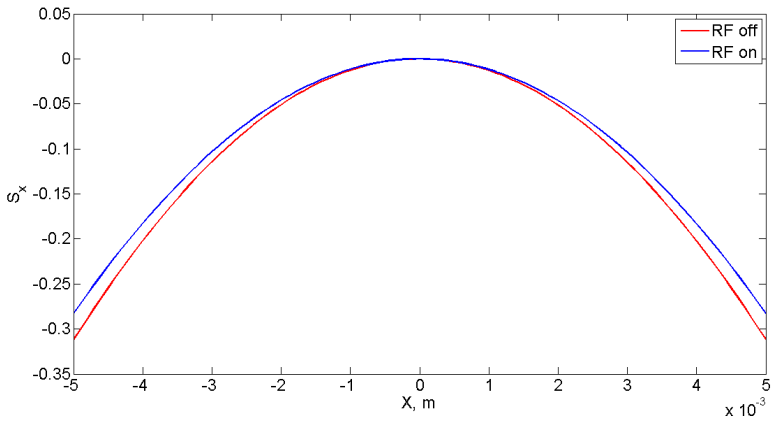

Figure 43: S_x spin components of the particles in the bunch with initial x offsets after 10^4 turns with the RF cavity turned on and off.

RF cavity is almost negligible, thus the sextupole correction plays the major role in this case.

To summarize, implementation of a radio frequency cavity is a necessary condition for the upcoming EDM experiment. An RF averages out energy difference between the particles in the bunch, which, in turn, directly acts on their spin precession frequencies. For the quasi-frozen and the frozen spin methods an optimal value of an RF voltage is around 200 KV and the frequency should be 50 MHz. These parameters decrease the decoherence due to $\frac{\Delta p}{p}$ effects. With the appropriate beam cooling, reducing the longitudinal beam size down to $\sim 10^{-5}$, switched on RF cavity makes possible to reach the spin coherence time of around 1000 seconds.

Sextupole correction of spin coherence time

The spin tune spread, which leads to the decrease of the spin coherence time, was explained in chapter 3. The formula 3.2.18 was written for N number of turns

$$2\pi\langle\Delta\nu_s\rangle = 2\pi G\langle\Delta\gamma_{eq}\rangle N_t. \tag{6.1.11}$$

The equation above shows that the spin decoherence is described through the equilibrium energy (energy averaged over one turn) spread. This energy spread can be rewritten as a equilibrium momentum spread according to formula 3.2.10

$$\Delta\delta_{eq} = \frac{\gamma_s^2}{\gamma_s^2\alpha_0 - 1}\left[\frac{\delta_m^2}{2}\left(\alpha_1 - \frac{\alpha_0}{\gamma_s^2} + \frac{1}{\gamma_s^4}\right) + \left(\frac{\Delta L}{L}\right)_\beta\right], \tag{6.1.12}$$

where the terms included in the equation reflects the nature of the energy deviation, which is present due to the orbit lengthening and the momentum spread in a bunch of particles. The contribution from the first term in formula 6.1.12 is easy to deal with, unlike the second term. One has to

use a sextupole family that, however, introduces a change of momentum compaction factor [88]

$$\Delta\alpha_{1,sext} = -\frac{S_{sext}D_0^3}{L}, \tag{6.1.13}$$

where $S_{sext} = \frac{1}{2B\rho}\frac{\partial^2 B_y}{\partial x^2}$ is the sextupole strength and D_0 is the coefficient in equation 3.2.13 for angular dispersion. It's possible to correct the second order momentum compaction factor up to the desired value, using the equation below

$$\alpha_1 + \Delta\alpha_{1,sext} = \frac{\alpha_0}{\gamma_s^2} - \frac{1}{\gamma_s^4}. \tag{6.1.14}$$

So, one has to cope with the second term of 6.1.12. Equation 3.2.12

$$\left(\frac{\Delta L}{L}\right)_\beta = \frac{\pi}{2L}\left[\epsilon_x\nu_x + \epsilon_y\nu_y\right] \tag{6.1.15}$$

demonstrates the orbit lengthening in the abscence of multipoles corresponding to the linear betatron oscillations.

See Appendix A for full derivation of the sextupole compensation. Only the final result presented will be presented here.

One can write the conditions for the orbit lengthening compensation by sextupoles [88].

$$\begin{aligned} -\frac{\epsilon_x}{2L}\sum_i S_i l_{si} D_{xi}\beta_{xi} &= \frac{\pi}{2L}\epsilon_x\nu_x \\ \frac{\epsilon_y}{2L}\sum_i S_i l_{si} D_{xi}\beta_{yi} &= \frac{\pi}{2L}\epsilon_y\nu_y \\ -\frac{\delta^2}{L}\sum_i S_i l_{si} D_{xi}^3 &= \alpha_1\delta^2. \end{aligned} \tag{6.1.16}$$

To summarize, the equilibrium energy shift caused by the orbit lengthening and the momentum spread in a bunch can be compensated if the contribution from momentum compaction factor of the second order α_1 is suppressed and the orbit lengthening is corrected with sextupoles. For this correction, one has to use three sextupole families placed in the sections of maximum/minimum values of $\beta_{x,y}$ functions and the dispersion function D_0.

Simulations for the improvement of spin coherence time with sextupole correction

In this subsection the simulations that was made for the correction of the spin coherence time with sextupoles will be discussed. Two lattices - for the frozen and the quasi-frozen spin methods - are very similar, though they have their distinctions.

Sextupoles	SFP	SDP1	SDP2	SFN	SDN1	SDN2
Field gradient, $\mathrm{T/m^2}$	-45.57	46.5	21.7	28.54	$-3,41$	-0.85

Table 2: Sextupole settings for the quasi-frozen spin lattice.

Firstly, the quasi-frozen spin lattice will be considered. Six sextupole families were set in the ring. The sextupoles were placed in the places with maximum and minimum values of beta-functions $\beta_{x,y}$ and dispersion function D. The number of families is larger than three, since the lattice has a peculiar design with negative dispersion sections. Figure 44 demonstrates the location of each sextupole from a different family, although not all the sextupoles are pictured. The total number of the sextupoles was equal to 26. The sextupole settings that were used for the correction of the SCT are shown in Table 2. The sextupoles were focusing and defocusing, which were placed in the positive or negative dispersion sections. For example, SFP means that the sextupole is focusing and is located in the positive dispersion region - **S**extupole, **F**ocusing, **P**ositive. These values of field gradients were the optimal ones for the longest spin coherence time.

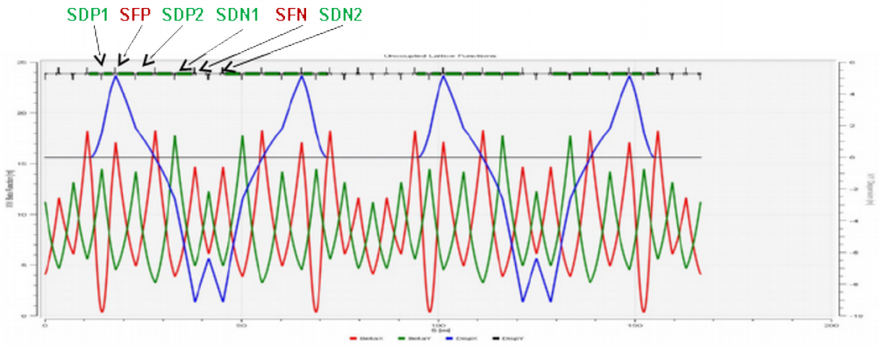

Figure 44: Beta- and dispersion functions for the lattice of the quasi-frozen spin method with the location of the sextupoles from six different families.

Figure 45 illustrates the S_x component that is interesting for us without any sextupole correction after 10^4 revolutions in the ring. The parabola in y-plane has smaller slope because there is no dispersion in the vertical plane. Then the sextupoles were turned on and the optimal values were found for both planes. Figure 46 pictures the S_x components of the particles in the bunch after 10^4 turns. Three curves are for various settings of the sextupole fields. The difference between the reference particle's horizontal spin projection and the particle with the initial x offset of $5\,\mathrm{mm}$ is of the order of $5 \cdot 10^{-4}$ for various sextupole settings. If one calculates the SCT from this results, it will be equal to $\sim$ 150 seconds, assuming that the S_x component grows linearly with time. One observes clearly non-parabolic dependence, which is predicted by the formula 3.2.17. This

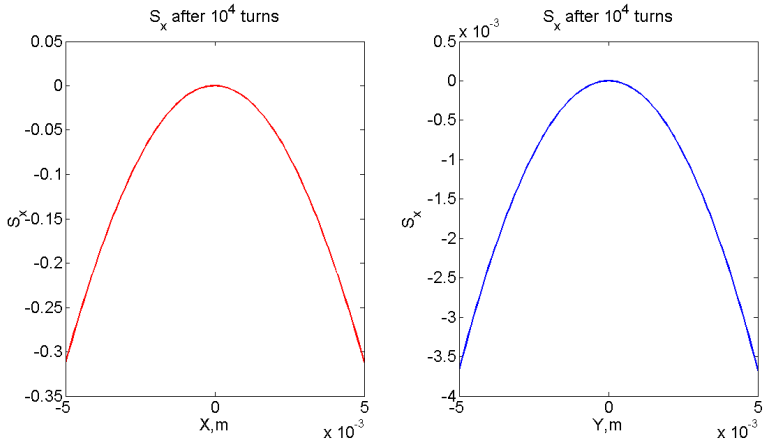

Figure 45: S_x spin components of the particles in the bunch with initial x and y offsets after 10^4 turns without sextupole correction.

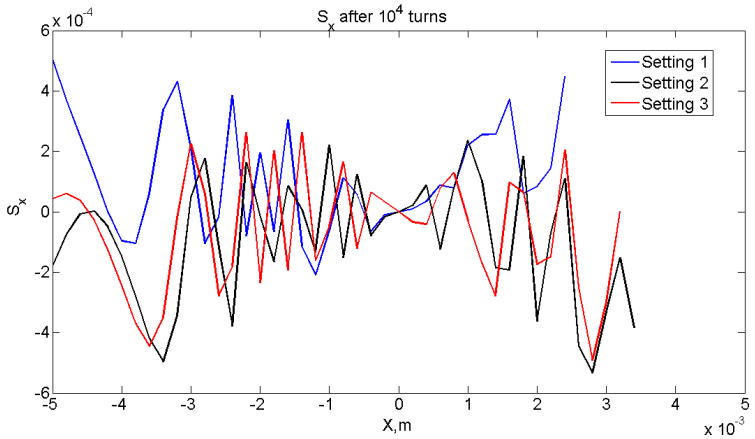

Figure 46: S_x spin components of the particles in the bunch with initial x offsets after 10^4 turns with three various sextupole settings.

feature will be discussed in the next subsection and it's correlated with the form of the electric potential between the electrodes.

The assumption that the beam is cooled down and its horizontal size is shrinked down to 1 mm has been made. One can zoom into Figure 46 and Figure 47 will be obtained. The SCT in this case is of the order of

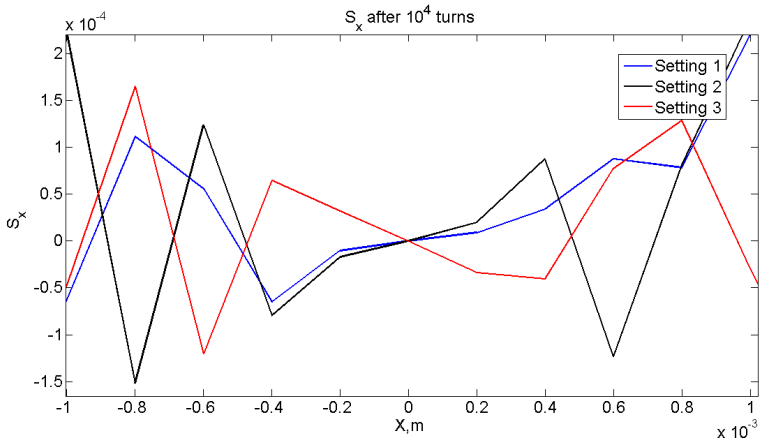

Figure 47: S_x spin components of the particles in the bunch with initial x offsets after 10^4 turns with three various sextupole settings.

1500 seconds, which is enough to measure an EDM.

Now, one can investigate the motion of the spin, when one has an offset in the vertical plane. Figures 48 and 49 shows the horizontal spin components of a bunch of particles, which has a vertical size of 5 mm.

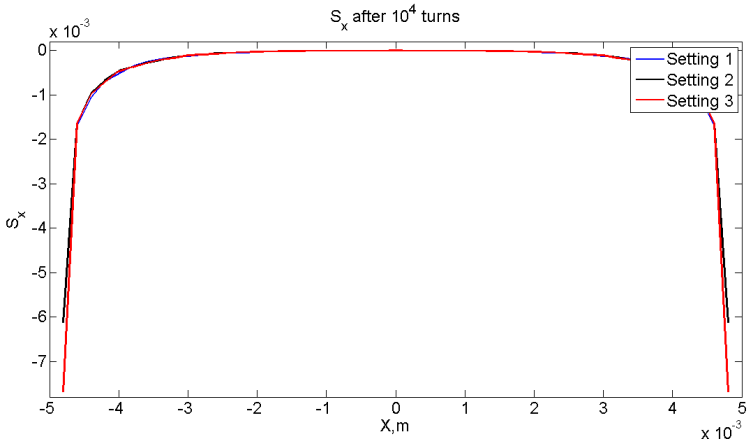

Figure 48: S_x spin components of the particles in the bunch with initial y offsets after 10^4 turns with three various sextupole settings.

The SCT for the y plane and for the beam size of 1 mm is around 15000 seconds. In this plane the parabolic dependence on the coordinate y is present.

The dependence of the S_x component on $\frac{\Delta p}{p}$ was discussed earlier. For both concepts, the frozen and the quasi-frozen, it is the same. The change of S_x is modulated by the RF and from turn to turn the curve is slightly

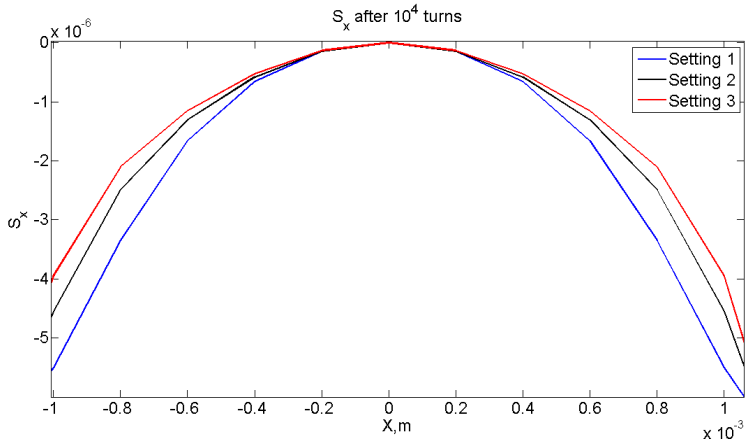

Figure 49: S_x spin components of the particles in the bunch with initial y offsets after 10^4 turns with three various sextupole settings.

different, which is plotted in Figure 50. One needs to cool the beam down

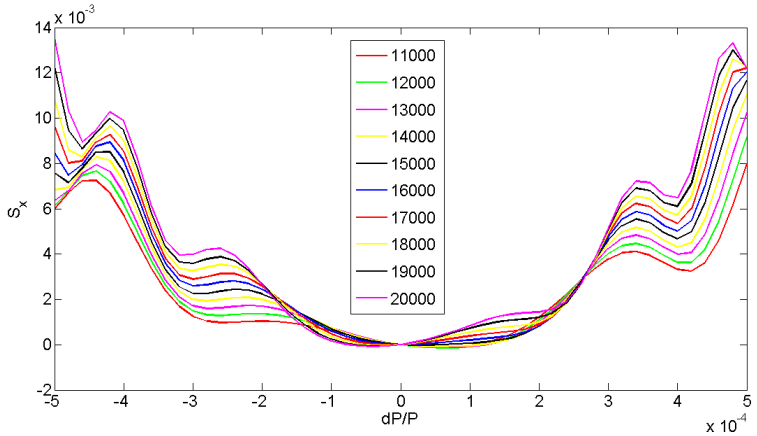

Figure 50: S_x spin components of the particles in the bunch with initial $\frac{\Delta p}{p}$ offsets after various number of turns in the range between ten and twenty thousand.

to 10^{-5} approximately to get the SCT of the order of 1000 seconds. The curves have parabolic feature, which are modulated by the RF voltage. That is why, one sees some "wiggles" on the graph.

The same calculations for the frozen spin method are presented below. This approach requires only two sextupole families, the energy deviation is corrected by an RF cavity and beam cooling. The table with the field gradients for both families is given below (Table 3).

The similar simulations were performed and the results for y and x planes are shown in the following figures (Figure 52 and Figure 54). The sextupoles were tuned in a way that for 1 mm radial or vertical beam sizes the SCT was of the order of 1000 seconds.The longitudinal plane looks exactly like in the quasi-frozen spin approach. And as for the quasi-frozen spin method, zooming into Figure 52 one sees the horizontal spin

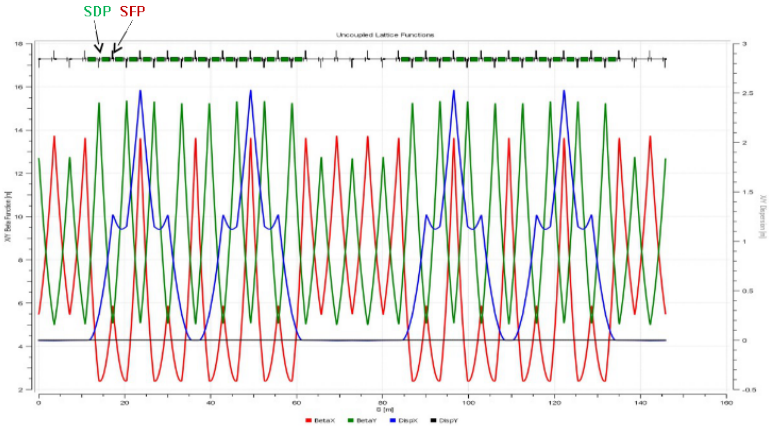

Figure 51: Beta- and dispersion functions for the lattice of the frozen spin method with the location of the sextupoles from two different families.

Sextupoles	SDP	SFP
Field gradients, $\mathrm{T/m^2}$	23.50	−39.25

Table 3: Sextupole settings for the frozen spin lattice.

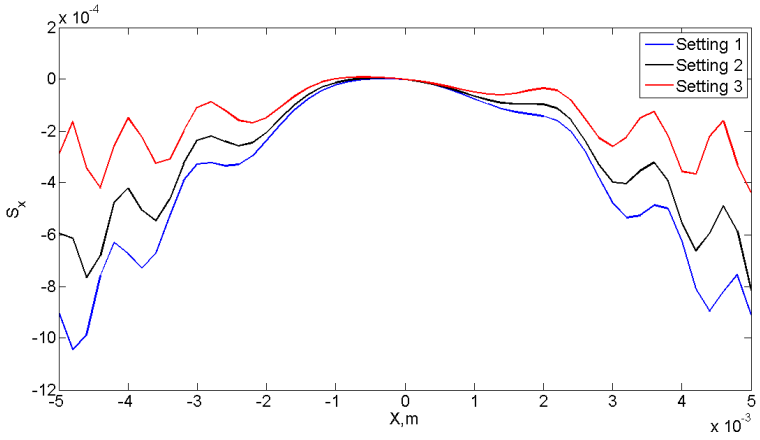

Figure 52: S_x spin components of the particles in the bunch with initial x offsets after 10^4 turns with three various sextupole settings.

dependence for the bunch of 1 mm horizontal size. The same is for the y

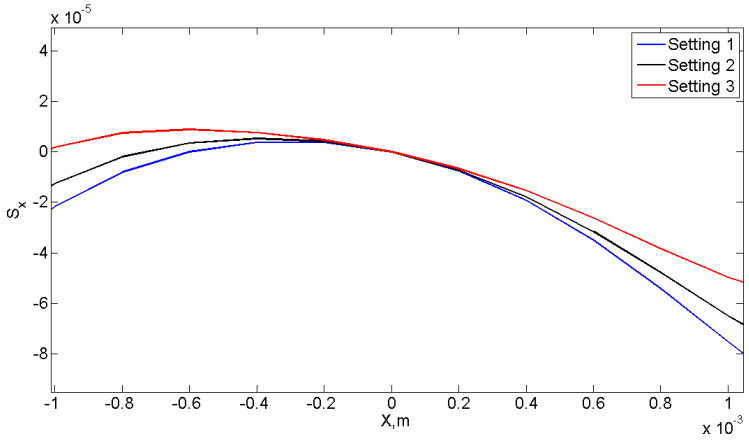

Figure 53: S_x spin components of the particles in the bunch with initial x offsets after 10^4 turns with three various sextupole settings.

plane:

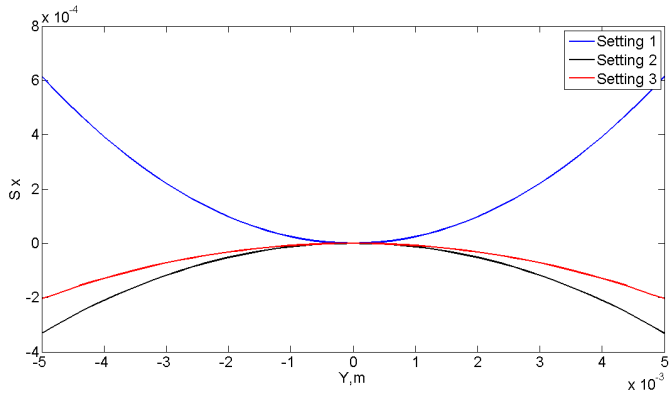

Figure 54: S_x spin components of the particles in the bunch with initial y offsets after 10^4 turns with three various sextupole settings.

Concluding, these two methods for an EDM measurement look very similar and the results, which were obtained for the prolongation of the spin coherence time, are close to each other. If one assumes that the difference between the horizontal spin components of the reference particle and a particle on the edge of the bunch grows linearly in time, then these two approaches are almost identical. For both of them the SCT value is enough and exceeds 1000 seconds for the beam size of 1 mm and $\frac{\Delta p}{p} \approx 10^{-5}$.

Stabilization of the average horizontal spin component in the quasi-frozen spin method

In the previous subsection the assumption that the difference between the horizontal spin components of the reference particle and a particle

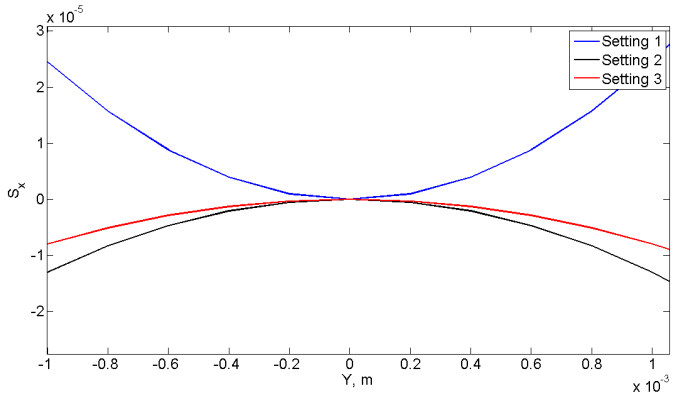

Figure 55: S_x spin components of the particles in the bunch with initial y offsets after 10^4 turns with three various sextupole settings.

on the edge of the bunch grows linearly was made. When one starts to investigate this further, it turns out to be that this assumption is not completely true.

One can define root mean square value of the S_x components for a bunch of particles.

$$\sigma_{S_x} = \sqrt{\frac{1}{N}\sum_{i=1}^{N}(S_x^i - \langle S_x \rangle)^2}, \tag{6.1.17}$$

where N is the number of particles in the bunch. The simulation was made with 101 particle with initial radial offsets in the range of $[-1, 1]$ mm. The sextupoles were turned on and set to the optimal value, which corresponds to the longest spin coherence time. The particles were tracked for 100000 turns and the σ_{S_x} of the S_x was calculated after each hundred of turns. Figure 56 illustrates the dependence of the root mean square of the horizontal component of the spins for all particles in a bunch.

One sees that the RMS value doesn't grow linearly as the number of turns increases. It stabilizes after some number of turns and stays almost constant. In fact, the behavior of that the RMS value is not simple and is very sensitive to sextupoles settings or changes in the RF voltage, for instance. The beam size also plays a crucial role in the process of the stabilization. Figure 57 shows the RMS S_x for the quasi-frozen approach when the sextupoles were completely turned off.

Another graph was obtained with COSY-infinity program by Eremey Valetov for comparison and benchmarking the results of MODE simulations [86]. His simulation results are shown in Figure 58. He used different values of sextupoles and different RF voltages. The particles were tracked for 400000 revolutions, so $N = 20$ in the picture corresponds to 400000-th turn.

From the results obtained in two programs, one can prove that the RMS value depends on the RF voltage and sextupole settings. However, emittance or size of the beam strongly affect stabilization, as well. The

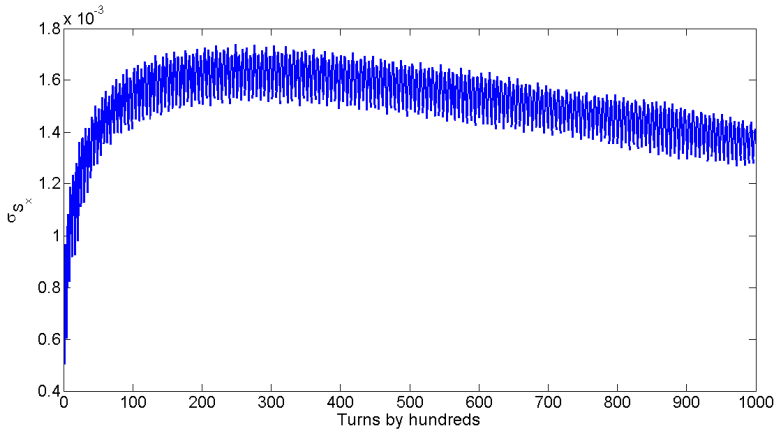

Figure 56: σ_{S_x} of S_x components for the particles with initial x offsets in the range of $[-5;5]$ mm. Sextupole values corresponded to the longest spin coherence time.

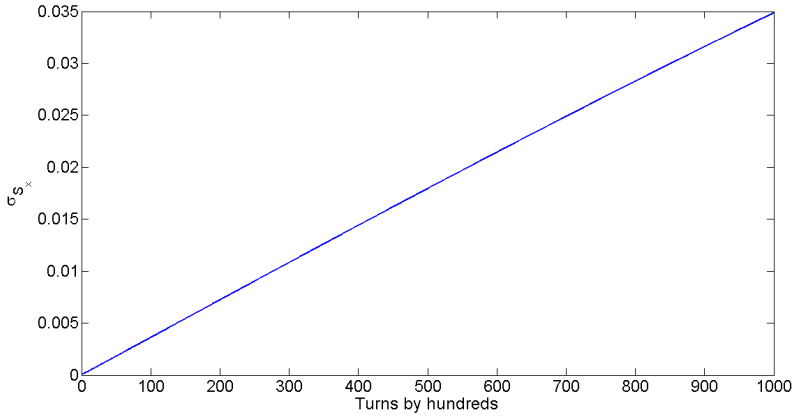

Figure 57: Root mean square of S_x components for the particles with initial x offsets in the range of $[-5;5]$ mm. Sextupoles were turned off.

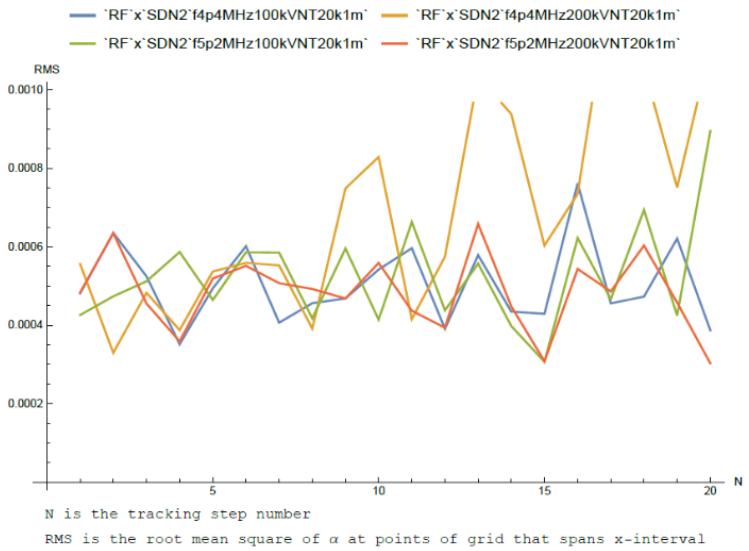

Figure 58: Root mean square of S_x components for the particles with initial x offsets in the range of $[-5;5]$ mm. Sextupole field gradients and RF voltage were varied. Simulation was performed in COSY-infinity program [86].

emittance restrictions were considered in the chapter 3. The limit for the emittance for COSY ring was set to $\epsilon_{x,y}^{rms} < 1.4\text{mm mrad}$ (3.2.22). The smaller the emittance, the better the stabilization of the root mean square value. Figure 59 was obtained for the frozen spin method for different radial beam sizes. For this case the sextupoles were turned off. One clearly sees that as soon as the beam size is getting smaller, the stabilization becomes better. So, again, the cooling is essential in the performance of the future EDM experiment.

Nevertheless, the RMS is growing. Indeed, the increase is slower than predicted linear growth but it is present in the plot. One can define the function f, which can be written as

$$f = (S_x - S_{x,ref})_{RMS} = a + b \cdot N, \tag{6.1.18}$$

where a is the difference between the S_x components of the reference and any other particle in a bunch, b is the slope of the RMS value of the S_x for the bunch, N is the number of turns. So, here the strong assumption that the RMS will be rising linearly is made. The MODE and COSY-infinity simulations were made and the optimal parameters b were found to have the spin coherence time longer than 1000 seconds. To achieve the SCT of that long the function f must be of the order of 10^{-9}. Below are the pictures of two tables with the calculated a and b values for different RF voltages and RF frequencies. The sextupoles were also tuned to get the maximum SCT value. All three initial spreads were considered: $\frac{\Delta p}{p}$, x and y. The absolute value for all three offsets was set

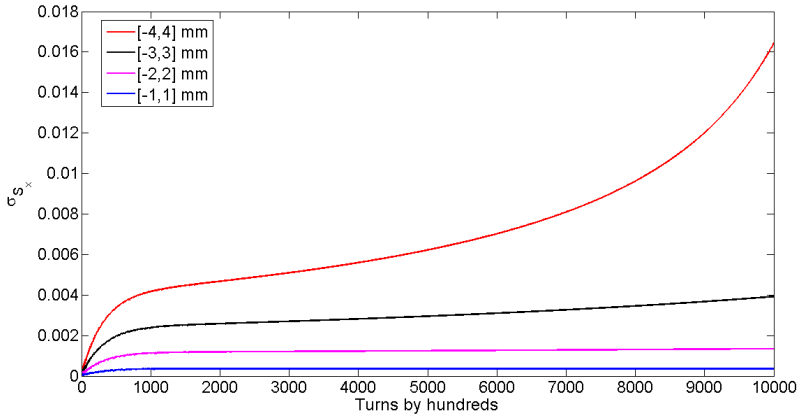

Figure 59: Root mean square of S_x components for the particles with different initial x ranges. Sextupoles were turned off.

to be equal to $5 \cdot 10^{-3}$ (in meters, in case of radial and vertical offsets, and in relative units for energy spread). The program was calibrating the

Structure type	$(S_x)_{RMS}$ = a + b·N at energy spread ΔW/W = 5·10^{-3}	$(S_x)_{RMS}$ = a + b·N at horizontal spread x = ± 5·10^{-3}	$(S_x)_{RMS}$ = a + b·N at vertical spread Y = ± 5·10^{-3}
Frozen Spin	RF = 100 kV at 5 MHz; SFP vary; a = 0.05, b = 2.9·10^{-7}	RF = 100,200 kV at 5 MHz; SFP vary; a = 0.00035, b = 0.1·10^{-9}	RF = 100 kV at 5 MHz; SFP vary; a = 1·10^{-5}, b = 0.3·10^{-7}
	RF = 200 kV at 5 MHz; SFP vary; a = 0.03, b = 0.1·10^{-7}		RF = 200 kV at 5 MHz; SFP vary; a = 1·10^{-5}, b = 0.2·10^{-9}
	RF = 200 kV at 5 MHz; SDP vary; a = 0.03, b = 0.1·10-7	RF = 100,200 kV at 5 MHz; SDP vary; a = 0.0003, b = 0.3·10^{-9}	RF = 200 kV at 5 MHz; SDP vary; a = 1·10^{-5}, b = 0.3·10^{-9}
	RF = 100 kV at 5 MHz; SDP vary; a = 0.04, b = 2.7·10^{-7}		RF = 100 kV at 5 MHz; SDP vary; a = 1·10^{-5}, b = 0.2·10^{-9}

Figure 60: Parameters of function f for different voltages and frequencies of the RF cavity for the frozen spin lattice. Sextupoles were automatically tuned to find the best spin coherence time.

sextupole values automatically, using gradient descent method [66]. This results from COSY-infinity simulations made by E.Valetov confirmed that high values of the SCT can be achieved even for relatively large beam sizes. Confirming one more time the statement above, the spread in $\frac{\Delta p}{p}$ should be smaller than $5 \cdot 10^{-3}$ yet, since, as one reads from Figure 60 (other tables are presented in Appendix C), the parameter b is of the order of $10^{-7} \div 10^{-8}$, which is not enough.

Finally, the two methods for an EDM search regarding the spin coherence time studies look promising. For both cases, the long spin coherence time can be obtained. A radio frequency cavity and sextupoles give the opportunity to fight the decoherence effects, which are present in any machine for finite sizes of a beam.

One should return back to the plots of S_x spin components, when the initial particles' coordinates were distributed along the horizontal axis. The sextupoles were turned on and tuned to the values, corresponding to the longest spin coherence time for the quasi-frozen and the frozen spin approaches (see Figures 46 and 52). One sees that the parabolic nature of the curves are lost. The graphs look like zigzags or wavy parabolas. That imposes some limitations on the spin coherence time. In the vertical plane everything is smooth (Figures 48, 54). The presence of the oscillating RF field, which modulates the spin motion, is responsible for the presence of those zigzags. However, is this is the only reason?

The answer to this question is uncertain. So one has to find out, whether the RF modulation is the only source of the non-parabolic behavior of the horizontal spin component. As a matter of fact, the electric field is needed in both methods. The obvious step would be the investigation of the aspects connected with the presence of the electric field. The specific features of this field are important and they affect the spin motion, by adding non-linearities in it. The next two subsections will shed light on that issue.

Kinetic energy change in the electric field potential

Electric cylindrical deflectors are used in both methods for beam steering. The particle dynamics in an electric field differs from one in a magnetic field. One should consider the effects, which take place when a particle flies through a cylindrical deflector.

A particle moves in a magnetic field with the constant absolute value of its velocity, which can be seen directly from Newton-Lorentz equation: the force acting on a particle is always perpendicular to the velocity vector. In an electrostatic field, a particle travels with acceleration according to the total energy conservation law. The total particle's energy must be the same before entering and after leaving a region with an electric field [69], [70]. Figure 61 shows that particular situation.

There were previously defined equations of a spin-orbital dynamics in chapter 2. They describe a particle motion according with the energy conservation law, 2.3.14

$$W' = -qu'(x,y,s) = q(E_x x' + E_y y' + E_s), \tag{6.1.19}$$

where W is the kinetic particle energy, q is the elementary charge and $E_{x,y,s}$ are the electric field components.

One should look at the situation, when a particle enters an electric field from a region with zero electric potential $u(x,y,z) \equiv 0$ an leaves the field also to the region with no electric potential. The particle velocity in this case must be the same before and after the area with the electric field, with accordance to 2.3.14. One should examine the time moment, when the particle flies in the electric field with the potential $u(x,y,z)$ (see Figure 61). As soon as the particle is caught in the electric field, it

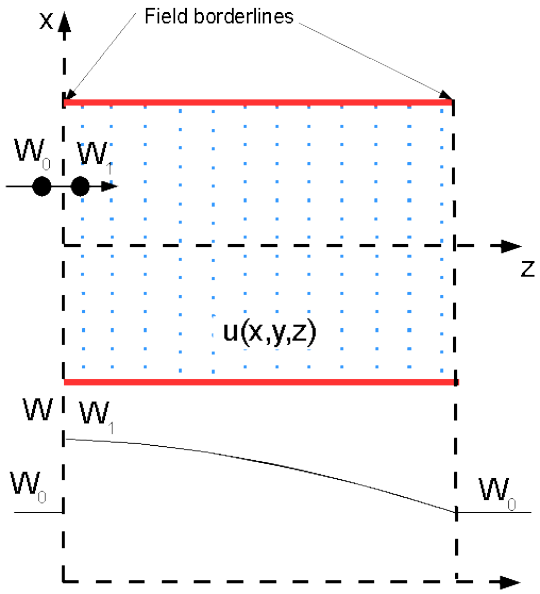

Figure 61: Change of kinetic energy of a particle moving through an electric deflector.

should accelerate (decelerate) accordingly to the gained (lost) potential energy

$$W_1 = W_0 - qu(x,y,z). \tag{6.1.20}$$

This instantaneous jump in particle's kinetic energy corresponds to the perpendicular fringe field. In reality, a particle moves through all the potential lines from $u_0 = 0$ to $u(x,y,z)$, smoothly changing its potential energy.

This fringe field affects the kinetic energy of the particle. One can do Taylor expansion of the potential $u(x,y,0) = u_0 + u_1 x + u_2 y + u_{11}x^2 + u_{12}xy + \ldots$ and write the following matrix equation

$$\begin{pmatrix} x \\ y \\ t \\ p_x \\ p_y \\ W \end{pmatrix} = \begin{pmatrix} 0 \\ 0 \\ 0 \\ 0 \\ 0 \\ qu_0 \end{pmatrix} + \begin{pmatrix} 1 & 0 & 0 & 0 & 0 & 0 \\ 0 & 1 & 0 & 0 & 0 & 0 \\ 0 & 0 & 1 & 0 & 0 & 0 \\ 0 & 0 & 0 & 1 & 0 & 0 \\ 0 & 0 & 0 & 0 & 1 & 0 \\ u_1 & u_2 & 0 & 0 & 0 & 1 \end{pmatrix} \begin{pmatrix} x_0 \\ y_0 \\ t_0 \\ p_{x,0} \\ p_{y,0} \\ W_0 \end{pmatrix} + \ldots \tag{6.1.21}$$

MODE takes into account those energy kicks at the entrance and at the end of an electric element. The detailed study was performed to check the influence of the energy kicks on the spin behavior. The simulation tool has an option of turning on and off described energy kicks, although turning them off corresponds to an unphysical situation. The simulations were made without the kicks to investigate their impact on the spin motion. All tracking results in this subsection were calculated for the frozen spin

method, since they are equivalent to the quasi-frozen approach. One can examine one of the results pictured in Figure 62. The sextupoles were set to the same values as for the black curve in Figure 52.

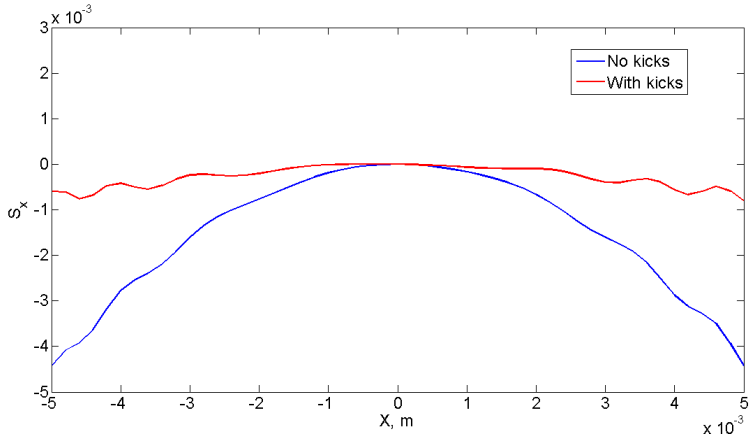

Figure 62: Blue: S_x spin components of the particles in the bunch with initial x offsets after 10^4 turns without energy kicks. Red: S_x spin components of the particles in the bunch with initial x offsets after 10^4 turns with energy kicks.

The parabola for the no-kicks case became steeper, as a result, the spin coherence time went down. This happened due to the violation of the full energy conservation law. The sextupole settings that have been optimal before, became wrong because the energy of the reference particle is not conserved from revolution to revolution. The sextupole compensation is not longer correct with the previous values of the field gradients. This is the reason for decreasing of the SCT.

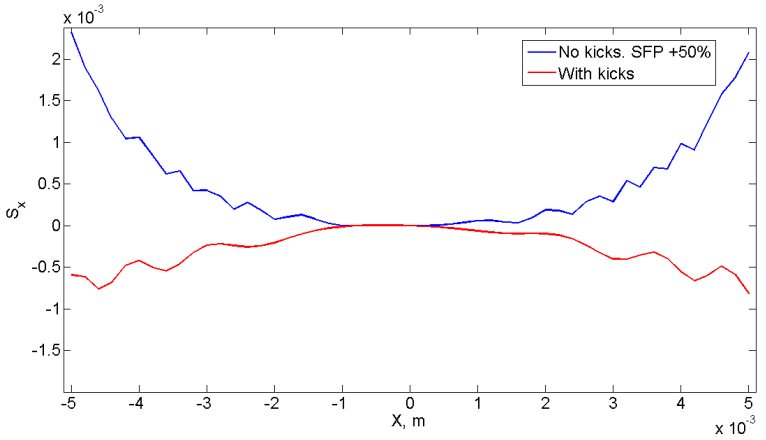

Figure 63: Blue: S_x spin components of the particles in the bunch with initial x offsets after 10^4 turns without energy kicks with ramped up SFP (see Table 3) sextupoles by 50%. Red: S_x spin components of the particles in the bunch with initial x offsets after 10^4 turns with energy kicks.

Nevertheless, the wiggles on the graph remained unchanged. This is not obvious from the plot in Figure 62, since the parabola is too steep to see that. That is why the sextupoles were adjusted to bring the parabola closer to zero (Figure 63). Regarding the y plane, turning off the energy kicks in the program affected the S_x component in the similar manner. A parabola has changed its steepness. This can be seen in Figure 64.

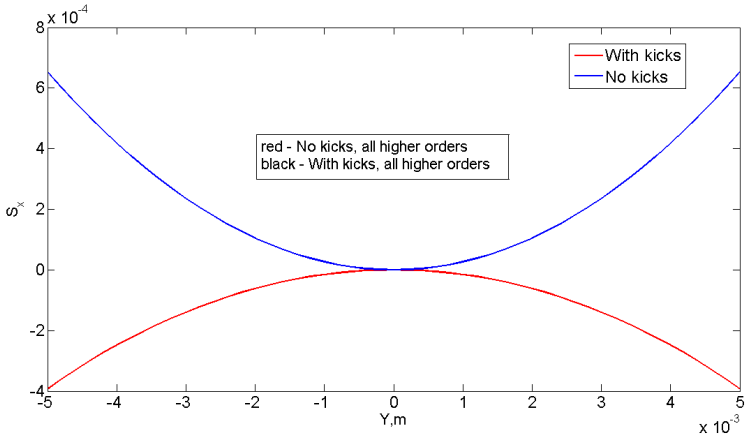

Figure 64: Blue: S_x spin components of the particles in the bunch with initial y offsets after 10^4 turns without energy kicks. Red: S_x spin components of the particles in the bunch with initial y offsets after 10^4 turns with energy kicks.

This means that energy kicks at both sides of the electric deflector do not contribute to the additional non-linearities of the spin motion or their contribution is negligibly small. One should further investigate the nature of electric field to find out the reason for non-parabolic shapes of the plots for S_x. The closer look at the form of the electric potential was taken. It will be discussed next.

The features of spin-orbital dynamics in the cylindrical deflector

As was shown in the previous subsection, the energy kicks at the ends of an electric deflector have negligibly a small contribution. However, the form of the electric potential itself sets significant limits on the spin coherence time. Let us investigate a cylindrical deflector, which is pictured in Figure 65

In accordance with Gauss's law [53] an electric potential between the internal electrode with the radius R_1 and the external electrode with the radius R_2 can be written as

$$\phi(r) = -U_0 + \frac{2U_0}{\ln\frac{R_2}{R_1}} \cdot \ln\frac{r}{R_1} \tag{6.1.22}$$

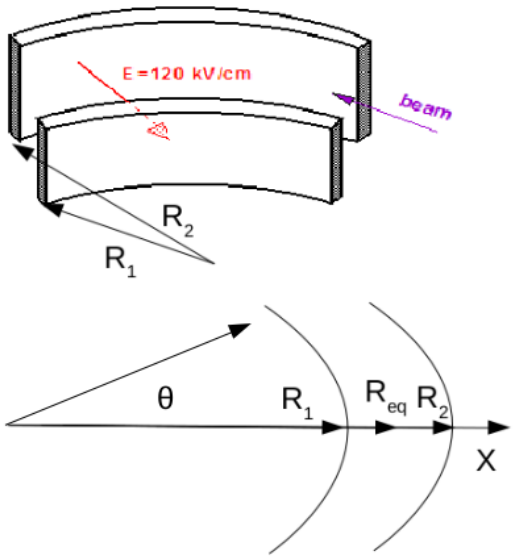

Figure 65: A cylindrical deflector in 3D and in horizontal plane.

where U_0 is the voltage at the electrodes, R_{eq} is the equilibrium radius of the reference particle trajectory inside the deflector. In the area between the electrodes the electric field has the form

$$E_R = \frac{2U_0}{\ln\frac{R_2}{R_1}} \cdot \frac{1}{r}. \tag{6.1.23}$$

One can write the equation of motion with the corresponding Lagrangian in such a field (see Appendix B) and get the following result [89]

$$r'' = \frac{1}{r} - \frac{em}{M^2} \cdot \frac{2U_0}{\ln\frac{R_2}{R_1}} r, \tag{6.1.24}$$

where $M = mv_\theta R_{eq}$ is the angular momentum, which is conserved, and $v_\theta = r\dot{\theta}$ is the angular velocity. For the ideal case, when the reference particle moves along the trajectory with the constant radius R_{eq}, it is clear that $r'' = 0$ and therefore

$$R_{eq}^2 = M^2 \cdot \frac{\ln\frac{R_2}{R_1}}{2emU_0}. \tag{6.1.25}$$

Now, the equation of motion has a simple form

$$r'' - \frac{1}{r} + \frac{1}{R_{eq}^2} r = 0. \tag{6.1.26}$$

One applies the transformation to the Cartesian coordinate system, where $E_x = E_R$, $E_y = 0$ and $r = R_{eq} + x$. Taking into account the fact

that $\frac{x}{R_{eq}} \to 0$ and substituting it in the 6.1.26, one gets the system of equations [91]

$$\begin{aligned} x'' + \frac{2}{R_{eq}^2}x - \frac{1}{R_{eq}^3}x^2 = 0 \\ y'' = 0. \end{aligned} \tag{6.1.27}$$

The orbital motion in the ideal case has no coupling between the horizontal and the vertical planes. It is clearly visible that the potential has the quadrupole and pseudosextupole components.

MODE allows a user to create an element with electric or magnetic fields of arbitrary configuration. The frozen spin lattice was chosen for a starting point with its $E + B$ elements (BNL elements). The electric field inside a BNL element was determined through the field potential and the strength. The shape of the electrodes of a BNL element is cylindrical.So the potential is given by the formula 6.1.22. Further Taylor expansion in the vicinity of zero was made for the potential up to the fifth order.

$$\begin{aligned} \phi(r) = -U_0 + \frac{2U_0}{\ln\frac{R_2}{R_1}} \cdot \ln\frac{R_{eq}+x}{R_1} = \\ = -U_0 + \frac{2U_0}{\ln\frac{R_2}{R_1}} \cdot \ln\left(\frac{R_{eq}}{R_1} + \frac{x}{R_1}\right) = \\ = -U_0 + \frac{2U_0}{\ln\frac{R_2}{R_1}} \cdot \left[\ln\left(\frac{R_{eq}}{R_1}\right) + \ln\left(1 + \frac{x}{R_{eq}}\right)\right] = \\ = -U_0 + \frac{2U_0}{\ln\frac{R_2}{R_1}} \cdot \left[\ln\left(\frac{R_{eq}}{R_1}\right) + \frac{x}{R_{eq}} - \frac{x^2}{2R_{eq}^2} + ... + \frac{x^5}{5R_{eq}^5}\right] \end{aligned} \tag{6.1.28}$$

This equation can be written in the following form in MODE.

$$\begin{aligned} u(x) = -u_5 \cdot x^5 + u_4 \cdot x^4 - u_3 \cdot x^3 + u_2 \cdot x^2 - u_1 \cdot x - u_0 \\ u(y) = 0, \end{aligned} \tag{6.1.29}$$

where the coefficients u_i for $i = 0 \div 5$ are:

$$\begin{aligned} u_5 &= 3.34 \cdot 10^2 \\ u_4 &= 3.84 \cdot 10^3 \\ u_3 &= 4.72 \cdot 10^4 \\ u_2 &= 6.52 \cdot 10^5 \\ u_1 &= 1.20 \cdot 10^7 \\ u_0 &= 4.07 \cdot 10^2. \end{aligned} \tag{6.1.30}$$

If one differentiate this potential with respect to x at the point where $x = 0$, the result will be equal to $120\,\mathrm{kV/cm}$, which is precisely the field strength for a BNL element.

After defining the potential everything is ready for the simulation performance. The simulations were made with all the terms in the potential and with only the dipole term, setting the coefficients from u_5 to u_2 inclusively to zero and leaving only u_0 unchanged. The sextupole strengths remained untouched and were set to the optimal value of the SCT. The results are plotted below for both planes, the horizontal and the vertical.

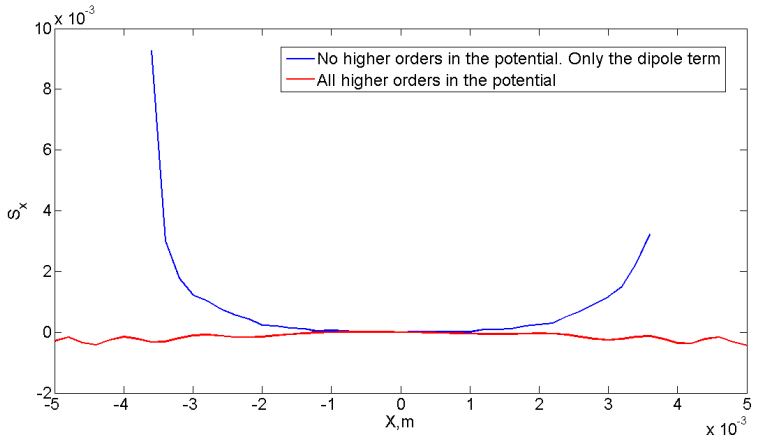

Figure 66: Blue: S_x spin components of the particles in the bunch with initial x offsets after 10^4 turns without higher orders in the potential. Red: S_x spin components of the particles in the bunch with initial x offsets after 10^4 turns with higher orders in the potential.

As seen from Figures 68 and 67 the higher orders in the electric field potential do play role in the spin motion. In fact, they have an effect on the parabola steepness and also for the horizontal spread case, they shrink the aperture of the beam.

A particle flying through a deflector or a BNL element with electric field interacts with pseudosextupole field, which was produced by the corresponding terms in the potential. This means that an electric deflector acts like a sextupole in the horizontal plane, too. This is the reason why with the previously optimal sextupole settings the longest spin coherence time decreases, when the higher orders are turned off. Indeed, a deflector has no longer a sextupole component and the sextupole correction in the whole ring is changed now.

Figure 68 demonstrates that the particles with initial offsets larger than $\approx 3.5\,\mathrm{mm}$ are lost during the tracking. MODE has produced no output for them and, therefore, no horizontal components of the spin were calculated. It was expected, since as long as some terms of the potential are set to zero, this $u(r)$ is less accurately describes the field in the deflector. The computational error increases as the distance from zero or from the design orbit grows. That is why at relatively large distances from zero, already at $3.5\,\mathrm{mm}$ the field is no longer correct. The orbit motion of the particle is significantly perturbed and the particles are lost.

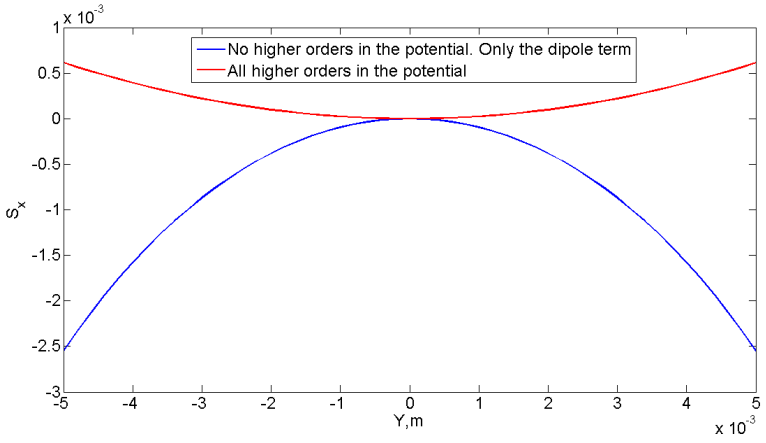

Figure 67: Blue: S_x spin components of the particles in the bunch with initial y offsets after 10^4 turns without higher orders in the potential. Red: S_x spin components of the particles in the bunch with initial y offsets after 10^4 turns with higher orders in the potential.

It is not visible in the case with the vertical beam spread because the potential is zero there. However, the change in the spin motion is there, since the sextupoles are turned on and the transverse $x - y$ coupling is present.

Turning off the higher orders in the potential didn't solve the problem of the non-parabolic behavior of the parabolas. The bents are still there. If one enlarges the center zone of Figure 68, they will be visible. The blue curve begins to wiggle for $|x| > 1\,\mathrm{mm}$. The same thing occurs for the red curve approximately in the region of $2.5 \div 3\,\mathrm{mm}$. Taking into account that the size of the beam is smaller in the case, when the higher orders are off, one concludes that these two curves have nearly the same magnitude of those bents. Nevertheless, according to the theory, the nontrivial nature of an electric potential should have an effect on the spin motion due to the presence of the octupole, the decapole components in the potential and so on. One can expand the potential up to 10-th order, for example, and observes them. The contribution from them is small, but for the high spin coherence times, which needed very precise sextupole tuning, those orders can be important.

So, the main contribution to the non-parabolic shape of the S_x dependencies on the horizontal spread comes from the RF modulation of the spin motion.

Misalignments of elements

Misalignments of elements inside a ring, as it was said in chapter 3, may significantly spoil the measurement. The most dangerous effect, which comes from a rotated magnet, for instance, is that the MDM precession

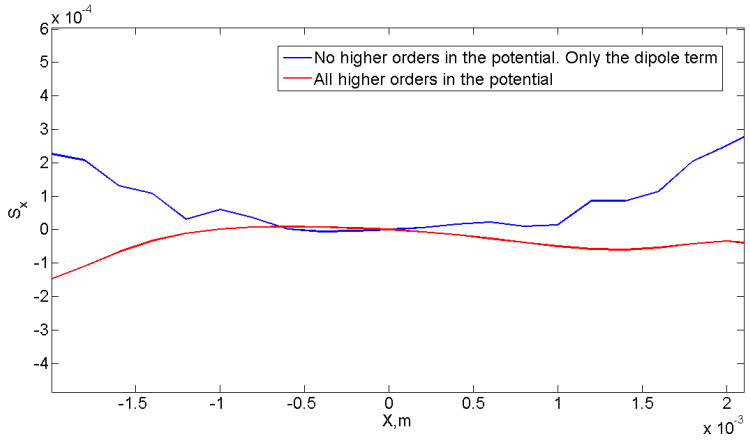

Figure 68: Blue: S_x spin components of the particles in the bunch with initial x offsets after 10^4 turns without higher orders in the potential. Red: S_x spin components of the particles in the bunch with initial x offsets after 10^4 turns with higher orders in the potential.

of the spin vector drives the polarization to the vertical plane exactly as the EDM does. Therefore, one cannot distinguish two rotations - MDM and EDM. Is there a way to solve this complicated issue? The answer is positive and the solution is simple. One should store to beams in the ring, one rotating clockwise and another with the counter-clockwise rotation.

Clockwise and counter-clockwise approach

This method of cancellation of the unwanted rotations of the spin due to the presence of misalignments was proposed by BNL [95]. One should consider a ring with a dipole, which is rotated either around the radial or the longitudinal axis (see Figure 69).

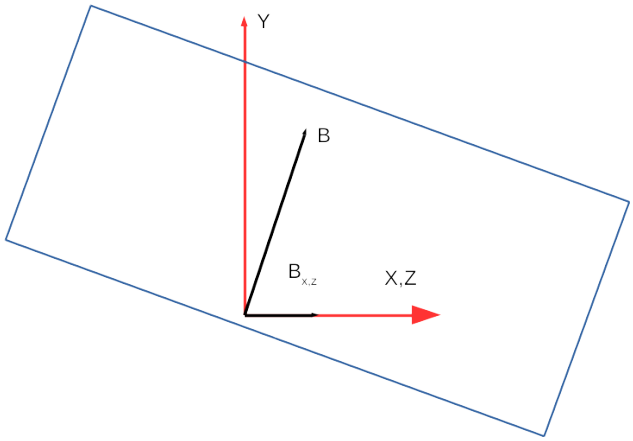

Figure 69: A dipole rotated around either X- or Z-axis.

One can write the T-BMT equation in CGS units for each projection of the spin precession

$$\begin{aligned} \frac{dS_x}{dt} &= \Omega_y S_z - \Omega_z S_y \\ \frac{dS_y}{dt} &= \Omega_z S_x - \Omega_x S_z \\ \frac{dS_z}{dt} &= \Omega_x S_y - \Omega_y S_x \end{aligned} \quad . \tag{6.1.31}$$

Since the transverse velocity is three orders less than the longitudinal one ($\beta_{x,y} << \beta_z$), the above angular frequencies of the spin rotation are represented in the following form [91]

$$\begin{aligned} \Omega_x &= -\frac{e}{mc}\left[GB_x - \left(\frac{1}{\gamma^2-1} - G\right)\beta_z E_y + \frac{\eta}{2}E_x - \frac{\eta}{2}\beta_z B_y\right] \\ \Omega_y &= -\frac{e}{\gamma mc}\left[GB_y - \left(\frac{1}{\gamma^2-1} - G\right)\beta_z E_x - \frac{e}{m\gamma}\frac{\eta}{2}E_y - \frac{e}{m\gamma}\frac{\eta}{2}\beta_z B_x\right] \\ \Omega_z &= \left[-\frac{e}{m\gamma}GB_z - \frac{e}{m\gamma}\frac{\eta}{2}E_z\right]. \end{aligned} \tag{6.1.32}$$

Firstly, the case when a dipole is rotated around X-axis will be discussed. The orbit motion is changed by the presence of B_x component of the rotated dipole. The reference particle will find a new trajectory and will no longer have all zero components in the state vector

$$\mathbf{X}_1 = \begin{pmatrix} x \\ y \\ t \\ p_x \\ p_y \\ W \end{pmatrix} = \begin{pmatrix} x_{init} \\ y_{init} \\ t_{init} \\ p_{x,init} \\ p_{y,init} \\ W_{init} \end{pmatrix} = \mathcal{M} \begin{pmatrix} x_{init} \\ y_{init} \\ t_{init} \\ p_{x,init} \\ p_{y,init} \\ W_{init} \end{pmatrix} \tag{6.1.33}$$

where $\mathcal{M}$ is the transfer map for the new ring with the rotated dipole, and $x_{init}, y_{init}, t_{init}, p_{x,init}, p_{y,init}, W_{init}$ are new initial coordinates of the reference particle. The reference particle transforms into itself after one turn around the ring. The simple but sufficient algorithm was realized in MODE program to find that new reference particle. A particle with all zero coordinates were tracked for 10^4 turns. Since the B_x component of the dipole bends the particle trajectory in the vertical direction, producing y and p_y components in the state vector, one finds an ellipse if one takes a look at the (y, p_y) phase space (see Figure 70. The longitudinal motion is perturbed, as well, because the path length is different and the equilibrium energy level is shifted, although the $\frac{\Delta p}{p}$ is of the level of 10^{-9}, which is negligibly small. Figure 71 shows the longitudinal phase space for the new ring.

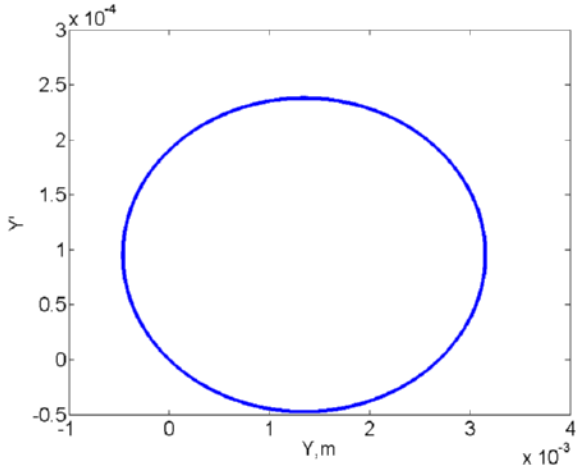

Figure 70: Vertical phase space ellipse corresponding to the presence of a B_x component of the rotated dipole in the ring.

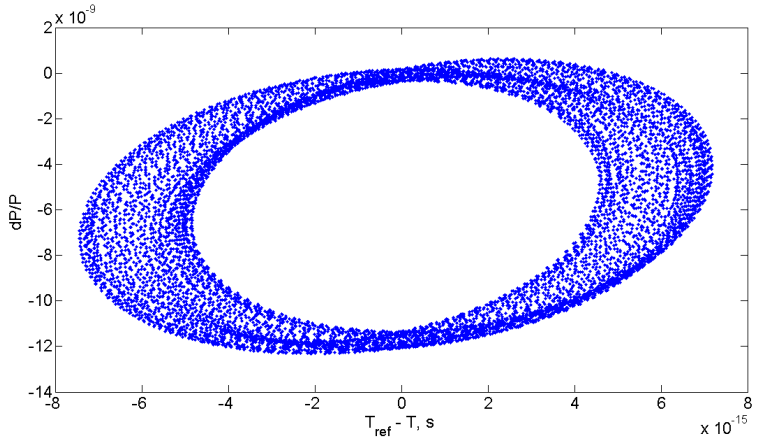

Figure 71: Longitudinal phase space ellipse corresponding to the presence of a B_x component of the rotated dipole in the ring.

Finally, the horizontal phase space (x, p_x) is changed, too. There are no kicks of the beam in the radial direction, however, the presence of non-vanishing dispersion function leads to the change in the horizontal motion. One can write a simple solution of Hill's differential equation for x-coordinate with the dispersion coefficient.

$$x = D_x \frac{\delta p}{p}, \tag{6.1.34}$$

where D_x is the dispersion in the horizontal plane. The (x, p_x) phase space is plotted in Figure 72.

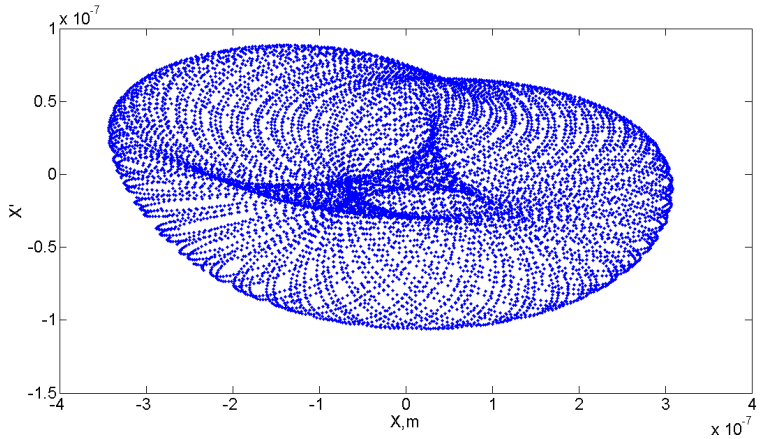

Figure 72: Horizontal phase space ellipse corresponding to the presence of a B_x component of the rotated dipole in the ring.

After the tracking, the mean values for all the components of the state vector were calculated and the new vector $\mathbf{X} = (< x >, < y >, < t >, < p_x >, < p_y >, < W >)$ was tracked again for 10^4 turns in the ring. This loop was repeated for approximately 15 times to get the precision of 10^{-15} in determination of all the reference particle's coordinates, which is the maximum precision available.

One should store the second beam in the counter-clockwise direction (CCW). The counter-clockwise motion is a tricky aspect of the modelling of spin-orbital dynamics, but it can be realized in MODE quite simply. One should multiply the existing map for the ring by the matrix $\mathcal{C}$

$$\mathcal{C} = \begin{pmatrix} 1 & 0 & 0 & 0 & 0 & 0 & 0 & 0 & 0 & 0 \\ 0 & -1 & 0 & 0 & 0 & 0 & 0 & 0 & 0 & 0 \\ 0 & 0 & 1 & 0 & 0 & 0 & 0 & 0 & 0 & 0 \\ 0 & 0 & 0 & 1 & 0 & 0 & 0 & 0 & 0 & 0 \\ 0 & 0 & 0 & 0 & -1 & 0 & 0 & 0 & 0 & 0 \\ 0 & 0 & 0 & 0 & 0 & 1 & 0 & 0 & 0 & 0 \\ 0 & 0 & 0 & 0 & 0 & 0 & -1 & 0 & 0 & 0 \\ 0 & 0 & 0 & 0 & 0 & 0 & 0 & -1 & 0 & 0 \\ 0 & 0 & 0 & 0 & 0 & 0 & 0 & 0 & -1 & 0 \\ 0 & 0 & 0 & 0 & 0 & 0 & 0 & 0 & 0 & 1 \end{pmatrix} \tag{6.1.35}$$

from both ends. Then the CCW map will be represented as

$$\mathcal{M}_{CCW} = \mathcal{C}\mathcal{M}_{CW}\mathcal{C}^{-1}, \tag{6.1.36}$$

where $\mathcal{M}_{CW}$ is the map for clockwise direction.

The orbital motion will be different for two cases. One can see (Figure 73) the difference in vertical phase space ellipses for CW and CCW particle movement in the ring. This difference indicates that for the initial CCW particle coordinates the coordinates of the reference particle, which were obtained above, should be chosen but with the different sign in y and p_y components of the state vector. If one makes such a choice, then the counter-clockwise particle will have exactly the same trajectory as the clockwise one but will be bended in the opposite direction, either up or down, depending on the sign of the B_x component of the rotated dipole. Other phase space ellipses for longitudinal and horizontal planes remain unchanged.

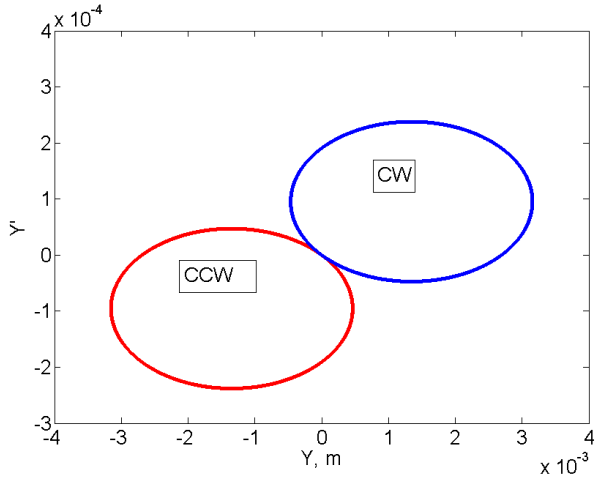

Figure 73: Vertical phase space ellipses for clockwise and counter-clockwise stored beams in the presence of a B_x component of the rotated dipole in the ring.

One can measure this separation of trajectories and find the value for a B_x component. However, there is no need for that, since the EDM signal can be measured directly in this approach.

As soon as the new reference particles are found for CW and CCW directions, one can consider the spin motion of those particle. If the ring is ideal, except for one dipole, apart from usual spin precession in the horizontal plane, which is equal to the momentum precession, one will have a slow rotation of the spin in the vertical direction due to the MDM interaction with the B_x component of the rotated dipole. The EDM signal is also there and rotates the spin in the same direction. The T-BMT equation for the vertical spin component for both directions of the particle motion is written as

$$\frac{dS_y}{dt}^{CW,CCW} = \Omega_z^{CW,CCW} S_x^{CW,CCW} - \Omega_x^{CW,CCW} S_z^{CW,CCW} \tag{6.1.37}$$

Since there are no longitudinal fields involved, $\Omega_z^{CW,CCW}$ for both CW and CCW directions are zero and

$$\frac{dS_y}{dt}^{CW,CCW} = -\Omega_x^{CW,CCW} S_z^{CW,CCW}. \tag{6.1.38}$$

Defining clockwise and counter-clockwise directions with indices $CW = \alpha, CCW = \beta$ will shorten the formulas. Then the angular spin precession frequencies in the horizontal plane without any vertical electric field are

$$\begin{aligned} \Omega_x^{\alpha} &= -\frac{e}{mc}\left[GB_x - \frac{\eta}{2}E_x + \frac{\eta}{2}\beta_z^{\alpha}B_y\right] \\ \Omega_x^{\beta} &= -\frac{e}{mc}\left[GB_x - \frac{\eta}{2}E_x + \frac{\eta}{2}\beta_z^{\beta}B_y\right] \end{aligned} \tag{6.1.39}$$

The fields are written in the laboratory coordinate system and they don't change the direction, when the direction of particle motion is changed. So, the sign in the velocity will be different $\beta_z^{\beta} = -\beta_z^{\alpha}$, and also the spin direction will be opposite. The CW particle is tracked with initial $S_z^{\alpha} = 1$ spin aligned with the momentum and pointing in the direction of flight. The same is true for the CCW particle - $S_z^{\beta} = -1$. Taking into account all the statements written above, the sum of two spin precessions is read

$$\begin{aligned} \frac{dS_y}{dt}^{\alpha} - \frac{dS_y}{dt}^{\beta} &= -\Omega_x^{\alpha} S_z^{\alpha} - \Omega_x^{\beta} S_z^{\beta} = -\Omega_x^{\alpha} \cdot 1 - \Omega_x^{\beta} \cdot (-1) = \\ = \frac{e}{mc}\left[GB_x - \frac{\eta}{2}E_x + \frac{\eta}{2}\beta_z^{\alpha}B_y\right] &- \frac{e}{mc}\left[GB_x - \frac{\eta}{2}E_x + \frac{\eta}{2}(-\beta_z^{\alpha})B_y\right] = \\ &= 2\frac{\eta}{2}\beta_z B_y \frac{e}{mc}. \end{aligned} \tag{6.1.40}$$

Equation 6.1.40 proves the interesting fact. When the beams with opposite velocities are stored in the ring the MDM precession terms arising due to the interaction with the radial field of a rotated dipole cancel each other, and the term, which is left, is a doubled EDM signal. However, this is true only for the reference particles. In other words, equation 6.1.40 works for the situation when a particle makes a turn around a ring, and it is tracked backwards with the opposite spin direction from the exact point, where it finished the first turn, but with the opposite signs in y and p_y state vector components.

Simulation of CW and CCW approach for the frozen spin method for the reference particles

The frozen spin method was taken into consideration, at first. In the presence of the radial fields, as it was mentioned above, the reference trajectory is no longer coincides with the designed closed orbit that implies that the reference particle has all zero components of the state

vector. Since the new closed orbit and the reference particle,too, are different, the S_x spin projection doesn't stay zero all the time because the frozen spin condition 5.2.3 is no longer fulfilled. And if one has the non-vanishing S_x component it will produce the vertical polarization build-up in case, when the longitudinal fields are present, that means in real life it will be always the case.

$$\left(\frac{1}{\gamma^2-1}-G\right)\frac{\vec{\beta}\times\vec{E}}{c}+G\vec{B}\neq 0. \tag{6.1.41}$$

Indeed, the energy of the new reference particle is changed and with the calculated B and E fields inside the E+B elements the particle spin is no longer parallel to the momentum. This leads to the growth of the S_x projection, which is demonstrated in Figure 74

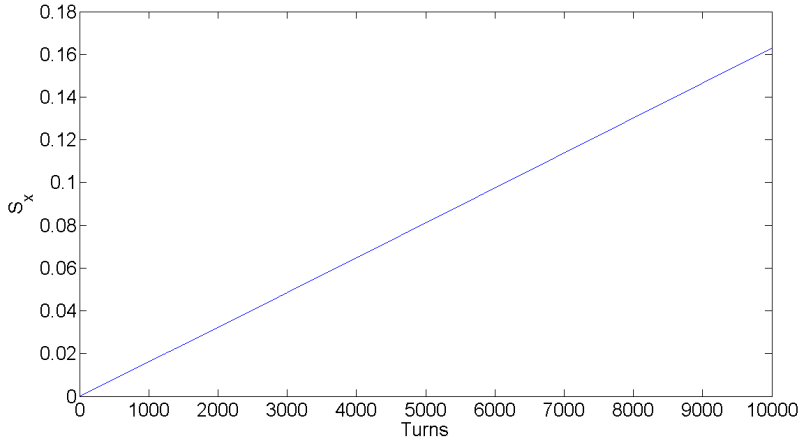

Figure 74: The growth of the S_x component in the presence of the rotated around the longitudinal axis BNL elements.

However, in reality one can tune the B-field and find the situation, when the value of S_x component stays zero all the time. Another possibility is to change the γ-factor of the reference particle. The formula for the frozen spin condition,

$$\left(\frac{1}{\gamma^2-1}-G\right)\frac{\vec{\beta}\times\vec{E}}{c}+G\vec{B}=0, \tag{6.1.42}$$

allows both options to be realized. The simulations was made for various particle energies and the reference particle's S_x spin component were monitored. Figure 75 illustrates the dependence of the S_x spin component on the particle energy in time. Different lines represent various initial energies of the particle. Taking a look at this figure, one can conclude that there exists a particular energy, at which the horizontal spin projection stays constantly equal to zero in time.

For the case, when the BNL elements are rotated around the longitudinal axis, leading to the increase of S_x spin projection, the following

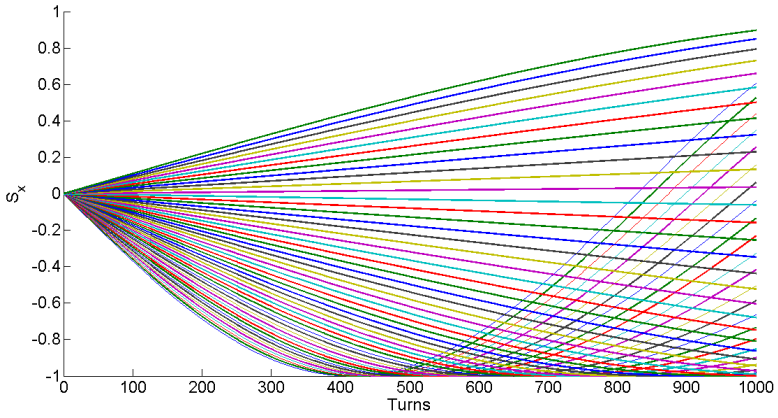

Figure 75: S_x spin component for different particle energies with respect to the number of turns. Each line represents a particlural initial energy in the range $\frac{\Delta p}{p} \in [-10^{-4}; 10^{-4}]$ with the steps of $3.92 \cdot 10^{-6}$.

technique was used in the simulations. For the simplicity of calculation and analysis, the S_x was rotated backwards each turn manually, meaning mathematically. The kick of the S_x was calculated after each revolution in the ring and subtracted in the tracking process. Nevertheless, the situation without this subtraction was also considered and checked. It will be discussed further, when the bunch of particles is investigated and when the rotations of the elements are made around the radial axis (in this case S_x subtraction is no longer possible at all).

Two reference particles were tracked in opposite directions, all the E+B elements were rotated randomly, according to Gauss distribution with the mean value $\mu = 0$ and the standard deviation $\sigma = 10^{-4}$rad. Initially the EDM was turned off completely in the simulation and the polarization build-up corresponding to the MDM interaction with the radial magnetic fields of the rotated elements was calculated for both cases. The sum of two MDM signals was exactly equal to zero. Afterwards, the EDM term was turned on, it was set to $10^{-21}\,\mathrm{e}\cdot\mathrm{cm}$, which corresponds to $\eta = 10^{-7}$. The predicted behavior of the S_y component was observed and the EDM signal was extracted from summation of two polarization build-ups in the presence of non-vanishing EDM. The extracted EDM value coincided with the initially set value. The result is shown in Figure 76. The simulation proved the theoretical considerations and showed that for the two reference particles stored in the opposite direction one can get a pure EDM signal with the MDM rotation cancellation.

However, the clockwise-counter-clockwise method will not work on its own for the following reason why. One should examine Figure 77. As long as the B_x components of the rotated dipoles or BNL elements are present the S_y component grows. The angular frequency of the MDM

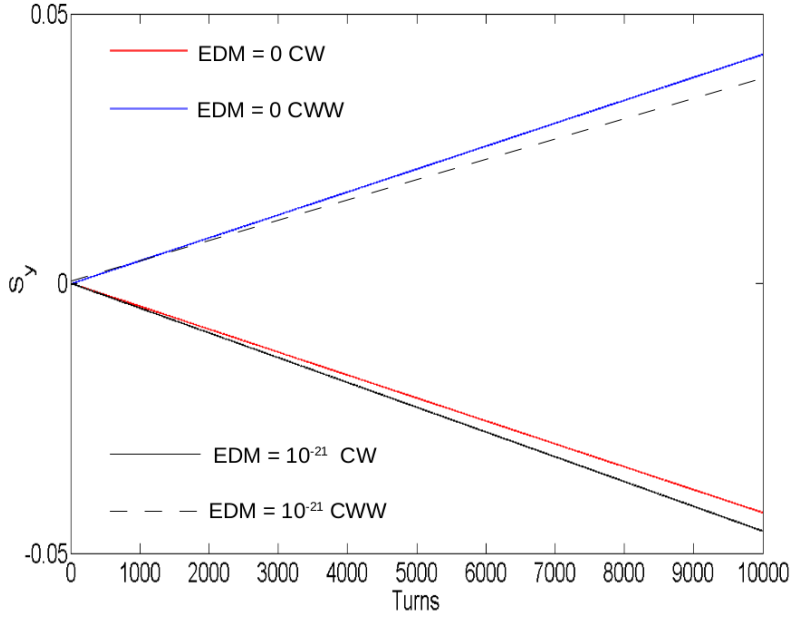

Figure 76: The build-up of the vertical polarization. In red: the polarization build-up due to the MDM interaction with B_x component of the rotated BNL elements, when the EDM was turned off for CW direction. In blue: the polarization build-up due to the MDM interaction with B_x component of the rotated BNL elements, when the EDM was turned off for CCW direction. In black, solid line:the polarization build-up due to the MDM and the EDM interaction with B_x component of the rotated BNL elements, when the EDM was $10^{-21}\,\mathrm{e}\cdot\mathrm{cm}$. In black, dashed line:the polarization build-up due to the MDM and the EDM interaction with B_x component of the rotated BNL elements, when the EDM was $10^{-21}\,\mathrm{e}\cdot\mathrm{cm}$.

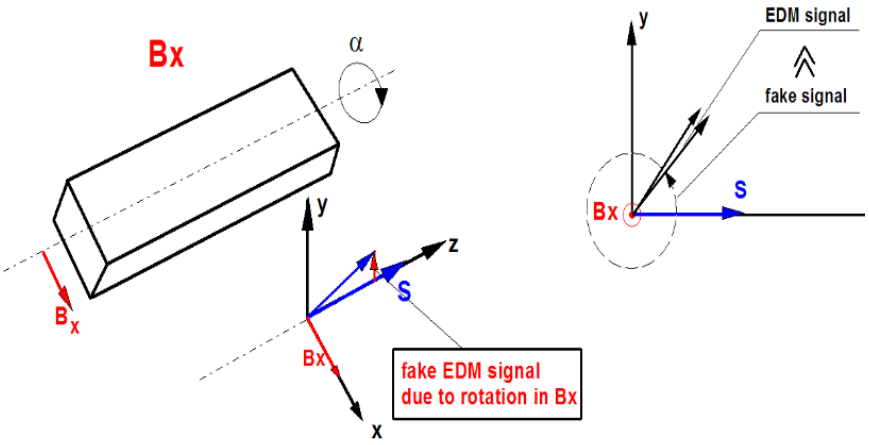

Figure 77: A dipole rotated around the longitudinal axis and the scheme of the spin rotation generated by a B_x component of the magnetic field.

rotation linearly depends on the radial component of B-field and is much more bigger than the EDM rotation.

$$\Omega_{B_x} = \frac{e}{m\gamma} \cdot \gamma G B_x >> \Omega_{EDM}, \tag{6.1.43}$$

where Ω_{B_x} is the angular spin frequency due to the interaction of the magnetic dipole moment with the integral B_x component of the field of the rotated BNL elements, and Ω_{EDM} is the frequency corresponded to the EDM presence. In this situation, the vertical spin component begins to rotate around the radial magnetic field. S_y increases, reaches the value of nearly 1, decreases until -1 and the process repeats. Thus, S_y oscillates with some frequency in time. One has a look at two solutions of the T-BMT equation (6.1.44) for the longitudinally polarized beam.

$$\begin{aligned} S_x(t) &= \frac{\Omega_y \sin(\sqrt{\Omega_x^2 + \Omega_y^2} \cdot t)}{\sqrt{\Omega_x^2 + \Omega_y^2}} \\ S_y(t) &= -\frac{\Omega_x \sin(\sqrt{\Omega_x^2 + \Omega_y^2} \cdot t)}{\sqrt{\Omega_x^2 + \Omega_y^2}}, \end{aligned} \tag{6.1.44}$$

where $\Omega_{x,y}$ are angular frequencies of spin rotation around x and y axes.

$$\begin{aligned} \Omega_x &= \Omega_{EDM} + \Omega_{B_x} \\ \Omega_y &= 0. \end{aligned} \tag{6.1.45}$$

The angular frequency Ω_y is equal to zero only for the reference particle, it is not true for the bunch of particles and it will be discussed in the next subsection. Also, one should remember that the rotation is considered relative to the momentum. In the lab frame Ω_y equals to the momentum precession frequency.

Therefore, one can write down the formula for S_y oscillations in the absence of Ω_y.

$$S_y(t) \approx -\sin(\Omega_{B_x} + \Omega_{EDM}) \cdot t. \tag{6.1.46}$$

The simulation result is plotted in Figure 78. Half of the oscillation period

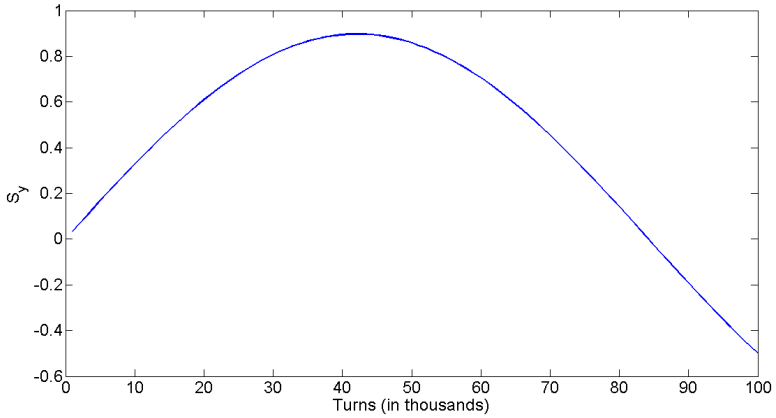

Figure 78: Oscillation of S_y spin projection of the reference particle due to the interaction of the spin vector with B_x component of the field of the rotated BNL elements in.

takes approximately 80 thousand turns when the elements are rotated by $\langle \alpha \rangle = 10^{-4}$ rad. This is unacceptable for the future EDM experiment, since when S_y reaches its maximum value and begins to decrease, the spin vector at this moment is pointing in the direction opposite to the momentum. Hence, the EDM build-up of the vertical polarization is finished and the EDM starts to rotate the spin downwards. In other words, the EDM build-up oscillates around zero together with S_y component of the spin vector and cannot be observed. There are two possible solutions and outcomes in this case. They will be discussed later in the next subsection, since the consideration of a whole bunch of particles is needed.

Rotation of the elements around the radial axis will be investigated below, since there is no point of doing it for the reference particle. Indeed, if the reference particle is tracked in the ring, where inclined BNL elements produces B_z component of the field, the spin of the reference particle will not be affected, since it lays along z axis pointing in the direction of the momentum. Nevertheless, the orbit is changed when such a rotation takes place and the spin will be no longer frozen. As was mentioned before, the tuning of the B-field and energy of the reference particle will help to find the situation, when the spin remains parallel to

the momentum all the time. Thus, there is no need to examine this case. However, when a bunch of particles is involved the longitudinal field (B_z) dramatically changes the whole spin behavior and represents the main threat for the experiment.

CW and CCW simulations for a bunch of particles for the frozen spin method

In order to draw conclusions and set the a systematic limit for the upcoming EDM experiment one needs to examine a bunch of particles. This will be done for the frozen spin method, since the results are nearly identical for the quasi-frozen spin approach.

A bunch of particles was distributed along the radial axis. Firstly, the situation when the BNL elements are rotated along the longitudinal axis (Figure 77) will be discussed. A number of simulations were performed, so one particular case, when the EDM was equal to $10^{-21}\,\mathrm{e}\cdot\mathrm{cm}$ ($\eta = 10^{-7}$), will be examined. The average rotation angle was also set to $10^{-4}\,\mathrm{rad}$. Four simulations were made: clockwise stored beam with EDM$=0$, counterclockwise stored beam with no EDM and the same simulations but with turned on EDM. The result is shown in Figure 79.

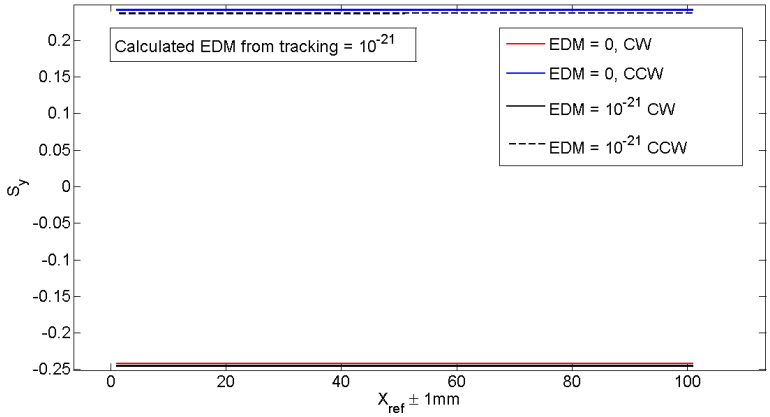

Figure 79: S_y spin component after 10^4 turns for a bunch of particles distributed along the radial axis. In red: the polarization build-up due to the MDM interaction with B_x component of the rotated BNL elements, when the EDM was turned off for CW direction. In blue: the polarization build-up due to the MDM interaction with B_x component of the rotated BNL elements, when the EDM was turned off for CCW direction. In black, solid line:the polarization build-up due to the MDM and the EDM interaction with B_x component of the rotated BNL elements, when the EDM was $10^{-21}\mathrm{e}\cdot\mathrm{cm}$. In black, dashed line:the polarization build-up due to the MDM and the EDM interaction with B_x component of the rotated BNL elements, when the EDM was $10^{-21}\mathrm{e}\cdot\mathrm{cm}$.

Those lines are parabolas with opposite curvatures. One can zoom into the picture and convince oneself (see Figure 80 They are identical but

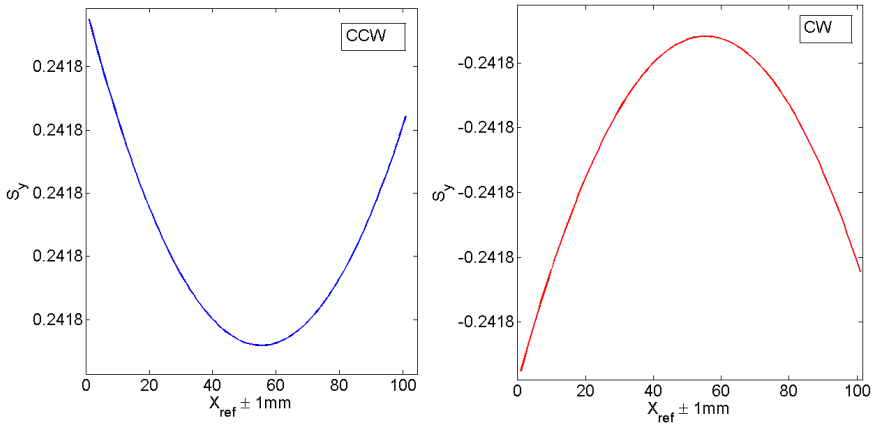

Figure 80: S_y spin components for clockwise and counter-clockwise tracking.

reversed. Therefore, when one subtracts one from another the only thing that is left is pure EDM signal corresponding to the equation 6.1.40. The EDM was calculated from the tracking results and it coincided ideally with the value, which was set in MODE.

When a bunch of particles is considered, the decoherence in the horizontal plane is always present. Then the angular frequency of the spin rotation around the vertical axis won't be zero. In fact, it will have the form

$$\Omega_y = \langle \delta\Omega_{decoh} \rangle, \tag{6.1.47}$$

where $\langle \delta\Omega_{decoh} \rangle$ is the average value of the vertical angular frequency, for which the decoherence is responsible. This frequency is the average value for all particles in a bunch and it changes in time. That is why notation δ is used. To understand this issue clearer one should take a look at the simulation results shown in Figure 81. The plot illustrates the difference between the S_x component of the reference particle and the S_x component of the particle tracked with the largest initial x offset, which was equal to $1\,\mathrm{mm}$, from the x coordinate of the newly found reference trajectory for the ring with misalignments. So this value, basically, shows the range of the horizontal spin projections inside a bunch of particles or the curvature of the parabola, which can be plotted for the S_x component similarly as it was done for the S_y component in Figure 80.

Explanation of this phenomenon is given below. The presence of the B_x field in the ring causes the spin to rotate around the radial axis. In the same time, the decoherence takes place in the horizontal plane. The particles' spins are not aligned anymore, that is they have different S_x components. They form some kind of a "fan", which becomes wider in time. This "fan" rotates around the radial axis and finally it points upwards. It happens after 40000 turns approximately if one throws a glance at Figure

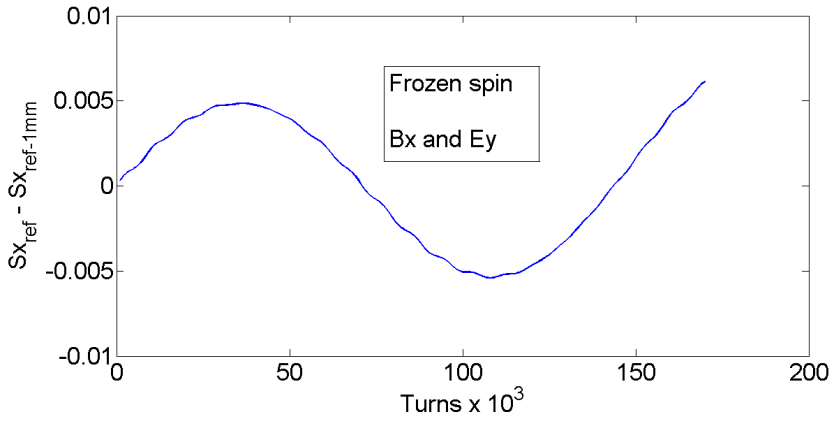

Figure 81: The oscillation of the difference between the S_x spin component of the reference particle and the S_x spin component of the particle with the largest initial offset in x direction in the presence of B_x.

81. The "fan" continues its rotation around the radial axis, however it becomes more narrow, its width decreases. This happens due to the fact that the spins, which build this "fan", point in the opposite direction. Then the process repeats.

Alternatively, one can think of it as of the oscillation of the curvature of the parabola, which represents the spin decoherence in the horizontal plane. Initially the parabola is a straight line because all the spins are aligned, later it obtains its parabolic shape and becomes more steeper with time and at some point it reaches its maximum curvature. It happens exactly at the time, when the S_y spin component hits its peak value. Afterwards, the parabola begins to shrink again, forms a straight line and starts to bend in the other direction. Both explanations are schematically illustrated in Figure 82 and Figure 83.

Taking into account the explanation above and the equation 6.1.44, one can write the expression for the average horizontal component of the spin vector.

$$\langle S_x(t)\rangle = \frac{\langle \delta\Omega_{decoh}\rangle}{\Omega_{B_x}} \sin\Omega_{B_x} t, \tag{6.1.48}$$

Now, everything is ready to discuss the issue of the spin rotation around the radial axis, which results in cancellation of the EDM build-up. As was mentioned before, this spin rotation kills the EDM signal and there are two possible ways to solve it.

The first possibility is straightforward. One has to install all the elements in the ring with the maximum available precision. When the elements were rotated by an average angle of 10^{-4} rad the rate of the spin precession in the vertical plane was equal to $\frac{dS_y}{dt} \sim 10^{-5}$ rad per revolution. The S_y spin component should not exceed 1 rad for 10^9 turns because this time is needed to observe an EDM signal if one assumes that the EDM is of the order of $10^{-29}\, e{\cdot}$cm. This condition requires the

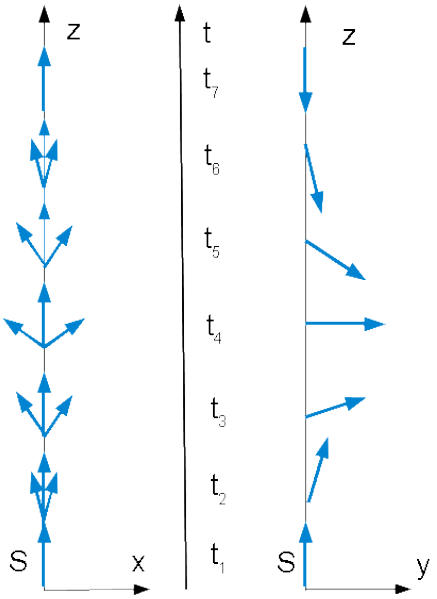

Figure 82: Osclillation of the width of the "fan" of particles' spins due to the presence of a B_x.

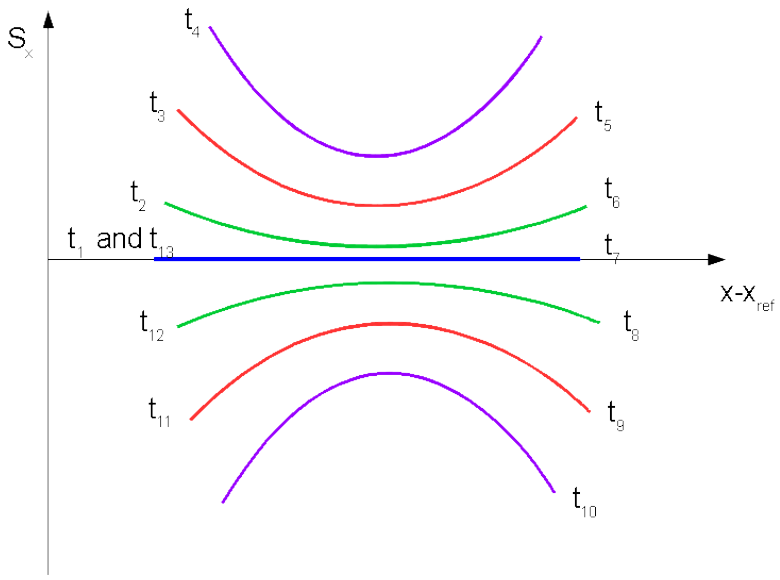

Figure 83: Oscillation of the curvature of the parabola, which represents the spin decoherence in the horizontal plane.

installation accuracy of the order of 10^{-9} rad, which is close to impossible. When the alignment is done, as accurate as possible, one has to apply CW and CCW method, described above. The field must be reversed to store the beam in the opposite direction. This is where the bunch of particles comes in handy. One would calibrate the magnetic field by the beam energy measured via spin tune observation in the horizontal plane, which will be equal to Ω_y. Then the two signals from CW and CCW runs must be subtracted to obtain an EDM signal. Current test runs at COSY demonstrated the relative accuracy of spin tune determination of 10^{-10} per 100 seconds [38]. However, the absolute accuracy of spin precession frequency is of the order of $10^{-5} - 10^{-6}$ Hz depending on the measurement time.

Assuming that all the elements were aligned with the 10^{-9} rad precision, the magnetic field was calibrated via spin precession frequency measurement with 10^{-6} Hz accuracy, the EDM limit in this case will only be equal to $10^{-25} \div 10^{-26}$ e·cm. One gets this value because the field measurement accuracy plays the final role in the evaluation. Since the B-field can be reversed only with that precision, there will be no chance of distinguishing between the EDM signal or fake MDM rotations that will arise due to non-equality of the magnetic fields for clockwise and counter-clockwise settings. In order to measure the EDM at the level of 10^{-29} e·cm, one has to measure the spin precession frequency with the precision of at least 10^{-9} Hz for 1000 seconds.

The second option is the frequency measurement instead of the polarization build-up [92]. Again, the elements must be installed with the maximum precision. However, the small modification for the ring elements must be made. Weak trim dipoles should be placed after each BNL element or in one place in the ring - this makes no difference. The scheme of such a trim dipole is shown in Figure 84.

The setting of a trim dipole can be realized as it's pictured above. One can use a small number of windings to create a radial magnetic field. The direction of the field shouldn't be strictly parallel to the x axis, it is not needed for the compensation of a B_x component of a BNL element. Figure 84 also illustrates the compensation principle. If a BNL element or a regular dipole for the quasi-frozen spin lattice is rotated around the longitudinal axis, yielding the B_x field component, this small radial field can be compensated by simply varying the amplitude of the magnetic field of the trim dipole. How it helps to measure the EDM will be explained further.

The solutions of the T-BMT equations, as it was written earlier, are

$$\begin{aligned} S_x(t) &= \frac{\Omega_y \sin(\sqrt{\Omega_x^2 + \Omega_y^2} \cdot t)}{\sqrt{\Omega_x^2 + \Omega_y^2}} \\ S_y(t) &= -\frac{\Omega_x \sin(\sqrt{\Omega_x^2 + \Omega_y^2} \cdot t)}{\sqrt{\Omega_x^2 + \Omega_y^2}}, \end{aligned} \tag{6.1.49}$$

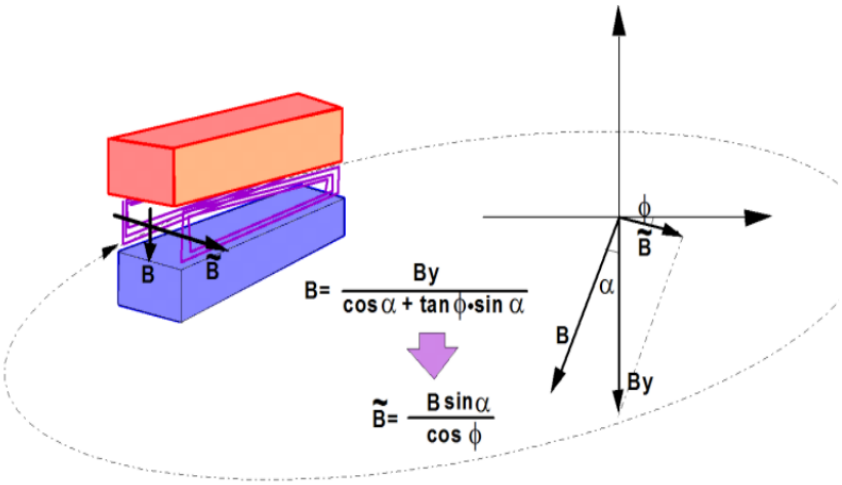

Figure 84: A scheme of a trim dipole installation and the resulting B-field compensation.

With a realistic installation accuracy of all elements of $10\,\mu$m, one can get the angular spin frequency of the order of $\Omega_{B_x} \approx 10\,\mathrm{rad/s}$, which is much larger than Ω_y for the frozen or quasi-frozen spin concepts. Then the following is true

$$\Omega_x = \Omega_{B_x} + \Omega_{EDM} \gg \Omega_y, \tag{6.1.50}$$

where $\Omega_y = \langle \Omega_{decoh} \rangle$, as in the previous notation.

For the sake of understanding, one should write one more time the simplified solutions of the T-BMT equation. The ratio between those two frequencies can easily be obtained of the order of $\frac{\Omega_y}{\Omega_x} \ll 10^{-5}$. Therefore, the square root in the solution of the T-BMT equation can be written as

$$\sqrt{\Omega_x^2 + \Omega_y^2} = \Omega_x \left(1 + \frac{1}{2}\left(\frac{\Omega_y}{\Omega_x}\right)^2 + \ldots\right), \tag{6.1.51}$$

and will be smaller than 10^{-10}. Once again, one obtains the solutions in the simple form

$$\begin{aligned} S_x(t) &= \frac{\Omega_y}{\Omega_{B_x}} \sin \Omega_{B_x} t \\ S_y(t) &= -\sin\left(\Omega_{B_x} + \Omega_{EDM}\right) t. \end{aligned} \tag{6.1.52}$$

This means that $S_x(t) \sim \frac{\Omega_y}{\Omega_{B_x}}$ oscillates with the amplitude, which is close to zero, and $S_y(t)$ oscillates with the total frequency $\Omega_{B_x} + \Omega_{EDM}$.

One can measure the difference in the oscillation of the vertical spin component for the clockwise and counter-clockwise case. In other words,

one determines the frequency of the spin rotation for both cases, which consists only of the EDM precession and MDM rotations around the radial magnetic fields. All other components will be negligible and will have only infinitely small quadratic contributions to the measured frequency. The resulted signal will be equal to $2\,\Omega_{EDM}$. Indeed,

$$\begin{aligned} \Omega_x^{CW} &= \Omega_{B_x} + \Omega_{EDM} \\ \Omega_x^{CCW} &= -\Omega_{B_x} + \Omega_{EDM} \\ \Omega_{EDM} &= \frac{1}{2}\left(\Omega_x^{CW} + \Omega_x^{CCW}\right). \end{aligned} \tag{6.1.53}$$

The simulation for this approach was made. Figure 85 demonstrates different spin tune for CW and CCW launched beams. The difference between the two is the desired EDM signal, when the magnetic fields are reversed ideally.

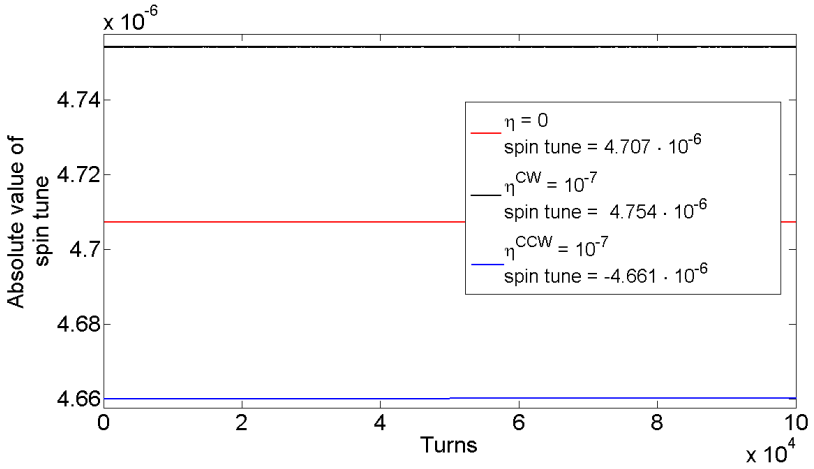

Figure 85: Spin tune difference between clockwise and counter-clockwise beams in the presence of the EDM of the order of $10^{-21}\,e\cdot\mathrm{cm}$.

In reality, the field reversal is far from ideal, and one has to take this into account. Now, why does one need those correction trim dipoles? They are used in the calibration procedure of the particle energy, when the fields are reversed. The calibration procedure is performed in a horizontal plane in order to measure the oscillation frequency of the spin with respect to the energy. To keep the spin rotation only in the horizontal plane, one uses the transverse trim dipoles with a horizontal magnetic field which compensate the oscillation of the spin in the vertical plane due to the B_x component. The full compensation is not needed, one has to just minimize the vertical oscillations in order to fulfill the following condition $\frac{\Omega_x}{\Omega_y} \ll 10^{-6}$. If Ω_x is suppressed down to $10^{-6}\,\mathrm{Hz}$ with the trim coils, one gets $\frac{\Omega_x}{\Omega_y} \approx 10^{-6}$. In this case, the square root in the T-BMT solution is

$$\sqrt{\Omega_x^2 + \Omega_y^2} = \Omega_y\left(1 + \frac{1}{2}\left(\frac{\Omega_x}{\Omega_y}\right)^2 + \ldots\right) \tag{6.1.54}$$

with the accuracy of 10^{-12}. Therefore, the solutions can be simplified as

$$\begin{aligned} S_x(t) &= \sin \Omega_y t \\ S_y(t) &= \frac{\Omega_x}{\Omega_y} \sim 10^{-6}. \end{aligned} \tag{6.1.55}$$

As a result, one can determine $S_x(t)$ with the spin tune measurement technique, when the spin precesses in the horizontal plane. The EDM precession and Ω_{B_x} contributes only quadratically to S_x and this impact is negligible. Varying the field of main dipoles all of which must be powered by one power supply, one finds the point for clockwise and counter-clockwise circulation of the beam, where the spin precession frequencies are the same. If the the frequencies for CW and CCW direction are the same, the reference particles for both bunches have exactly the same energy. This corresponds to the situation, when the amplitudes of the magnetic fields of the main dipoles before and after the reversal procedure are effectively equal to each other. The precision of the spin frequency measurement determines the precision of the field reversal. As was mentioned earlier the absolute accuracy of spin frequency determination is $10^{-6}\,\mathrm{Hz}$ for 1000 seconds measurement interval. Therefore, one can calibrate the fields with this precision. Nevertheless, this technique requires further studies, even though it seems to be very promising.

Taking into account the calibration procedure, one concludes that the absolute values of $\Omega_{B_x}^{CW}$ and $\Omega_{B_x}^{CCW}$ will be equal with the precision of $10^{-6}\,\mathrm{Hz}$. The EDM precession frequency for the EDM of $10^{-26}\,e\cdot\mathrm{cm}$ is $10^{-6}\,\mathrm{Hz}$. So adding two frequencies from CW and CCW measurements, one can only be sensitive to the EDM of the order $10^{-25} - 10^{-26}\,e\cdot\mathrm{cm}$.

This result fully coincides with the result described for the first measurement option, however this technique is more realistic and achievable nowadays, since the installation accuracy of the elements is realistic and realizable in present accelerators.

The more important and difficult problem is the rotation of the elements around the transversal axis. In this case, the B_z component of the magnetic field is present and the depolarization of the beam in the horizontal plane inevitably leads to the build-up of the vertical S_y component, which mimics the EDM signal. In chapter 3, this was briefly discussed in the section about geometric phases. Indeed, the rotation of the S_x component of the spin vector around the longitudinal magnetic field results in the creation of the fake EDM build-up. This is pictured in Figure 86

The solution of the T-BMT equation for this case is the following

$$\begin{aligned} S_x(t) &= \frac{\Omega_y \sin(\sqrt{\Omega_z^2 + \Omega_y^2}\cdot t)}{\sqrt{\Omega_z^2 + \Omega_y^2}} \\ S_y(t) &= \frac{\Omega_y \Omega_z}{\Omega_z^2 + \Omega_y^2}[1 - \cos(\sqrt{\Omega_z^2 + \Omega_y^2}\cdot t)], \end{aligned} \tag{6.1.56}$$

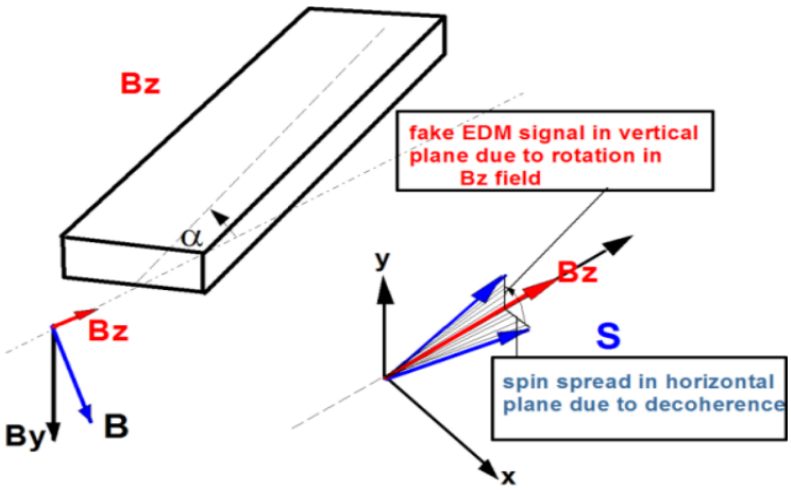

Figure 86: A dipole rotated around the transversal axis and the scheme of the spin rotation generated by the decoherence and B_z component of the magnetic field.

where Ω_z is the angular frequency of the spin rotation around the longitudinal axis due to the presence of the finite B_z component of an inclined magnet.

$$\Omega_z = \Omega_{B_z} \tag{6.1.57}$$

Ω_y, as usual, equals to $\langle \delta\Omega_{decoh} \rangle$. Then, the two cases are possible: $\Omega_{B_z} \ll \langle \delta\Omega_{decoh} \rangle$ or $\Omega_{B_z} \gg \langle \delta\Omega_{decoh} \rangle$. The solutions of the T-BMT equation are

$$\begin{aligned} \langle S_x(t) \rangle &= \sin(\langle \delta\Omega_{decoh} \rangle \cdot t) \\ \langle S_y(t) \rangle &= \frac{\Omega_{B_z}}{\langle \delta\Omega_{decoh} \rangle}[1 - \cos(\langle \delta\Omega_{decoh} \rangle \cdot t)], \end{aligned} \tag{6.1.58}$$

when $\Omega_{B_z} \ll \langle \delta\Omega_{decoh} \rangle$ and

$$\begin{aligned} \langle S_x(t) \rangle &= \frac{\langle \delta\Omega_{decoh} \rangle}{\Omega_{B_z}} \sin(\Omega_{B_z} \cdot t) \\ \langle S_y(t) \rangle &= \frac{\Omega_{B_z}}{\langle \delta\Omega_{decoh} \rangle}[1 - \cos(\Omega_{B_z} \cdot t)], \end{aligned} \tag{6.1.59}$$

when $\Omega_{B_z} \gg \langle \delta\Omega_{decoh} \rangle$.

The simulation for a bunch of particles were made in MODE. The spin motion was investigated. The results are plotted below.

Similarly to the situation when a B_x component is present, the existence of the longitudinal magnetic field leads to the oscillation of the curvature of the parabola for the S_x and S_y spin projections. This means that the width of the spin "fan" in the horizontal plane oscillates in time, as it

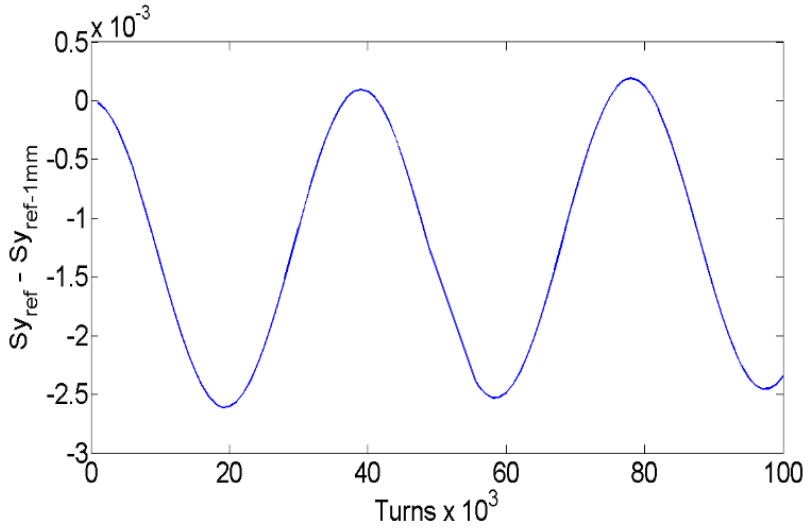

Figure 87: The oscillation of the difference between the S_y spin component of the reference particle and the S_y spin component of the particle with the largest initial offset in x direction in the presence of B_z.

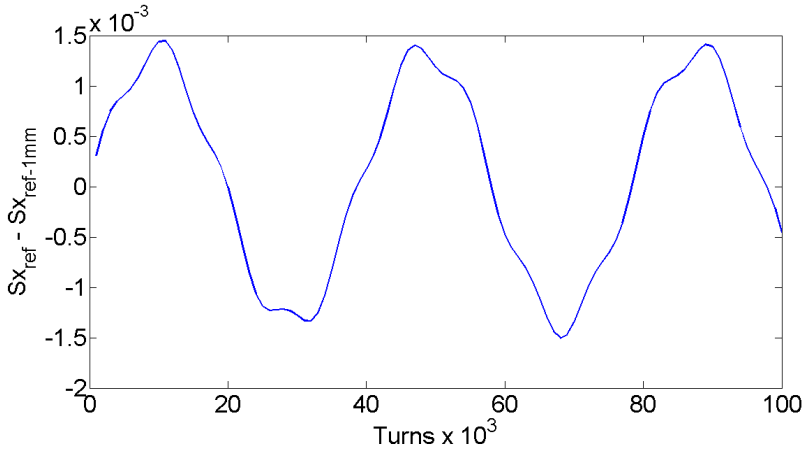

Figure 88: The oscillation of the difference between the S_x spin component of the reference particle and the S_x spin component of the particle with the largest initial offset in x direction in the presence of B_z.

was described earlier. This "fan" also rotates around z axis, building the oscillating "fan" in the vertical plane. So the vertical spin component oscillates as number of turns increases, which is shown in the equations 6.1.58 and 6.1.59. The EDM signal oscillates, too, resulting in the total averaging of the EDM build-up to zero. So, when there are inclined magnets or, basically, any elements, with finite size of the beam, with finite value of spin coherence time the EDM signal can't be observed due to the transformation of the decoherence in the horizontal plane to the oscillating vertical polarization, which totally smears out the EDM interaction.

The only solution to this problem is analogous to the case for the longitudinally rotated magnets. One should install solenoids at both ends of an element. The scheme is pictured below in Figure 89.

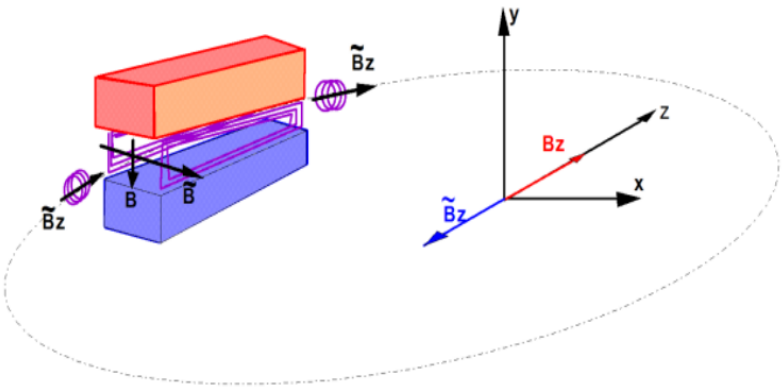

Figure 89: A scheme of solenoids installation and the resulting B-field compensation.

The solenoids must be tuned similarly, as was explained above for B_x compensation. The goal is to achieve the Ω_{B_z} value close to 10^{-9} rad/turn.

This seems to be the only way to correct the geometrical phase contribution to the experiment. Afterwards, the clockwise-counter-clockwise approach should be used in the difference in two angular spin frequencies will give the EDM signal, analogously to the situation with B_x. The fields for CW and CCW direction should be calibrated by the spin tune measurement, as well. Therefore, taking the accuracy of spin frequency measurements of 10^{-6} Hz the final EDM signal systematic limit can be set to $10^{-25} \div 10^{-26}\, e{\cdot}$cm.

Conclusion

Consideration of the main systematic errors for the quasi-frozen and the frozen spin methods demonstrated that for the existing accuracy of the spin tune determination the precision, with which one can measure an EDM at a storage ring, using clockwise and counter-clockwise stored beams, is of the order of $10^{-25} \div 10^{-26}\, e{\cdot}\text{cm}$.

SYSTEMATIC ERRORS CONSIDERATION FOR THE PRECURSOR EDM EXPERIMENT AT COSY

Introduction

The main systematic effects arising in the RF Wien filter method, which is going to be used for the EDM experiment at COSY, will be considered in this section. COSY ring was chosen as a starting point for the future search for an electric dipole moment of a charged particle. As it was said in the previous chapter, the RF Wien filter was installed in the storage ring. Number of simulations were done to set the experimental limit for the existing ring, i.e. with the level of misalignments and the phase stability that are present at COSY. Clockwise and counter-clockwise technique is not applicable in this case, since there is no availability to store the beam in CCW direction at this machine. A simulation for the maximization of the spin coherence time hasn't been performed for RF Wien filter method, but the experimental data was gathered during the test runs at COSY. The spin coherence time has been achieved of around 1000 s [48]. For this purpose, the sextupole correction together with the beam cooling were used. The measured spin coherence time is shown in Figure 90.

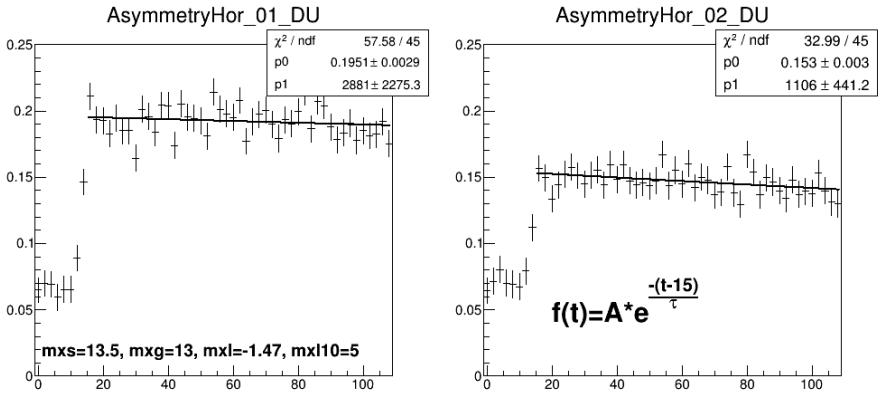

Figure 90: Spin coherence time for two spin states (up and down) at the test run at COSY.

Two spin states with vertical polarization in the up or down direction are displayed in the picture. The extraction time, when the measurement

of the spin polarization was done, was set to approximately one hundred seconds. The function

$$F(t) = A \cdot \exp(\frac{-(t-15)}{t}) \tag{6.2.1}$$

was used to fit the data points and calculate the SCT for both states. The coefficient p_1 indicates the value for the spin coherence time. The SCTs are different for two states because the initial polarization was different.

Taking into account that the SCT is sufficient for the detection of an EDM signal, the simulations have been made for a single particle.

Misalignments of the Wien filter

The ideal storage ring was discussed in the previous chapter and the linear build-up of the vertical polarization corresponding to the interaction of an EDM with the motional electric field inside the ring was demonstrated. Firstly, one should consider the case when the RF Wien filter is not ideally set. The situation with the slightly rotated device will be investigated. The Wien filter field strength was set to $E = 1\,\mathrm{MV/m}$, B-field was equal to $0.73\,\mathrm{T}$ and the length was chosen of $1\,\mathrm{m}$.

The rotation of the RF Wien filter around the longitudinal axis yields a horizontal component of the magnetic field B_x, which, in turn, causes the vertical betatron oscillations of the beam. The spin receives an additional kick due to the MDM interaction with B_x according to Thomas-BMT equation. This kick works in the same way as an EDM interaction with the motional electric field in the ring (see Figure 91). It is clearly visible that the rotation of the device leads to the same amount of the polarization build-up, which could be produced by the EDM of the order of $10^{-19}\,e \cdot \mathrm{cm}$. The build-up of the polarization per turn scales linearly with the value of the angle of the RF Wien filter rotation, as well as the false EDM signal, which this rotation generates. The spin experiences fast (g-2) precession, which are modulated by the RF Wien filter. That is why one sees two broad bands in Figure 91, and not a single line. The width of the bands is proportional to the value of the EDM. In the following simulation η that is equal to 10^{-4} will be used, which corresponds to the EDM of $2.6 \cdot 10^{-19}\,e \cdot \mathrm{cm}$. The Wien filter was rotated by a random angle drawn from the normal distribution with the mean $\mu = 0$ and the standard deviation $\sigma = 10^{-4}$. This is the typical precision of placement for a device at COSY.

The MDM rotation that mimics the EDM signal is directly proportional to the angle of the RF Wien filter rotation. If one sets the device more accurately, the rate of the MDM rotation drops. With this field strength of the Wien filter the EDM polarization build-up per turn is of the order of $S_y = 10^{-7}$ and the MDM one is of the same order of magnitude. Figure 92 demonstrates the linear dependence of the MDM build-up per turn on the order of the RF Wien filter rotation angle.

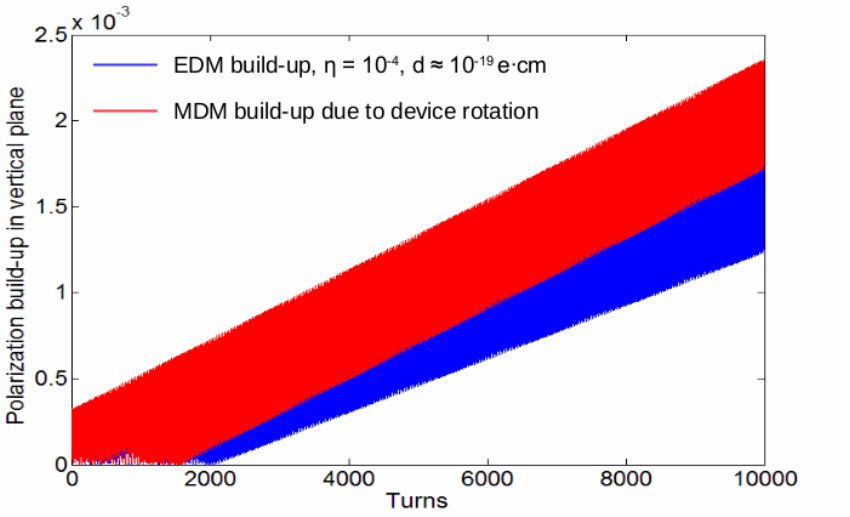

Figure 91: The polarization build-up in vertical plane. The initial spin direction of the deuteron is longitudinal. In red: the MDM interaction with the field of the longitudinally rotated Wien filter in the absence of the EDM. The rotation angle is 10^{-4} rad. In blue: the EDM interaction with the motional electric field, when the Wien filter is perfectly aligned. The EDM of $2.6 \cdot 10^{-19}\, e \cdot \mathrm{cm}$ was assumed.

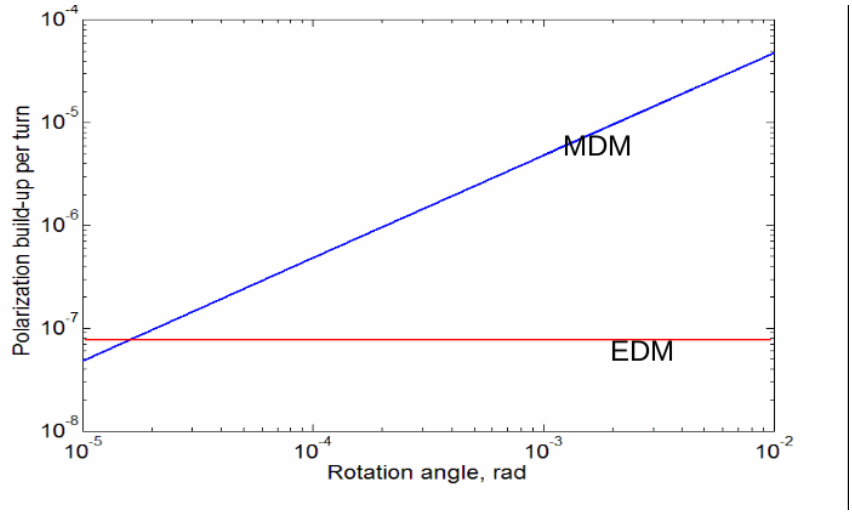

Figure 92: The polarization build-up per turn for different angles of the RF Wien filter rotation. In red: the EDM build-up per turn for the ideal ring. In blue: the MDM build-up per turn. The EDM of $2.6 \cdot 10^{-19}\, e \cdot \mathrm{cm}$ was assumed.

Misalignments of the ring elements

The next step one should take, is to consider the effect of the non-vanishing misalignments of the magnets in the machine. The presence of the misalignments tilts the initially vertical direction of the spin closed orbit. This induces a similar false build-up of the polarization, which was described above. The present misalignments at COSY are of the order of 0.1 mm (or mrad for rotations). They were randomly distributed in the MODE program. The typical random seed coincides with the result, which is shown in Figure 93. There was no orbit correction made during the simulation.

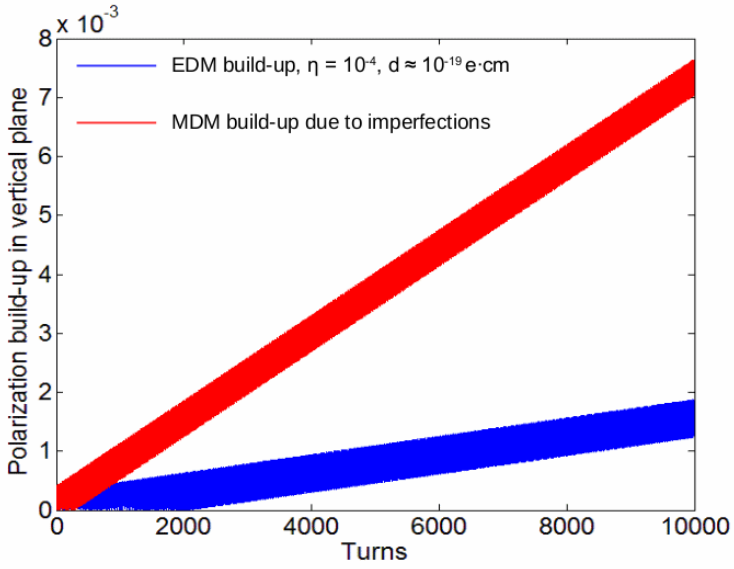

Figure 93: The polarization build-up in vertical plane. The initial spin direction of the deuteron is longitudinal. In red: The polarization build-up due to the MDM interaction with imperfection fields of the misaligned magnets with RF Wien filter on. In blue: the EDM interaction with the motional electric field in the absence of imperfections. The EDM was $2.6 \cdot 10^{-19}\, e \cdot \mathrm{cm}$.

Frequency mismatch

As it was mentioned above, the RF Wien filter must be operated exactly at the spin resonance. What happens, if there is a mismatch between the operating and the resonance frequencies? One can denote this mismatch by

$$\Delta = \frac{f_{WF}}{f_{res}}, \tag{6.2.2}$$

where f_{WF} and f_{res} are the operating Wien filter and the spin resonance frequencies respectively. An EDM of $10^{-21}\, e \cdot \mathrm{cm}$ was used in the simu-

lation. Four different mismatches were considered with the largest one of 10^{-4} and the smallest one of 10^{-7}. Here η parameter was set two orders of magnitude lower and was equal to 10^{-6}. The resulting polarization build-ups are plotted in Figure 94.

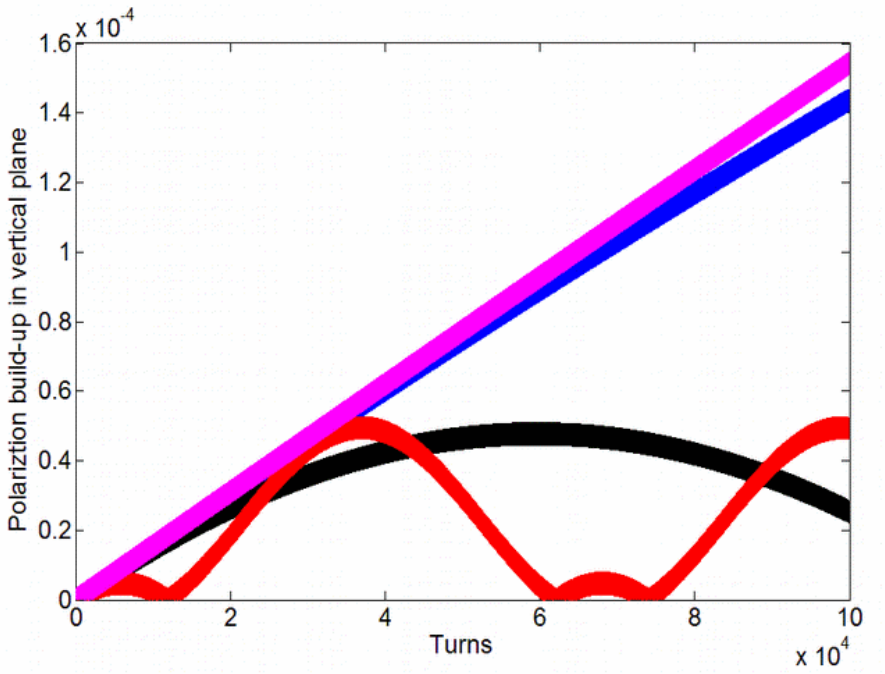

Figure 94: The polarization build-ups due to the EDM interaction with the motional electric field for different values of the mismatch between the spin resonance and the operating Wien filter frequencies. a) $\Delta = 10^{-7}$ b) $\Delta = 10^{-6}$, c) $\Delta = 10^{-5}$, d) $\Delta = 10^{-4}$. An EDM was equal to $2.6 \cdot 10^{-21}\, e \cdot \mathrm{cm}$.

One can see that the polarization does not grow linearly anymore, when two frequencies do not match, but indeed oscillates. The resonance condition must be fulfilled with the great precision. In the case, when $\Delta = 10^{-7}$ the slope of the polarization build-up coincides with the theoretically calculated value. This indicates that one should set the frequency of the RF Wien filter with the precision of 10^{-7} for the EDM of $10^{-21}\, e \cdot \mathrm{cm}$. However, that constraint also scales linearly with the value of the EDM, and for the EDM of the order of $10^{-20}\, e \cdot \mathrm{cm}$ one can afford to have a mismatch at the level of 10^{-6}.

Conclusion

One of the possible ways to measure an EDM at the precursor experiment at COSY was considered. The representation of the RF Wien filter was realized in MODE program. The systematic effects, which limit the potential sensitivity, were studied.

The impact of the rotations of the Wien filter was investigated. Firstly, the EDM-like signal was generated by the MDM interaction with the rotated vertical magnetic field of the Wien filter. Secondly, the situation with the pure EDM build-up for the untitled device was considered. It was shown that the rotations of the RF Wien filter around the longitudinal axis yields the same build-up of the vertical polarization as caused by the EDM interaction with the motional electric field in COSY ring.

The spin motion was examined when the misalignments and rotations of the magnets of COSY took place. Two types of tracking were performed for that reason, one with the EDM and a perfect orbit and another without one for the distorted case. The build-ups of polarization were plotted against the turn number for both situations and later compared in order to get the systematic limit on the current COSY configuration.

The mismatch between the operating frequency of the RF Wien filter and the spin resonance frequency was considered. Four particular situations with different relative frequency mismatches were tested in the simulation. The resulting polarization build-ups were compared. The deviation from linear behavior, which prevents the possibility of polarization measurements, was demonstrated. It was presented that one must pay significant attention to the fulfillment of the resonance condition.

In summary, all three simulation results indicate the same systematic limit, for the present situation at COSY, of the order of $10^{-19}\, e \cdot \mathrm{cm}$. This is a starting point for the precursor experiment that is planned to be conducted in the next 2 years. Based on this, one should think of an installation of a modern orbit correction system and on a way to control and keep the frequency of the RF Wien filter with the maximum achievable precision. Further simulation work will be done towards the implementation of an orbit correction algorithm in MODE program. Field errors of the Wien filter must be considered and the effect caused by them should be calculated.

7

CONCLUSIONS AND OUTLOOK

The interest for electric dipole moment (EDM) experiments is highly motivated by the problem of matter-antimatter asymmetry in our Universe. New sources of CP violation are needed to explain that phenomenon properly. An EDM of an elementary particle is a perfect candidate for this role because the existence of an EDM requires CP-violation. In particular, new experiments for the EDM of a charged hadron are proposed.

The upcoming experiment requires a new storage ring to be built. Since an EDM could be as small as $10^{-29}\, e \cdot \mathrm{cm}$, a fantastic precision should be achieved. The main obstacle on the way is systematic errors, which set the final limitation on the accuracy that can be accomplished. The systematic errors for three measurement principles were investigated in this work.

To study the impact of the systematic errors on the final experimental sensitivity, a large number of simulations were made. The newly developed program MODE was the primary simulation tool. The basic working principle of MODE was explained. The models of the future experiments for the frozen and the quasi-frozen spin methods were designed and realized in MODE environment. Special ring elements with incorporated magnetic and electric fields were created and used in the simulations. The time depended element, the radio frequency Wien filter, was programmed, too, for the consideration of the precursor experiment.

MODE was benchmarked via the comparison with the existing experimental data, which was taken during the test runs at the Cooler Synchrotron (COSY). The ring structure for the precursor experiment at COSY was written. The model of COSY storage ring was precisely tested. The spin-orbital dynamics is correctly described in the program. Furthermore, the comparison of the simulation results between COSY-infinity and MODE codes was made, and the obtained outcomes were similar.

After the program testing and its benchmarking the main systematic studies were done. Two approaches - the frozen and the quasi-frozen spin methods - are close in realization and they share the same systematics. The precursor experiment, where a radio frequency Wien filter is implemented, has at least one more source of systematic errors, which corresponds to the accuracy and the stability of the RF Wien filter frequency.

The first reason of the potential errors is the spin decoherence, which takes place at any storage ring when a bunch of polarized particles is used. The finite size of the bunch in all three directions: radial, vertical and longitudinal causes the particles' spins to decohere (depolarize) while the bunch is stored.

The second main source of the arising errors is the misalignment of the elements inside the ring. Each accelerator has a finite precision of the magnet installation. Any rotations of the main dipoles or combined E/B elements inevitably lead to the build-up of the fake signal, which mimics the EDM contribution.

For the Wien filter approach, the frequency mismatch between the Wien filter device and the frequency of the spin rotation is harmful. The EDM polarization build-up is impossible if the ratio between those two frequencies is not maintained equal to one.

The ways of the correction for the main systematic errors were described. The spin decoherence effects should be fought by implementation of an radio frequency cavity with high voltage and frequency to compensate the $\frac{\Delta p}{p}$ part leading to the depolarization. The terms connected to the beam sizes in radial and vertical directions must be compensated by sextupole fields.

The misalignments of the main dipoles or the E/B elements can only be corrected if one stores the beams in opposite directions. So subtraction of the signals from clockwise and counter-clockwise runs will allow to disentangle an EDM contribution from systematic effects.

The promising field calibration technique was proposed. This approach requires further simulations to be proven undoubtedly valid. However, even today one can consider it a simple and useful way of getting access to precise measurements of vertical fields for CW and CCW experimental setups.

The sensitivity for the future potential experiments with either the frozen or the quasi-frozen spin were estimated. With the current possibility of determination of spin precession frequency at the level of $10^{-6}\,\mathrm{Hz}$ for 1000 seconds, the EDM limit, which one can currently set on those methods, is of the order of $10^{-25} \div 10^{-26}\, e\ \cdot \mathrm{cm}$. For the present situation at COSY, the accuracy of the precursor experiment is expected to be of the order of $10^{-19} e \cdot \mathrm{cm}$.

The future improvement of the spin precession frequency determination technique will increase the potential sensitivity of the EDM experiments. The steps must be made exactly in this direction. The alignment process must be advanced, too. Further studies of additional systematic errors, which has fewer impact on the final precision, should be made.

BIBLIOGRAPHY

[1] Aaij R., Abellan Beteta C., Adeva B. et al. (2012). "Evidence for CP Violation in Time-Integrated $D_0 \to h^- h^+$ Decay Rates", *Phys. Rev. Lett.*, 108, 111602.

[2] Abachi S., Abbott B., Abolins M. et al. (1995). "Search for High Mass Top Quark Production in $p\bar{p}$ Collisions at $\sqrt{s} = 1.8\,\mathrm{TeV}$", *Phys. Rev. Lett.*, 74, 2422 – 2426.

[3] Abe F., Akimoto H., Akopian A. et al. (1995). "Observation of Top Quark Production in $p\bar{p}$ Collisions with the Collider Detector at Fermilab", *Phys. Rev. Lett.*, 74, 2626 – 2631.

[4] Abe K., Abe K., Abe R. et al. (2001). "Observation of Large CP Violation in the Neutral B Meson System", *Phys. Rev. Lett.*, 87, 091802.

[5] Abe K., Hayato Y., Iida T. et al. (2011). "The search for n-nbar oscillation in Super-Kamiokande I", *ArXiv e-prints*. Retrieved from http://arxiv.org/abs/1109.4227.

[6] Aguilar M., Alberti G., Alpat B. et al. (2013). "First Result from the Alpha Magnetic Spectrometer on the International Space Station: Precision Measurement of the Positron Fraction in Primary Cosmic Rays of $0.5 - 350\,\mathrm{GeV}$", *Phys. Rev. Lett.*, 110, 141102.

[7] Altarev I., Chesnevskaya S., Feldmeier W. et al. (2012). "A next generation measurement of the electric dipole moment of the neutron at the FRM II", *Il Nuovo Cimento*, 35.

[8] Anastassopoulos D. et al. (2008). "Search for a permanent electric dipole moment of the deuteron nucleus at the $10^{-29} e \cdot \mathrm{cm}$ level", *AGS proposal (srEDM collaboration*.

[9] Andrianov S. (2006). "Normal form for beam physics in matrix presentation", *Proceedings of EPAC*2006, 2122 – 2124.

[10] Andrianov S. (1993). "A matrix representation of the lie transformation", *Abstracts of the Intern. Congress on Comp. Syst. and Appl. Math CSAM*, 14.

[11] Andrianov S. (1995). "Dynamic modeling in beam dynamics",*Proc. of the 2 Intern. Workshop on Beam Dynamics and Optimiz.*, 20 – 28.

[12] Andrianov S. (1997). "A matrix representation of the lie algebraic methods for design of nonlinear beam lines", *AIP Conf. Proc*, 391, 335 – 360.

[13] Andrianov S. (2004). "Role of parallel and distributed computing in beam physics", *Nuclear Instruments and Methods*, 519, 37 – 41.

[14] Andrianov S. (2012). "The convergence and accuracy of the matrix formalism approximation", *Proc. of ICAP*2012, 93 – 95.

[15] Apostol. T. (1974). "Mathematical Analysis", *Addison-Wesley*.

[16] Aubert B., Boutigny D., Gaillard J.-M. et al. (2001). "Observation of CP Violation in the B^0 Meson System", *Phys. Rev. Lett.*, 87, 091801.

[17] Aubry A., Chartier P. (1998). "Pseudo-symplectic runge-kutta methods", *BIT Numerical Mathematics*, 38, 439 – 461.

[18] Bagdasarian Z. et al. (2014). "Measuring the polarization of a rapidly precessing deuteron beam", *Phys. Rev. ST Accel. Beams*, 17, 052803.

[19] Baker C. A., Doyle D. D., Geltenbort P. et al. (2006). "Improved Experimental Limit on the Electric Dipole Moment of the Neutron", *Phys. Rev. Lett.*, 97, 131801.

[20] Bargmann V., Michel L., Telegdi V.L. (1959). "Precession of the Polarization of Particles Moving in a Homogeneous Electromagnetic Field", *Phys. Rev. Lett.*, 2, 435.

[21] Becker-Szendy R., Bratton C. B., Cady D. R. et al. (1990). "Search for proton decay into $e^+ + \pi^0$ in the IMB-3 detector", *Phys. Rev. D*, 42, 2974 – 2976.

[22] Bennett G. W., Bousquet B., Brown H. N. et. al. (2009). "Improved limit on the muon electric dipole moment", *Phys. Rev. D*, 80, 052008.

[23] Berz M. (1989). "Differential algebraic description of beam dynamics to very high orders", *Particle Accelerators*, 24, 109 – 124.

[24] Berz M., Makino K. (2013). "COSY INFINITY 9.1: Beam Physics Manual", *Tech.report of Michigan State University*, MSUHEP-060804-rev.

[25] Berz M. (1991). "Symplectic Tracking Through Circular Accelerators With High Order Maps", *Nonlinear Problems in Future Accelerators*, eds. W. Scandale and G. Turchetti, 288 – 296.

[26] Berz M. (1990). "Computational Aspects of Optics Design and Simulation: COSY INFINITY", *Nuclear Instruments and Methods in Physics Research Section A: Accelerators, Spectrometers, Detectors and Associated Equipment*, 298, 473 – 479.

[27] Bogolyubov N., Mitropolsky Yu. (1961). "Asymptotic methods in the theory of nonlinear oscillations", *Hindustan Publishing Corpn. Delhi*.

[28] Canetti L., Drewes M., Shaposhnikov M. (2012). "Matter and Antimatter in the Universe", *New Journal of Physics*, 14, 095012.

[29] Chatrchyan S., Khachatryan V., Sirunyan A. et al. (2001). "Observation of a new boson at a mass of 125 GeV with the CMS experiment at the LHC", *Physics Letters B.*, 716, 30 – 61.

[30] Chekmenev S. (2014). "Estimation of Systematic Errors for Deuteron Electric Dipole Moment (EDM) Search at a Storage Ring", *Proc. of IPAC*2014, 2998.

[31] Chekmenev S. (2016). "Estimation of Systematic Errors for Deuteron Electric Dipole Moment Search at COSY", *International Journal of Modern Physics: Conference Series*, 40, 1660099.

[32] Christenson J., Cronin J., Fitch V. et al. (1964). "Evidence for the 2Π Decay of the K_2^0 Meson", *Physical Review Letters*, 13, 138 – 140.

[33] Courant E., Snyder H. (1958). "Theory of the Alternating-Gradient Synchrotron", *Annals of Physics*, 3.

[34] Dimopoulos S., Georgi H. (1981). "Softly broken supersymmetry and SU(5)", *Nuclear Physics B*, 193, 150 – 162.

[35] Dmitriev V. F., Sen'kov R. A. (2003). "Schiff Moment of the Mercury Nucleus and the Proton Dipole Moment", *Phys. Rev. Lett.*, 91, 212303.

[36] Dragt A. (1997). "Lie Methods for Nonlinear Dynamics with Applications to Accelerator Physics", *University of Maryland, Center for Theoretical Physics, Department of Physics*.

[37] Dragt A., Healy L., Neri F. (1985). "MARYLIE 3.0. A Program for nonlinear analysis of accelerator and beamline lattices", *IEEE Trans. Nucl. Sci.*, 32, 2311 – 2313.

[38] Eversmann D. et al. (2015). "New Method for a Continuous Determination of the Spin Tune in Storage Rings and Implications for Precision Experiments", *Phys. Rev. Lett.*, 115, 094801.

[39] Fanti V., Lai A., Marras D. et al. (1999). "A New measurement of direct CP violation in two pion decays of the neutral kaon", *Phys.Lett.*, B465, 335 – 348.

[40] Farley F.J.N. (1972), "Pitch correction in (g-2) experiments", *Phys. Lett.*, 42B, 66 – 68.

[41] Farley F. J. M., Jungmann K., Miller J. P. et al. (2004). "New Method of Measuring Electric Dipole Moments in Storage Rings", *Phys. Rev. Lett.*, 93, 052001.

[42] Farrar G. R., Shaposhnikov M. E. (1993). "Baryon asymmetry of the Universe in the minimal standard model", *Phys. Rev. Lett.*, 70, 2833 – 2836.

[43] Fixsen D., Dwek E., Mather J. C. et al. (1998). "The Spectrum of the Extragalactic Far-Infrared Background from the COBE FIRAS Observations", *The Astrophysical Journal*, 508, 123.

[44] Fournier D. (1990). "NA31 results on CP violation in K decays, and a test of CPT", 1989 *International Symposium on Lepton-photon Interactions at High Energies.*, 168 – 183.

[45] Fukuyama T., Silenko A.J. (2013). "Derivation of Generalized Thomas-Bargmann-Michel-Telegdi Equation for a Particle with Electric Dipole Moment", *Int. J. Mod. Phys.*, *A*28, 1350147.

[46] Gilani F. (2004). "C# In-Depth: Harness the Features of C# to Power Your Scientific Computing Projects", *MSDN Magazine*. Retrieved from http://msdn.microsoft.com/en-us/magazine/cc163995.aspx

[47] Grote H. (1990). "The MAD program (methodical accelerator design) version 8.4: User's reference manual". Retrieved from http://mad8.web.cern.ch/mad8/doc/mad8_user.pdf.

[48] Guidoboni G. (2013). "Spin Coherence Time studies for the storage ring EDM search", *PhD Thesis*.

[49] Hinshaw G., Larson D., Komatsu E. et al. (2013). "Nine-year Wilkinson Microwave Anisotropy Probe (WMAP) Observations: Cosmological Parameter Results", *The Astrophysical Journal Supplement Series*, 208, 19.

[50] Ignatovich V.K. (2007). "The Berry phase. The simplest derivation and relation to EDM experiments with UCN", *American Journal of Physics*, 76, 258 – 264.

[51] Ivanov A. (2014). "MODE software for nonlinear spin-orbit dynamics simulation in electromagnetic fields", *Proc. of 20 Intern. Workshop on BDO*.

[52] Ivanov A. et al. (2014). "Matrix Integration of ODEs for Spin-orbit Dynamics Simulation", *Proc. of IPAC*2014*, Dresden, Germany*, 400 – 402.

[53] Jackson J. (1998). "Classical Electrodynamics, 3rd Edition", *Wiley-VCH*.

[54] Kaplansky I. (1969). "Linear Algebra and Geometry: A second course", *Dover Publications, Inc.*.

[55] Khriplovich I. (2000). "Nuclear electric dipole moments at ion storage rings", *Hyperfine Interactions*, 127, 365 – 371.

[56] Knecht A. (2009). "Towards a New Measurement of the Neutron Electric Dipole Moment". Retrieved from http://ucn.web.psi.ch/papers/Thesis_Andreas_Knecht_2009.pdf.

[57] Kobayashi M., Maskawa T. (1973). "CP-Violation in the Renormalizable Theory of Weak Interaction", *Progress of Theoretical Physics.*, 49, 652 – 657.

[58] Kodama K., Ushida N., Andreopoulos C. et al. (2001). "Observation of tau neutrino interactions", *Physics Letters B.*, 504, 218 – 224.

[59] Lambert J.D. (1991). "Numerical Methods for Ordinary Differential Systems. The Initial Value Problem", *John Wiley & Sons*.

[60] Landau L., Lifshitz E. (1969). "Mechanics", *Pergamon Press*.

[61] Lebedev V. Retreived from http://home.fnal.gov/∼ostiguy/ OptiM/OptimHelp/optimx.html.

[62] Lee S. (1997). "Spin Dynamics and Snakes in Synchrotrons", *Singapore: World Scientific*.

[63] Lehrach A., Pretz J., Rathmann F. et al. (2014). "Search for Permanent Electric Dipole Moments at COSY. Step 1: Spin coherence and systematic error studies".

[64] Lehrach A., Lorentz B., Morse W. et al. (2012). "Precursor Experiments to Search for Permanent Electric Dipole Moments (EDMs) of Protons and Deuterons at COSY", *ArXiv:1201.5773.*

[65] Livingston S., Blewett J. (1962). "Particle Accelerators", *McGraw-Hill Book Company, Inc.*

[66] Luke S. (2015). "Essentials of Metaheuristics", *Lulu*. Retrieved from https://cs.gmu.edu/∼sean/book/metaheuristics/Essentials.pdf.

[67] Lüders G. (1954). "On the Equivalence of Invariance under Time-Reversal and under Particle-Antiparticle Conjugation for Relativistic Field Theories", *Kongelige Danske Videnskabernes Selskab, Matematisk-Fysiske Meddelelser.*, 28, 1 – 17.

[68] Maier R. (1997). "Cooler synchrotron COSY – Performance and perspectives", *Nuclear Instruments and Methods in Physics Research Section A: Accelerators, Spectrometers, Detectors and Associated Equipment*, 390, 1 – 8.

[69] Mane S. (2008). "Orbital dynamics in a storage ring with electrostatic bending", *Nuclear Instr. and Methods in Phys. Research A*, 288 – 294.

[70] Mane S. (2012). "Orbital and spin motion in a storage ring with static electric and magnetic fields", *Nuclear Instr. and Methods in Phys. Research A*, 40 – 50.

[71] Matlab – the language of technical computing. Retrived from http://www.matlab.com.

[72] Mey S., Gebel R. (2016). "A Novel RF E×B Spin Manipulator at COSY", *International Journal of Modern Physics: Conference Series*, 40, 1660094.

[73] Meyer H. O., Schwandt P., Jacobs W. W. et al. (1983). "Proton scattering from ^{12}C between 120 and 200 MeV and the optical potential", *Phys. Rev. C*, 27, 459 – 469.

[74] Mohapatra R. N., Pati J. C. (1975). ""Natural" left-right symmetry", *Phys. Rev. D*, 11, 2558 – 2561.

[75] Nishino H., Clark S., Abe K. et al. (2009). "Search for Proton Decay via $p \to e^+\pi^0$ and $p \to \mu^+\pi^0$ in a Large Water Cherenkov Detector", *Phys. Rev. Lett.*, 102, 141801

[76] Pati J. C., Salam A. (1974). "Lepton number as the fourth "color"", *Phys. Rev. D*, 10, 275 – 289.

[77] Pauli W. (1955). "Exclusion principle, Lorentz group and reflexion of space-time and charge" in Pauli W., Rosenfeld L., Weisskopf V. (Eds) *"Niels Bohr and the development of physics; essays dedicated to Niels Bohr on the occasion of his seventieth birthday"*, London : Pergamon Press.

[78] Picozza P., Boezio M. (2013). "Picozza P., Boezio M. Multi messenger astronomy and CTA: TeV cosmic rays and electrons", *Astroparticle Physics*, 43, 163 – 170.

[79] Pospelov M., Ritz A. (2005). "Electric dipole moments as probes of new physics", *Annals of Physics*, 318, 119 – 169.

[80] Retrieved from http://physics.nist.gov/cgi-bin/cuu/Value?gdn

[81] Rosenzweig J. (2003). "Fundamentals of beam physics", *New York: Oxford University Press*, 291.

[82] Sakharov A. (1967). "Violation of CP Invariance, C Asymmetry, and Baryon Asymmetry of the Universe", *Letters to Jounal of Experimental and Theoretical Physics*, 5, 24 – 26.

[83] Semertzidis Y. (2011). "A storage ring proton electric dipole moment experiment: most sensitive experiment to cp-violation beyond the standard model", *Proceedings of the DPF-2011 Conference, Providence, RI*. Retrieved from http://arxiv.org/pdf/1110.3378v1.pdf

[84] Senichev Yu., Lehrach A., Maier R., Zyuzin D. (2011). "The spin aberration of polarized beam in electrostatic rings", *P*roc. of IPAC2011, 2175 – 2178.

[85] Senichev Yu., Maier R., Zyuzin D. (2013). "Spin Tune Decoherence Effects in Electro- and Magnetostatic Structures", *Proc. of IPAC13*, 2579 – 2581.

[86] Senichev Yu., Andrianov. S, Ivanov A., Chekmenev S. Berz M., Valetov E. (2015). "Investigation of Lattice for Deuteron EDM Ring", *Proc. of ICAP*2015, 17 – 19.

[87] Senichev Yu., Andrianov. S, Ivanov A., Chekmenev S. Berz M., Valetov E. (2015). "Quasi-frozen Spin Method for EDM Deuteron Search", *Proc. of IPAC*2015, 213 – 215.

[88] Senichev Yu., Ivanov A., Lehrach A., Maier R., Zyuzin D., (2014). "Spin Tune Decoherence in Multipole Fields", *Proc. of IPAC*2014, 3017 – 3019.

[89] Senichev. Yu., Møller S.P. (2000). "Beam Dynamics in Electrostatic Rings", *Proceedings of EPAC*2000, 794 – 796.

[90] Senichev Yu., Lehrach A., Maier R., Zyuzin D. (2011). "The spin aberration of polarized beam in electrostatic rings", *Proceedings of IPAC*2011, 2175 – 2177.

[91] Senichev Yu. (2000). "The features of beam dynamics in the electrostatic rings", *FZJ IKP report*, 23.

[92] Senichev Yu., Andrianov. S, Ivanov A., Chekmenev S. Berz M., Valetov E., Pretz. J., Lorentz B. (2016). "Systematic Errors Investigation in Frozen and Quasi-Frozen Spin Lattices of Deuteron EDM Ring", *Proceedings of IPAC*2016.

[93] Serebrov A., Aleksandrov E., Dovator N. et al. (2008). "Experimental search for neutron: Mirror neutron oscillations using storage of ultracold neutrons", *Phys. Lett.*, B663, 191 – 185

[94] Smith J. H., Purcell E. M., Ramsey N. F. (1957). "Experimental Limit to the Electric Dipole Moment of the Neutron", *Phys. Rev.*, 108, 120 – 122.

[95] Storage Ring EDM Collaboration (2011). "A Proposal to Measure the Proton Electric Dipole Moment with $10^{-29} e \cdot \mathrm{cm}$ Sensitivity".

[96] Tarbutt M. R., Sauer B. E., Hudson J. J. et al. (2013). "Design for a fountain of YbF molecules to measure the electron's electric dipole moment", *New Journal of Physics*, 15, 053034.

[97] The ACME Collaboration (2014). "Order of Magnitude Smaller Limit on the Electric Dipole Moment of the Electron", *Science*, 343, 269 – 272.

[98] Weinberg S. (1976). "Implications of dynamical symmetry breaking", *Phys. Rev.*, 13, 974 – 976.

[99] Wess J., Zumino B. (1974). "Supergauge transformations in four dimensions", *Nuclear Physics B*, 70, 39 – 50.

[100] Wille K. (2001). "Particle Accelerator Physics: An Introduction", *Oxford University Press*.

[101] Zhang H., Ding F. (2013). "On the Kronecker Products and Their Applications", *Journal of Applied Mathematics*, 2013, 296185.

[102] Алферов Г. (2006). "Механика в криволинейных координатах". [Alferov G. (2006). "Mechanics in curvilinear coordinates"]. Retrieved from http://www.apmath.spbu.

[103] Андрианов С. (2004). "Динамическое моделирование систем управления пучками частиц *СПб.: Изд-во С.-Петерб. ун-та,* [Andrianov S. (2004). "Dynamic modelling of beam particle control systems", *SPbSU*].

[104] Егоров А. (2005). "Обыкновенные дифференциальные уравнения с приложениями *М.: ФИЗМАТЛИТ.* [Egorov A. (2005). "Ordinary differential equations with applications", *M.: PHYSMATHLIT*].

[105] Иванов А. (2015). "Нелинейное матричное интегрирование спин-орбитальной динамики заряженных частиц" [Ivanov A. (2015). "Nonlinear matrix integration of spin-orbital dynamics of charged particles", *PhD Thesis*]. ru/ru/staff/alferov/files/krivol_coordinaty.pdf

[106] Лоусон Д. (1980). "Физика пучков заряженных частиц *М. Мир* [Lawson D. (1980). "The Physics of Charged Particle Beams", *M. Mir*].

[107] Штеффен К. (1960). "Оптика пучков высокой энергии *М. Мир* [Steffen K. (1969). "High Energy Beam Optics", *M. Mir*].

[108] Силадьи М. (1990). "Электронная и ионная оптика *М. Мир* [Szilágyi M. (1990). "Electron and Ion Optics", *M. Mir*].

8

APPENDIX

APPENDIX A

One can consider the case when quadrupole but sextupole fields are present in the ring, Hill's differential equations [100] for the orbital motion will be

$$\begin{aligned} x'' + \frac{K(s)}{1+\delta}x + \frac{1}{2}\frac{S(s)}{1+\delta}(x^2 - y^2) &= \frac{1}{\rho(s)}\frac{\delta}{1+\delta} \\ y'' - \frac{K(s)}{1+\delta}y - \frac{S(s)}{1+\delta}xy &= 0, \end{aligned} \tag{8.1.1}$$

where $x'' = \frac{d^x}{ds^2}$, $y'' = \frac{d^y}{ds^2}$, $K(s) = \frac{e}{p}\frac{\partial B_y(s)}{\partial x}$ and $S(s) = \frac{e}{p}\frac{\partial B_y^2(s)}{\partial x}$ are the quadrupole and the sextupole components in the ring correspondingly. Since one has to avoid hitting the third order resonance [62], the average value for S can be used $\bar{S} = \frac{1}{2\pi R}\sum_i S_i l_i$. The new variables can be introduced via Courant-Snyder formalism [33]

$$\begin{aligned} \eta_x &= \frac{x}{\sqrt{\beta_x}} \\ \eta_y &= \frac{y}{\sqrt{\beta_y}} \\ \beta_{x,y}\nu_{0_{x,y}}d\phi &= ds, \end{aligned} \tag{8.1.2}$$

where $\beta_{x,y}$ are the horizontal and the vertical β-functions and $\nu_{0_{x,y}}$ are the corresponding betatron tunes.

The new variable ϕ is periodic with 2π around circumference of the ring $C = 2\pi\bar{R}$. When $\delta << 1$ is assumed, the following system of equations can be defined

$$\begin{aligned} \eta_x'' + \nu_{0_x}^2(1-\delta)\eta_x = -\frac{1}{2}S\nu_{0_x}^2(1-\delta)\beta_x^{3/2}(\beta_x\eta_x^2 - \beta_y\eta_y^2) + \\ +\nu_{0_x}^2(1-\delta)\beta_x^{3/2}\frac{\delta}{\rho} \\ \eta_y'' + \nu_{0_y}^2(1-\delta)\eta_y = S\nu_{0_y}^2(1-\delta)\beta_y^{3/2}\beta_x^{1/2}\eta_x\beta_y^{1/2}\eta_y \end{aligned} \tag{8.1.3}$$

For the simplicity, introduction of new coordinates $d\theta_{x,y} = \omega_{x,y} d\phi$ that will be used in equation 8.1.3 with the coefficients is needed

$$\begin{aligned} \bar{\omega}_{0_x}^2 &= \nu_{0_x}^2 (1-\delta) \\ \bar{\omega}_{0_y}^2 &= \nu_{0_y}^2 (1-\delta) \\ A &= \frac{1}{2} \bar{\omega}_{0_x}^2 S \beta_x^{3/2} \\ B &= \bar{\omega}_{0_y}^2 S \beta_y^{3/2} \\ C_\delta &= \frac{\bar{\omega}_{0_x}^2}{\rho} \beta_x^{3/2}. \end{aligned} \tag{8.1.4}$$

The equation 8.1.3 can be written as

$$\begin{aligned} \omega_x^2 \eta_x'' + \bar{\omega}_{0_x}^2 \eta_x &= -A(\beta_x \eta_x^2 - \beta_y \eta_y^2) + C_\delta \delta \\ \omega_y^2 \eta_y'' + \bar{\omega}_{0_y}^2 \eta_y &= B \beta_x^{1/2} \beta_y^{1/2} \eta_x \eta_y \end{aligned} \tag{8.1.5}$$

The sextupole term brings small contribution to the solution, so it can be considered as a tiny perturbation of motion. The solution can be found with the help of Landau method [60]

$$\begin{aligned} \eta_{x,y} &= \eta_{0_x} + \eta_{1_x} + \eta_{2_x} + ... \\ \omega_{x,y} &= \omega_{0_x} + \omega_{1_x} + \omega_{2_x} + ... \end{aligned} \tag{8.1.6}$$

When this approach is completed, it's possible to get the following formulas for η and ω for zero order

$$\begin{aligned} \eta_{0_x} &= \sqrt{\epsilon_x} \cos\theta_x + \frac{C_\delta \cdot \delta}{\bar{\omega}_{0_x}^2} \\ \omega_{0_x} &= \bar{\omega}_{0_x} \eta_{0_y} = \sqrt{\epsilon_y} \cos\theta_y \omega_{0_y} = \bar{\omega}_{0_y} \end{aligned} \tag{8.1.7}$$

and for the first order

$$\begin{aligned} \eta_{1_x} = &-\frac{A}{\bar{\omega}_{0_x}^2} \left(\frac{\beta_x \epsilon_x}{2} - \frac{\beta_y \epsilon_y}{2} \right) - \frac{A \beta_x}{\bar{\omega}_{0_x}^2} \left(\frac{C_\delta \delta}{\bar{\omega}_{0_x}^2} \right)^2 + \\ &+ \frac{A}{\bar{\omega}_{0_x}^2} \left(\frac{\beta_x \epsilon_x}{6} \cos 2\theta_x + \frac{\beta_y \epsilon_y}{2(1 - 4\bar{\omega}_{0_y}^2 / \bar{\omega}_{0_x}^2)} \right) \cos 2\theta_y \Bigg) \\ \eta_{1_y} = &\frac{B}{\bar{\omega}_{0_y}^2} \sqrt{\epsilon_x \beta_x} \sqrt{\epsilon_y \beta_y} \Bigg(\frac{\cos(\theta_y - \theta_x)}{2[1 - (\bar{\omega}_{0_y} - \bar{\omega}_{0_x})^2 / \bar{\omega}_{0_y}^2]} + \\ &+ \frac{\cos(\theta_y + \theta_x)}{2[1 - (\bar{\omega}_{0_y} + \bar{\omega}_{0_x})^2 / \bar{\omega}_{0_y}^2]} \Bigg). \end{aligned} \tag{8.1.8}$$

Inserting 8.1.7 into $x = \beta_x^{1/2}(\eta_{0_x} + \eta_{1_x})$ and 8.1.8 into $y = \beta_y^{1/2}(\eta_{0_y} + \eta_{1_y})$, one obtains

$$\begin{aligned}
x = \frac{\beta_x^2}{\rho}\delta - \frac{1}{L}\sum_i S_i\beta_{xi}^2\left(\frac{\beta_x\epsilon_x}{2} - \frac{\beta_y\epsilon_y}{2}\right) - \delta^2\frac{1}{L}\sum_i\frac{S_i\beta_{xi}^6}{\rho^2} + \\
+\frac{1}{L}\sum_i S_i\beta_{xi}^2\left(\frac{\beta_x\epsilon_x}{6}\cos 2\theta_x + \frac{\beta_y\epsilon_y}{2(1-4\bar{\omega}_{0_y}^2/\bar{\omega}_{0_x}^2)}\cos 2\theta_y\right) + \sqrt{\epsilon_x\beta_x}\cos\theta_x \\
y = \sqrt{\epsilon_x\beta_x}\sqrt{\epsilon_y\beta_y}\frac{1}{L}\sum_i S_i\beta_{yi}^2\left(\frac{\cos(\theta_y-\theta_x)}{1-(\bar{\omega}_{0_y}-\bar{\omega}_{0_x})^2/\bar{\omega}_{0_y}^2} + \right. \\
\left. +\frac{\cos(\theta_y+\theta_x)}{1-(\bar{\omega}_{0_y}+\bar{\omega}_{0_x})^2/\bar{\omega}_{0_y}^2}\right) + \sqrt{\epsilon_y\beta_y}\cos\theta_y \\
x' = -\frac{1}{L}\sum_i S_i\beta_{xi}^2\left(\frac{\epsilon_x}{3}\sin 2\theta_x + \frac{\epsilon_y}{1-4\bar{\omega}_{0_y}^2/\bar{\omega}_{0_x}^2}\sin 2\theta_y\right) - \sqrt{\frac{\epsilon_x}{\beta_x}}\sin\theta_x \\
y' = -\frac{1}{L}\sum_i S_i\beta_{yi}^2\sqrt{\frac{\epsilon_x}{\beta_x}}\sqrt{\frac{\epsilon_y}{\beta_y}}\left(\frac{(\beta_x-\beta_y)\sin(\theta_y-\theta_x)}{1-(\bar{\omega}_{0_y}-\bar{\omega}_{0_x})^2/\bar{\omega}_{0_y}^2} + \right. \\
\left. +\frac{(\beta_x+\beta_y)\sin(\theta_y+\theta_x)}{1-(\bar{\omega}_{0_y}+\bar{\omega}_{0_x})^2/\bar{\omega}_{0_y}^2}\right) - \sqrt{\frac{\epsilon_y}{\beta_y}}\sin\theta_y.
\end{aligned} \tag{8.1.9}$$

For the tune shifts one gets

$$\begin{aligned}
\omega_{1_x} &= \frac{\delta}{4\pi}\int_0^{2\pi}\beta_x S D_x d\theta = \delta\frac{1}{4\pi C}\sum_i S_i l_{si} D_{xi}\beta_{xi} \\
\omega_{1_y} &= -\frac{\delta}{4\pi}\int_0^{2\pi}\beta_y S D_x d\theta = \delta\frac{1}{4\pi C}\sum_i S_i l_{si} D_{xi}\beta_{yi}.
\end{aligned} \tag{8.1.10}$$

One should substitute 8.1.9 with $D_x \approx \beta_x^2/\rho$ in the expression for the orbit lengthening, which is

$$\left(\frac{\Delta L}{L}\right)_\beta = \frac{1}{L}\oint\left(\frac{\rho}{x} + \frac{x'^2+y'^2}{2}\right)dS. \tag{8.1.11}$$

The formula 8.1.11 has two terms: one of them is

$$\begin{aligned}
\left(\frac{\Delta L}{L}\right)_{\frac{x}{\rho}} = \frac{1}{L}\oint\frac{x}{\rho}ds = \frac{\delta}{L}\int\frac{D_x}{\rho}ds - \frac{\epsilon_x}{2L}\sum_i S_i l_{si} D_{xi}\beta_{xi} + \\
+\frac{\epsilon_y}{2L}\sum_i S_i l_{si} D_{xi}\beta_{yi} - \frac{\delta^2}{L}\sum_i S_i l_{si} D_{xi}^3
\end{aligned} \tag{8.1.12}$$

and the second one, when $\beta_x = \beta_y$ and $\bar{\omega}_{0_x} = \bar{\omega}_{0_y}$, is

$$\left(\frac{\Delta L}{L}\right)_{x',y'} = \frac{1}{L}\oint\frac{x'^2+y'^2}{2}ds = \frac{5}{4}\left(\frac{\epsilon_x\frac{1}{L}\sum_i S_i\beta_{xi}^2}{3}\right) + \frac{\epsilon_x}{4\beta_x} + \frac{\epsilon_y}{4\beta_y}. \tag{8.1.13}$$

There are quadrupole and sextupole components in the second term. The sextupole contribution to the orbit lengthening is several orders of magnitude smaller than the one from the quadrupoles, which gives the following result

$$\left(\frac{\Delta L}{L}\right)_{x',y'} = \frac{\pi}{2L}\left(\epsilon_x \nu_x + \epsilon_y \nu_y\right). \tag{8.1.14}$$

APPENDIX B

Lagrangian in the cylindrical coordinate system is [91]

$$\mathcal{L} = \frac{m}{2}(\dot{r}^2 + r^2\dot{\theta}^2 + \dot{y}^2) + \frac{2eU_0}{R_2 - R_1}R_2R_1 \cdot \frac{1}{\sqrt{r^2 + y^2}} - \frac{eU_0}{R_2 - R_1}(R_2 + R_1). \tag{8.2.1}$$

APPENDIX C

Structure type	$(S_x)_{RMS}$ = a + b·N at energy spread ΔW/W = 5·10⁻³	(Sx)RMS = a + b·N at horizontal spread x = ± 5·10-3				$(S_x)_{RMS}$ = a + b·N at vertical spread Y = ± 5·10⁻³			
Quasi-frozen spin	RF = 100 kV at 4.4 MHz; SDP1 vary; (the same for SDP2,SDN1, SDN2,SFN1) a = 0.03, b = 2.6·10⁻⁷	SFP1	4.4 MHz	100 kV	a = 4·10⁻⁴ b= 1.4·10⁻⁹	SFP1	4.4 MHz	100 kV	a = 1·10⁻⁵ b= 0.1·10⁻⁹
		SFP1	5.2 MHz	100 kV	a = 5·10⁻⁴ b= 0.5·10⁻⁹	SFP1	5.2 MHz	100 kV	a = 1·10⁻⁵ b= 0.1·10⁻⁹
		SFP1	4.4 MHz	200 kV	a = 4·10⁻⁴ b= 2.6·10⁻⁹	SFP1	4.4 MHz	200 kV	a = 1·10⁻⁵ b= 0.1·10⁻⁹
		SFP1	5.2 MHz	200 kV	a = 5·10⁻⁴ b= 0.1·10⁻⁹	SFP1	5.2 MHz	200 kV	a = 1·10⁻⁵ b= 0.1·10⁻⁹
		SDP1	4.4 MHz	100 kV	a = 5·10⁻⁴ b= 0.5·10⁻⁹	SDP1	4.4 MHz	100 kV	a = 5·10⁻⁶ b= 0.1·10⁻⁹
		SDP1	5.2 MHz	100 kV	a = 5·10⁻⁴ b= 0.1·10⁻⁹	SDP1	5.2 MHz	100 kV	a = 5·10⁻⁶ b= 0.1·10⁻⁹
	RF = 200 kV at 4.4 MHz; SDP1 vary; (the same for SDP2,SDN1, SDN2,SFN1) a = 0.03, b = 0.2·10⁻⁷	SFP1	4.4 MHz	200 kV	a = 5·10⁻⁴ b= 0.2·10⁻⁹	SFP1	4.4 MHz	200 kV	a = 1·10⁻⁵ b= 0.1·10⁻⁹
		SFP1	5.2 MHz	200 kV	a = 5·10⁻⁴ b= 0.01·10⁻⁹	SFP1	5.2 MHz	200 kV	a = 1·10⁻⁵ b= 0.1·10⁻⁹
		SFP1	4.4 MHz	100 kV	a = 5·10⁻⁴ b=0.01·10⁻⁹	SFP1	4.4 MHz	100 kV	a = 1·10⁻⁵ b= 0.1·10⁻⁹
		SFP1	5.2 MHz	100 kV	a = 5·10⁻⁴ b= 0.1·10⁻⁹	SFP1	5.2 MHz	100 kV	a = 1·10⁻⁵ b= 0.1·10⁻⁹
		SDP1	4.4 MHz	200 kV	a = 4·10⁻⁴ b= 0.1·10⁻⁹	SDP1	4.4 MHz	200 kV	a = 5·10⁻⁶ b= 0.1·10⁻⁹
		SDP1	5.2 MHz	200 kV	a = 5·10⁻⁴ b= 0.01·10⁻⁹	SDP1	5.2 MHz	200 kV	a = 5·10⁻⁶ b= 0.1·10⁻⁹

Figure 95: Parameters of function f for different voltages and frequencies of the RF cavity for the quasi-frozen spin lattice. Sextupoles were automatically tuned to find the best spin coherence time.

Structure type	$(S_x)_{RMS}$ = a + b·N at energy spread ΔW/W = 5·10^{-3}	(Sx)RMS = a + b·N at horizontal spread x = ± 5·10-3				$(S_x)_{RMS}$ = a + b·N at vertical spread Y = ± 5·10^{-3}			
Quasi-frozen spin	RF = 100 kV at 5.2 MHz; SDP1 vary; (the same for SDP2,SDN1, SDN2,SFN1) a = 0.03, b = 2.1·10^{-7}	SFN1	4.4 MHz	100 kV	a = 4·10^{-4} b= 0.6·10^{-9}	SFN1	4.4 MHz	100 kV	a = 5·10^{-5} b= 0.1·10^{-9}
		SFN1	5.2 MHz	100 kV	a = 5·10^{-4} b= 0.01·10^{-9}	SFN1	5.2 MHz	100 kV	a = 1·10^{-5} b= 0.1·10^{-9}
		SFN1	4.4 MHz	200 kV	a = 4·10^{-4} b= 0.6·10^{-9}	SFN1	4.4 MHz	200 kV	a = 5·10^{-5} b= 0.1·10^{-9}
		SFN1	5.2 MHz	200 kV	a = 6·10^{-4} b= 0.5·10^{-9}	SFN1	5.2 MHz	200 kV	a = 5·10^{-5} b= 0.1·10^{-9}
		SDN1	4.4 MHz	100 kV	a = 5·10^{-4} b= 0.3·10^{-9}	SDN1	4.4 MHz	100 kV	a = 5·10^{-6} b= 0.1·10^{-9}
		SDN1	5.2 MHz	100 kV	a = 5·10^{-4} b= 0.1·10^{-9}	SDN1	5.2 MHz	100 kV	a = 5·10^{-6} b= 0.1·10^{-9}
	RF = 200 kV at 5.4 MHz; SDP1 vary; (the same for SDP2,SDN1, SDN2,SFN1) a = 0.03, b = 0.2·10^{-7}	SDN1	4.4 MHz	200 kV	a = 5·10^{-4} b= 0.2·10^{-9}	SDN1	4.4 MHz	200 kV	a = 4·10^{-5} b= 0.1·10^{-9}
		SDN1	5.2 MHz	200 kV	a = 5·10^{-4} b= 0.01·10^{-9}	SDN1	5.2 MHz	200 kV	a = 4·10^{-5} b= 0.1·10^{-9}
		SDN2	4.4 MHz	100 kV	a = 5·10^{-4} b=0.01·10^{-9}	SDN2	4.4 MHz	100 kV	a = 5·10^{-5} b= 0.1·10^{-9}
		SDN2	5.2 MHz	100 kV	a = 5·10^{-4} b= 0.1·10^{-9}	SDN2	5.2 MHz	100 kV	a = 5·10^{-5} b= 0.1·10^{-9}
		SDN2	4.4 MHz	200 kV	a = 4·10^{-4} b= 0.1·10^{-9}	SDN2	4.4 MHz	200 kV	a = 5·10^{-6} b= 0.1·10^{-9}
		SDN2	5.2 MHz	200 kV	a = 5·10^{-4} b= 0.01·10^{-9}	SDN2	5.2 MHz	200 kV	a = 5·10^{-6} b= 0.1·10^{-9}

Figure 96: Parameters of function f for different voltages and frequencies of the RF cavity for the quasi-frozen spin lattice. Sextupoles were automatically tuned to find the best spin coherence time.

9

ACKNOWLEDGMENTS

In the end, I want to thank groups of people who supported me throughout those years of my work on this thesis, those people who helped me to bring this work to life.

Before all else, I would like to thank my supervisors Prof. Dr. Jörg Pretz and Prof. Dr. Yuri Senichev. Both of them helped me with overcoming numerous obstacles in my studies, our fruitful discussions have produced many good-quality results and generated wonderful ideas that allowed me to complete my work. My knowledge of spin-orbital dynamics and statistics has been colossally improved during our mutual work.

I wish to express my gratitude to the whole JEDI collaboration and to some individual groups in particular. I am thankful to the COSY accelerator crew and especially to Dr. Bernd Lorentz and Dr. Ralf Gebel. The experimental part of my thesis and benchmarking of my simulations would not be possible without their participation. I would like to thank Prof. Dr. Sergey Andrianov and Dr. Andrey Ivanov for developing the program MODE for spin-orbital tracking, which I used in my studies. Their support was critical in the times when I designed modest EDM measurement simulations. Regarding specific theoretical questions, I would like to thank Dr. Nikolai Nikolaev. With his help, I was able to master my knowledge in the field of geometrical phases in storage rings.

Also, I want to thank all doctoral candidates that worked with me during four years, especially Marcel Rosenthal, Dennis Eversmann, Artem Saleev, Denis Zyuzin, Fabian Trinkel, Sebastian Mey, Fabian Hinder, Jan Hetzel and Nils Hempelmann. We had many conversations about experimental setups, simulations, theoretical aspects, which helped me make to progress in my studies.